

# UNIVERSITÀ DEGLI STUDI DI PADOVA

**Dipartimento di Fisica e Astronomia "Galileo Galilei"**

**Master Degree in Physics**


**Final Dissertation**

# Improved resonance strengths in the $^{21}$Ne(p,$\gamma$) reaction at astrophysical energies


**Thesis supervisor**

**Prof. Antonio Caciolli**

**Thesis co-supervisor**

**Dr. Francesca Cavanna**

**Candidate**

**Chiara Baron**


**Academic Year 2022/2023**

# Contents

# Introduction

The life of stars comprises several stages in which nuclear processes provide the energy necessary to balance the force of gravity and establish a state of hydrostatic equilibrium. Nuclear reactions power the stars fusing lighter elements into heavier ones, and in these processes elements from helium to iron are synthesized. The first set of thermonuclear reactions to be ignited is hydrogen burning, which mainly proceeds through the *pp* chains or, in massive stars, the *CNO* cycles. Moreover, in hot second generation stars, the *NeNa* cycle contributes to burning hydrogen into helium, exploiting the neon and sodium isotopes as catalysts. This cycle is of fundamental importance in the nucleosynthesis of elements comprised between $^{20}$Ne and $^{24}$Mg and it is active in red giant branch stars during shell hydrogen burning, asymptotic giant branch stars, massive stars in the main sequence, classical novae and supernovae. The *NeNa* cycle involves proton capture reactions on all stable isotopes of neon and the $^{21}$Ne(p,$\gamma$)$^{22}$Na reaction has the major astrophysical impact of producing the unstable nucleus of $^{22}$Na, which is a stellar $\gamma$ ray signature. In particular, the production of $^{22}$Na is a distinctive characteristic of classical novae whose underlying white dwarf has a core composed of oxygen and neon. The knowledge of the $^{21}$Ne(p,$\gamma$)$^{22}$Na reaction rate is fundamental to predict the $^{22}$Na abundances produced in these environments. What is more, the nuclear physics input is also crucial in theoretical models that explain the observed excess of $^{22}$Ne (daughter nucleus of $^{22}$Na) in carbon rich presolar grains with the production of $^{22}$Na through the $^{21}$Ne(p,$\gamma$)$^{22}$Na reaction in core collapse supernovae. The $^{21}$Ne(p,$\gamma$)$^{22}$Na reaction rate is dominated by several resonances at astrophysical energies and the resonance strengths are known with high uncertainties ($\sim$ 20%) from previous experiments. To the purpose of reducing the uncertainties, the resonances at $E_p = 126, 271, 272, 290$ and 352 keV are being remeasured in an ongoing experiment at the Laboratory for Underground Nuclear Astrophysics (LUNA) in the Gran Sasso National Laboratory. Indeed, the underground facility is characterized by an exceptionally low background and it is particularly suited to measure the signal produced by reactions with extremely small cross section, such as charged particle induced reactions at low energy.

The objective of this thesis is the study of the two resonances at $E_p = 271$ and 272 keV, measured at LUNA in Autumn 2022. I contributed to the data taking with several shifts at the Gran Sasso National Laboratory and I took care of the complete analysis of the experimental data. In the measurement, the intense proton beam delivered by the LUNA 400 kV accelerator impinges on the windowless gas target filled with natural neon gas, and the prompt $\gamma$ rays produced by the reaction are detected by two high purity germanium detectors. The two resonances at $E_p = 271$ and 272 keV are very close in energy and it is not possible to resolve them individually using this experimental setup. However, the two resonances populate excited states of $^{22}$Na at different energies and it is possible to distinguish the two contributions through the analysis of the $\gamma$ rays emitted in the de-excitation process. Four new primary transitions are identified for the de-excitation of the $^{22}$Na level populated by the $E_p = 272$ keV resonance, and the branching ratios have been calculated. The analysis of the experimental data reported in this thesis is an evaluation of the resonance energy and

strength of both resonances. In comparison to literature [1], the resonance energies measured at LUNA for the $E_p = 271$ and 272 keV resonances are higher by 0.9 and 0.8 keV, respectively. What is more, the resonance strengths have been measured with higher precision compared to the values reported in literature [2, 1], and for the $E_p = 272$ keV resonance the obtained value is higher by 40 meV than the expected one.

This thesis is organized in four main chapters. Chapter 1, after a brief overview on stellar evolution, introduces the major features of thermonuclear reactions in stars. Then, Chapter 2 is dedicated to the astrophysical relevance of the $^{21}$Ne(p,$\gamma$)$^{22}$Na reaction. Moreover, the existing measurements on the resonant contributions to the reaction rate are reviewed. In Chapter 3, it is described the LUNA underground facility and the experimental setup adopted in the $^{21}$Ne(p,$\gamma$)$^{22}$Na reaction study. Eventually, in Chapter 4 the data analysis procedure and the obtained results are discussed.

# Chapter 1

# Thermonuclear reactions in stars

Thermonuclear reactions are of crucial importance in stellar evolution since they are responsible for the energy production in stars. Indeed, during the majority of a star's life, the fusion of lighter nuclei into heavier elements provides the kinetic energy necessary to balance the gravitational contraction. What is more, thermonuclear reactions are fundamental for the nucleosynthesis of the elements in stars: the different evolutionary stages are associated to nuclear processes that synthesize increasingly heavier elements [3]. As a consequence, fusion reactions alter the stellar composition and the freshly produced heavier nuclei enrich the interstellar matter when mass is ejected in several evolutionary stages. The interstellar matter, in turn, provides the elements from which new generation stars originate.

The first part of this Chapter is an overview on stellar evolution, while the second part illustrates the concept of thermonuclear reaction rate. Finally, in the last two Sections, the non-resonant and resonant contributions to the reaction rate are described. More details can be found in [4, 5], used as reference for this Chapter.

## 1.1 Overview on stellar evolution

A star originates from the gravitational contraction of an interstellar gas cloud whose composition is mainly hydrogen and helium. In this process, gravitational potential energy is transformed into thermal energy and radiation. Initially, the gas experiences gravitational free falling, but, as the density rises, there is a correspondent increase in opacity, with the consequence that part of the emitted ration is not liberated but stored in the interior. Thus, the temperature and pressure begin to rise, slowing down the contraction of the central and denser part.

The star continues to shrink until the temperature in the center is high enough to ignite the first set of thermonuclear reactions, which convert hydrogen into helium. At this point, the star settles in a long lived state of hydrostatic and thermal equilibrium in which hydrogen is burnt in the core and the gravitational contraction is temporarily halted. During this stage, stars are in the *main sequence* and have different properties depending on the initial mass and composition. As a result, main sequence stars are found in a large range of temperatures and luminosity in the Hertzsprung-Russell diagram (Figure 1.1), which shows the correlation between the stellar luminosity and the effective surface temperature. As it can be seen, massive stars are in the high luminosity part of the diagram: the mass is directly correlated to the internal temperature, and nuclear reactions proceeds faster as the temperature increases, generating a larger energy output. The reaction networks that contribute to hydrogen burning in stellar cores are mainly two: the *pp* chains and the *CNO* cycles. In both cases, the net effect is the conversion of four protons into a helium nucleus. The *pp* chains are the dominant source

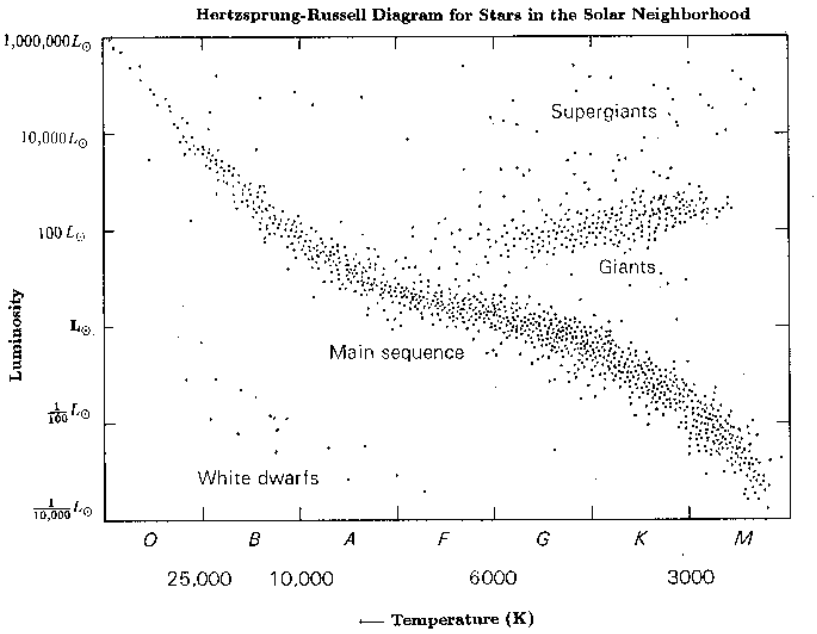


Figure 1.1: Hertzsprung-Russell diagram: the luminosity of stars is represented as a function of the surface temperature. https://casswww.ucsd.edu/archive/public/tutorial/HR.html

of energy in low mass stars ($M \leq 1.5 M_\odot$[1]), while in high mass stars, where the temperatures are higher, the *CNO* cycles are the main hydrogen fusion path.

When hydrogen is exhausted, the composition of the core is mainly helium and the star contracts. Eventually, hydrogen fusion is ignited again in a shell surrounding the core, which is still contracting and becoming hotter. If the star has low mass, the core is electron degenerate and, when the temperature is high enough for fusing helium into carbon and oxygen, a thermonuclear runaway, called *core helium flash*, takes place. The large amount of energy released lifts the degeneracy and helium burning is ignited. Instead, if the star is more massive ($M \geq 2 M_\odot$), the core is not degenerate and helium ignites quiescently.

When helium is exhausted, the oxygen and carbon core contracts, heats up and helium burning is ignited in a surrounding shell. At this point, the star approaches the final evolutionary stages, which depends critically on its initial mass: higher mass stars reaches higher temperatures and further burning phases are possible.

It is important to highlight that the endpoints of stellar evolution of both intermediate and massive stars are sites in which the $^{21}$Ne(p,$\gamma$)$^{22}$Na reaction plays a significant role. These are described in detail in Chapter 2.

## 1.2 Thermonuclear reaction rates

Nuclear reactions can be classified in two main categories, according to the sign of their $Q_{value}$, which is defined as

$$Q_{value} = \sum_i m_{i,initial} - \sum_i m_{i,final} \tag{1.1}$$

where the first summation runs over the masses of the nuclei that produce the reaction and the second one over the masses of the reaction products. If the $Q_{value}$ is positive, the nuclear reaction is exothermic and the $Q_{value}$ is the amount of released energy. On the other hand,

[1] The symbols $M_\odot$ and $L_\odot$ refer to the mass and the luminosity of the Sun respectively.

if the $Q_{value}$ is negative, the reaction is endothermic and it is necessary to provide energy in order for the reaction to occur. In stellar environment, exothermic reactions are of crucial importance because they provide the energy necessary to compensate the gravitational collapse of the star.

Another fundamental quantity in describing the nuclear energy production in a star is the total produced energy, which is given by the product of the $Q_{value}$ and the reaction rate (number of reactions that takes place per unit time and unit volume). Considering a particle-induced reaction $0 + 1 \rightarrow 2 + 3$[2] it is possible to define the reaction rate as

$$r_{01} = N_0 N_1 v \sigma(v) \tag{1.2}$$

where $N_0$ and $N_1$ are the projectile and target number densities respectively, $v$ is the relative velocity between projectile and target, and $\sigma$ is the cross section, which in turn depends on the relative velocity. The relative velocity of the interacting nuclei is not constant, but it is described by a probability function $P(v)$, normalized to 1:

$$\int_0^\infty P(v)dv = 1 \tag{1.3}$$

where $P(v)dv$ is the probability that the relative velocity is comprised between $v$ and $v + dv$. In equilibrium conditions, the kinetic energy at disposal of nuclei in stellar gas derives only from their thermal motion and thus the reactions that take place in this environment are called *thermonuclear reactions*. In this framework, the velocities of nuclei are described by Maxwell-Boltzmann distributions. In particular, if the velocities of the two interacting nuclei are described by Maxwell-Boltzmann distributions, their relative velocity has also the same probability function:

$$P(v)dv = \left(\frac{m_{01}}{2\pi kT}\right)^{3/2} e^{-m_{01}v^2/(2kT)} 4\pi v^2 dv \tag{1.4}$$

where $k = 8.6173 \cdot 10^{-5}$ eV/K is the Boltzmann constant, $T$ is the temperature and $m_{01} = m_0 m_1/(m_0 + m_1)$ is the reduced mass. A convenient way of rewriting eq. 1.4 by introducing the energy $E = m_{01}v^2/2$ is

$$P(v)dv = \left(\frac{2}{\sqrt{\pi}}\right) \frac{1}{(kT)^{3/2}} \sqrt{E} e^{-E/kT} dE \tag{1.5}$$

The function written in eq. 1.5 increases linearly at low energy, then it reaches a maximum and eventually decreases exponentially, approaching zero at high energy.

Once the probability function is known, it is possible to write the reaction rate per particle pair:

$$< \sigma v >_{01} = \int_0^\infty P(v)\sigma(v)v dv = \left(\frac{8}{\pi m_{01}}\right)^{1/2} \frac{1}{(kT)^{3/2}} \int_0^\infty E\sigma(E) e^{-E/kT} dE \tag{1.6}$$

where the notation $< \sigma v >$ refers to the average value. Inserting eq. 1.6 in eq. 1.2, it is possible to rewrite the reaction rate as:

$$r_{01} = \frac{N_0 N_1 < \sigma v >_{01}}{1 + \delta_{01}} \tag{1.7}$$

where the term $(1 + \delta_{01})$, with $\delta_{01}$ the Kronecker delta, is introduced to take into account the possibility of reactions among identical particles. The reaction rate can be calculated

[2] In this notation 0 indicates the projectile, 1 the target, 2 and 3 the reaction products.

once it is known the reaction rate per particle pair $< \sigma v >$, which contains the nuclear physics information. This latter quantity is either measured experimentally or derived from theoretical models. The cross section $\sigma$ depends on the considered reaction and the reaction rate per particle pair $< \sigma v >$ depends strongly on the temperature. Since the temperature changes as the star evolves, it is necessary to determine $< \sigma v >$ for all the evolution stages of interest.

## 1.3 Charged particle induced non resonant reactions

Thermonuclear reactions have different properties depending on the type of particle is the projectile. It may be a photon (in this case the reaction is called photodisintegration), a neutron or a charged nucleus. This Section and the following ones report some details on reactions induced by charged particles.

In reactions involving charged nuclei there are two forces at work: the attractive nuclear potential, which has short range and it is relevant for distances shorter than the nuclear radius $R_n = R_0 + R_1$ ($R_0$ is the radius of the projectile and $R_1$ is the radius of the target), and the repulsive Coulomb potential, which, instead, is long range (see Figure 1.2). Classically, the

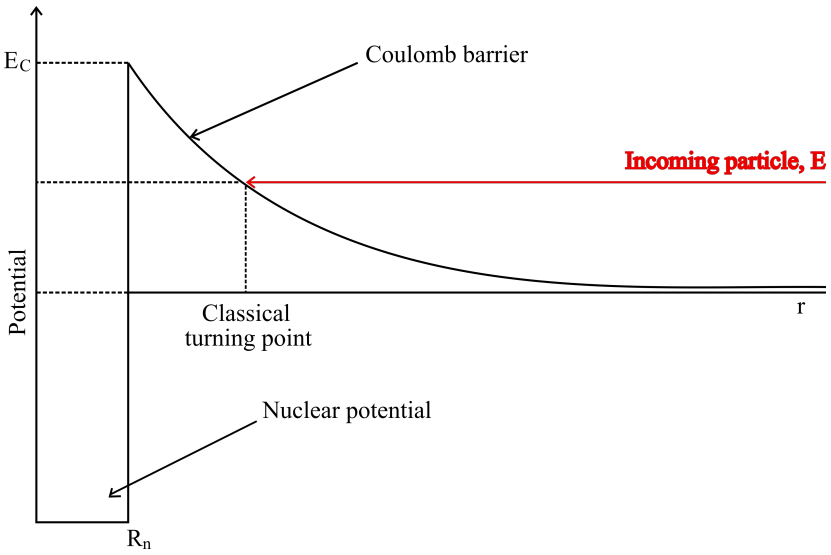


Figure 1.2: Diagram of the attractive nuclear potential and of the repulsive Coulomb one. Classically, the incoming particle can reach distances shorter than the nuclear radius ($R_n = R_0 + R_1$) only if its energy is higher than the Coulomb barrier.

incoming projectile can reach the region of the nuclear potential only if its energy $E$ is higher than the Coulomb barrier $E_C$. As mentioned above, the nuclei have kinetic energy only from their thermal motion and thus the energy is not sufficient to overcome the Coulomb barrier at typical temperatures of quiescent burning. Nonetheless, fusion reactions in stars are possible thanks to the quantum mechanical process known as *tunnel effect*. In this case, the probability that a nucleus penetrates the Coulomb barrier and feels the attractive nuclear potential is not null even if $E < E_C$. The penetration probability is function of the energy: it approaches 1 close to $E_C$ and falls to zero as the energy decreases. At low energy ($E << E_C$) and in the approximation that the contribution to the barrier from orbital momentum is negligible, it can be approximated as

$$P \propto e^{-2\pi\eta} \tag{1.8}$$

where $\eta$ is the Sommeferld parameter, defined as

$$\eta = \frac{Z_0 Z_1 e^2}{\hbar v} \tag{1.9}$$

with $Z_0$ and $Z_1$ the charges of the interacting nuclei, $v$ their relative velocity, $e$ the charge of the electron and $\hbar$ the Planck constant divided by $2\pi$. The cross section of the reaction is proportional to the penetration probability:

$$\sigma(E) \propto e^{-2\pi\eta} \tag{1.10}$$

As a consequence of the exponential in the penetration probability, the cross section drops at lower energies. This rapid decrease is one of the major challenges in experimental nuclear astrophysics. Indeed, in direct measurements the energies of interest are usually low and thus the cross sections to be measured are extremely small.

In the description of non resonant reactions, it is useful to write the cross section in terms of the *astrophysical S-factor* $S(E)$, which, in case of only s-wave transmission probability, can be introduced as

$$\sigma(E) = \frac{1}{E} e^{-2\pi\eta} S(E) \tag{1.11}$$

where $1/E$ is a geometrical term linked to the de Broglie wavelength, while $e^{-2\pi\eta}$ comes from the penetration probability (eq. 1.10) and $S(E)$ is the $S$-factor which includes all the nuclear effects. The advantage of the $S$-factor over the cross section is that it has a smoother dependence on the energy for non resonant reactions.

Using eq. 1.11 it is possible to rewrite the reaction rate per particle pair (eq. 1.6) as

$$< \sigma v >= \left(\frac{8}{\pi m_{01}}\right)^{1/2} \frac{1}{(kT)^{3/2}} \int_0^\infty e^{-2\pi\eta} S(E) e^{-E/kT} dE$$

$$= \left(\frac{8}{\pi m_{01}}\right)^{1/2} \frac{1}{(kT)^{3/2}} \int_0^\infty exp\left(-\frac{2\pi}{\hbar}\sqrt{\frac{m_{01}}{2E}} Z_0 Z_1 e^2\right) S(E) e^{-E/kT} dE \tag{1.12}$$

An important feature of the integrand of eq. 1.12 is that it includes the product of two exponential functions that depends on the energy: the term $e^{-1/\sqrt{E}}$ from the penetration probability, which tends to zero at low energies, and the term $e^{-E/kT}$ from the Maxwell Boltzmann distribution, which goes to zero at high energies. The product of these two exponential functions has a maximum called the *Gamow peak*, whose energy $E_0$ is higher respect to the maximum of the Maxwell Boltzmann distribution. This is due to the convolution of $e^{-E/kT}$ with the penetration probability, which has the effect of shifting the peak towards the high energy tail of the Maxwell Boltzmann distribution. Figure 1.3 shows the Maxwell-Boltzmann and the Gamow factors together with the Gamow peak for the $^{21}$Ne(p,$\gamma$)$^{22}$Na reaction at the temperature of a classical nova.

The maximum of the Gamow peak $E_0$ can be obtained imposing the first derivative of the integrand equal to zero:

$$E_0 = 0.1220 \left(Z_0^2 Z_1^2 \frac{M_0 M_1}{M_0 + M_1} T_9^2\right)^{1/3} \tag{1.13}$$

where $M_0$ and $M_1$ are the masses of the projectile and target respectively, and $T_9$ is the temperature in units of $10^9$ K. On the other hand, the width $\Delta$ of the Gamow peak can be determined approximating the peak with a Gaussian function whose maximum is equal to $E = E_0$:

$$\Delta = \frac{4}{\sqrt{3}}\sqrt{E_0 kT} = 0.2368 \left(Z_0^2 Z_1^2 \frac{M_0 M_1}{M_0 + M_1} T_9^5\right)^{1/6} \tag{1.14}$$

The importance of the Gamow peak is that most non resonant reactions take place in the energy range $E_0 - \Delta/2$ and $E_0 + \Delta/2$.

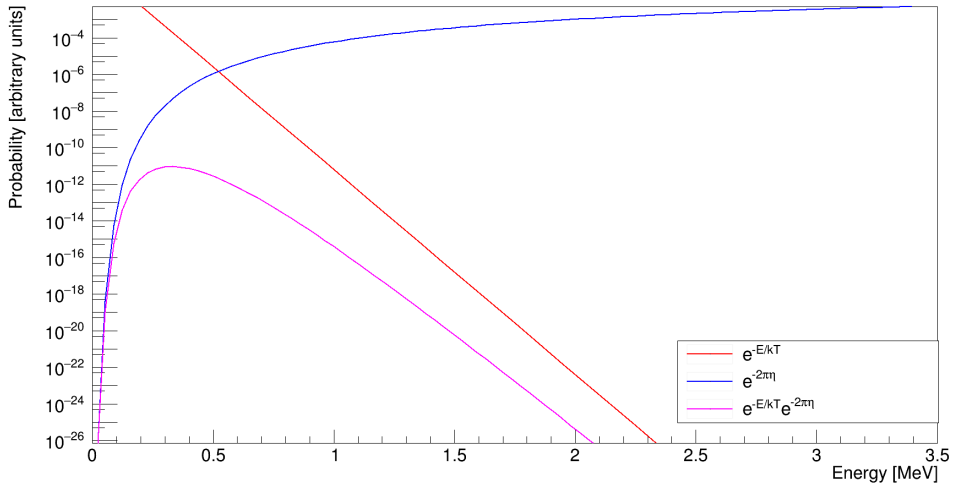


Figure 1.3: Maxwell-Boltzmann factor (red line), Gamow factor (blue line) and Gamow peak (pink line) for the $^{21}$Ne(p,$\gamma$)$^{22}$Na reaction at a temperature of T=0.45 GK (classical nova).

## 1.4 Charged particle induced resonant reactions

Regarding proton capture reactions, resonances are two step processes in which it is firstly populated an excited state of the compound nucleus and subsequently the excited state decays to lower-lying states. In order to have the production of a resonant reaction, the following energy relation must be satisfied:

$$E_r = E_i - Q_{value} \tag{1.15}$$

where $E_r$ is the energy of the projectile in the center of mass frame and $E_i$ is the energy of the excited level of the compound nucleus that is populated. The process is schematized in the diagram shown in Figure 1.4.

The cross section of the process is proportional to the product of the matrix elements of the two steps:

$$\sigma \propto | < E_f|H_\gamma|E_i > |^2 | < E_i|H_f|0+1 > |^2 \tag{1.16}$$

where the operator $H_f$ describes the formation of the compound state $E_i$ and the operator $H_\gamma$ describes the decay of the excited level $E_i$ of the compound nucleus to the final state $E_f$. Contrary to the case of non resonant reactions, in which the $S$-factor varies smoothly with energy, in the presence of a resonance the $S$-factor varies strongly with energy and the cross section may acquire high values at energies close to $E_r$.

The resonant reactions that contribute to the reaction rate can be classified into three main categories: narrow, broad and subthreshold resonances. In the following these contributions are analyzed.

### 1.4.1 Narrow and isolated resonances

This thesis is focused on the study of two narrow and isolated resonances of the $^{21}$Ne(p,$\gamma$)$^{22}$Na reaction and in the following chapters this type of resonances is discussed. A resonance is considered isolated if the level density of the compound nucleus is small, namely different resonances do not overlap. Instead, a resonance is narrow if the partial widths can be

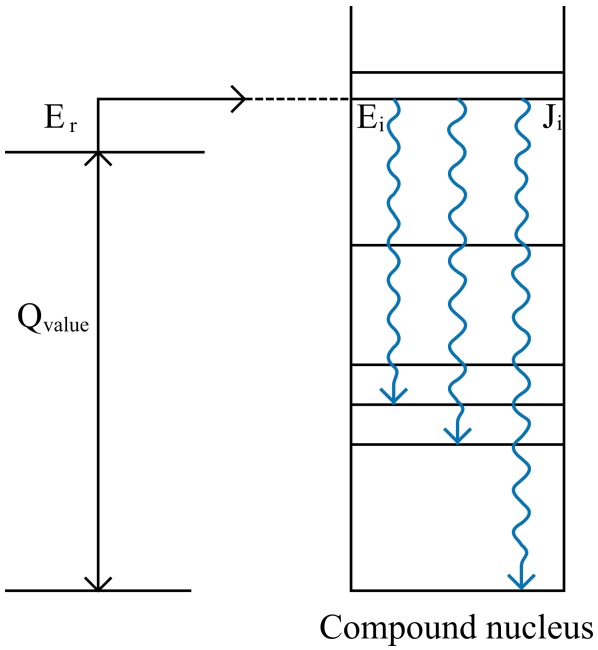


Figure 1.4: Diagram of a resonant reaction of the type $0+1 \rightarrow 2+\gamma$. If the projectile energy satisfies eq. 1.15, the energy level $E_i$ of the compound nucleus is populated. Then the level $E_i$ de-excites through photon emission.

assumed constant over the resonance width. If the condition of isolated resonance is fulfilled, the cross section is well described by the Breit-Wigner function:

$$\sigma_{BW}(E) = \frac{\lambda^2}{4\pi}\omega\frac{\Gamma_a\Gamma_b}{(E_r - E)^2 + \Gamma^2/4} \tag{1.17}$$

where $\lambda$ is de Broglie wavelength, $E_r$ is the resonance energy in the center of mass frame, $\Gamma_a$ and $\Gamma_b$ are the partial widths of entrance and exit channels, and $\Gamma$ is the total resonance width. The term $\omega$ is introduced to simplify the notation:

$$\omega = \frac{(2J+1)(1+\delta_{01})}{(2J_0+1)(2J_1+1)} \tag{1.18}$$

with $J$ spin of the resonance, $J_0$ and $J_1$ the spins of target and projectile respectively. The factor $\delta_{01}$ is a term introduced to take into account the possibility that the target and the projectile are identical particles. Then, the reaction rate in eq. 1.6 can be rewritten inserting the expression of the cross section in eq. 1.17:

$$\begin{aligned} < \sigma v > &= \left(\frac{8}{\pi m_{01}}\right)^{1/2}\frac{1}{(kT)^{3/2}}\int_0^\infty E\sigma_{BW}(E)e^{-E/kT}dE \\ &= \frac{\sqrt{2\pi}\hbar^2}{(m_{01}kT)^{3/2}}\omega\int_0^\infty \frac{\Gamma_a\Gamma_b}{(E_r-E)^2+\Gamma^2/4}e^{-E/kT}dE \end{aligned} \tag{1.19}$$

In the hypothesis of narrow resonance, the partial widths and the Boltzmann term $e^{-E/kT}$ are considered constant over the resonance width and it is possible to calculate them at the resonance energy $E_r$:

$$< \sigma v > = \frac{\sqrt{2\pi}\hbar^2}{(m_{01}kT)^{3/2}}e^{-E_r/kT}\omega\frac{\Gamma_a\Gamma_b}{\Gamma}2\int_0^\infty \frac{\Gamma/2}{(E_r-E)^2+\Gamma^2/4}dE$$

$$= \frac{\sqrt{2\pi}\hbar^2}{(m_{01}kT)^{3/2}} e^{-E_r/kT} \omega \frac{\Gamma_a \Gamma_b}{\Gamma} 2\pi = \left(\frac{2\pi}{m_{01}kT}\right)^{3/2} \hbar^2 e^{-E_r/kT} \omega\gamma \tag{1.20}$$

where $\omega\gamma = \omega\Gamma_a\Gamma_b/\Gamma$ is called *resonance strength* and it is the integrated cross section.

If a reaction has more than one narrow resonance, their contribution to the reaction rate is obtained through the sum:

$$< \sigma v >= \left(\frac{2\pi}{m_{01}kT}\right)^{3/2} \hbar^2 \sum_i (\omega\gamma)_i e^{-E/kT} \tag{1.21}$$

Resonant reactions take place only at energies of the projectile that satisfies eq. 1.15. For this reason narrow resonances contribute to the reaction rate only if their energy is in the energy window of interest for astrophysics. The concept of Gamow peak does not apply in this case, however it is a useful tool to discriminate which resonances contribute to the reaction rate. Indeed, the major contribution to the rate is expected from resonances whose energies lie in the range $E_0 \pm \Delta$.

### 1.4.2 Broad and subthreshold resonances

A resonance is defined broad if the following relation among the resonance energy and the width holds:

$$\Gamma/E_r \geq 10\% \tag{1.22}$$

If this is the case, it is not possible to assume that the cross section is equal to the value acquired at the energy $E_r$ over all the energy window in which the resonance extends. For this reason, it is necessary to take into account the energy dependence of the cross section when evaluating the reaction rate per particle pair $< \sigma v >$. Particular attention should be paid to interference contributions. Indeed, these may be relevant if more than one broad resonance of same angular momentum and parity are present within the same energy region.

Instead, a subthreshold resonance is characterized by the fact that the excited level of the compound nucleus $E_i$ has energy lower than the $Q_{value}$ for the considered decay channel. Thus, the level at $E_i$ cannot be populated by a resonant reaction. However, the excited levels of a nucleus are not stable, hence they are characterized by a finite lifetime and an associated width. If the high energy wing of a subthreshold state extends above the $Q_{value}$, the subthreshold resonance may contribute to the cross section.

Eventually, the total reaction rate is obtained from the sum of all the contributions from either non resonant and resonant processes, including possible interference contributions.

# Chapter 2

# Astrophysical motivation

The $^{21}$Ne(p,$\gamma$)$^{22}$Na reaction is part of the *NeNa* cycle, which contributes to hydrogen burning and nucleosynthesis in several stellar environments. The major astrophysical impact of this reaction is the production of the unstable nucleus of $^{22}$Na, a stellar $\gamma$ ray signature. In order to describe the produced nuclear abundances, it is necessary to determine the reaction rate, which, for the $^{21}$Ne(p,$\gamma$)$^{22}$Na reaction, has contributions from a number of resonances at low energies. In this context, an experimental campaign is ongoing at LUNA to re-measure the most relevant resonances, with the objective of determining the resonance strengths with a reduced uncertainty respect to previous measurements. The first part of this chapter is dedicated to the main features of the *NeNa* cycle and the stellar environments in which the $^{21}$Ne(p,$\gamma$)$^{22}$Na reaction plays an important role. In the second part, the major experimental results on this reaction are collected.

## 2.1 *NeNa* cycle

As mentioned in Chapter 1, hydrogen burning in stars proceeds mainly through the *pp* chains and the *CNO* cycles, with one of the two processes being the dominant source of energy depending on the temperature and composition of the stellar environment. If the *CNO* cycle is activated, it proceeds mainly through two different paths: the *CN* branch, dominant at lower temperatures ($T \sim 20$ MK), and the *NO* path, dominant at higher temperatures ($T \gtrsim 30$ MK) [6]. When the temperature in the star's core is higher than 15 MK, the *CN* cycle is the major source of energy. However, at these temperatures it is activated also the *NeNa* cycle, which contributes to hydrogen burning converting four protons into helium thanks to catalyst isotopes of neon and sodium. Since the rate of the *NeNa* cycle is slower than the *CN* cycle, its importance is not associate to energy production but to the synthesis of elements between $^{20}$Ne and $^{24}$Mg [7].

The *NeNa* cycle is composed of a series of charged particle induced reactions involving all three neon stable isotopes $^{20}$Ne, $^{21}$Ne and $^{22}$Ne [4] (see Figure 2.1). The stellar environments in which it is active are red giant branch stars during shell hydrogen burning (*RGB*) [9, 10], asymptotic giant branch stars (*AGB* stars) [11], massive stars in the main sequence, classical novae [12] and supernovae. A detailed knowledge of the reactions involved in the *NeNa* cycle is fundamental to characterize the nucleosynthesis in these environments and determine the abundances of the synthesized elements [6]. To this scope, the determination of the reaction rates plays a fundamental role. The relative thermonuclear reaction rates, obtained from literature data, are shown in Figure 2.2 for all the reactions involved in the *NeNa* cycle. The first reaction, $^{20}$Ne(p,$\gamma$)$^{21}$Na, has the lowest reaction rate [13] and thus is the bottleneck of the cycle, setting both the duration of the entire cycle and the abundances of isotopes produced by subsequent reactions. The presence of the $^{20}$Ne isotope is necessary for the activation of the

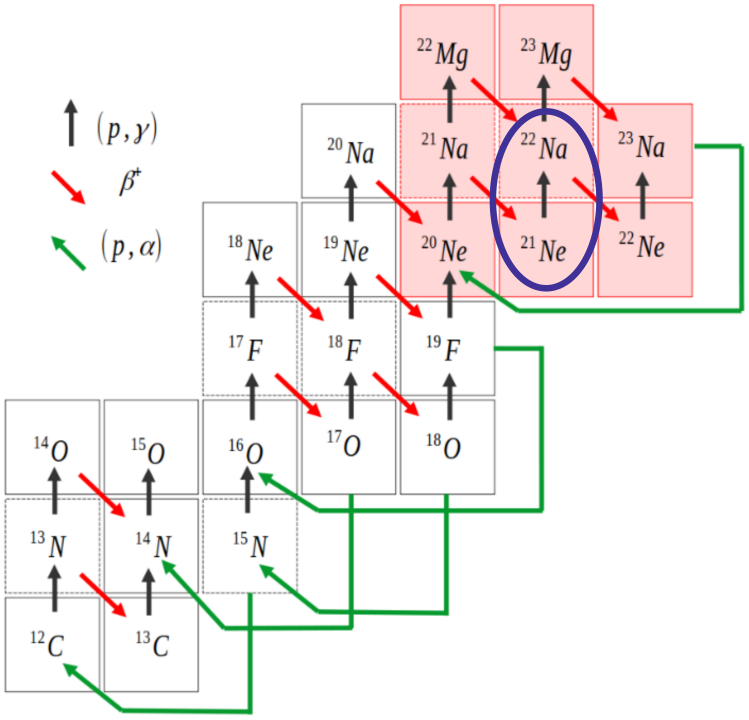


Figure 2.1: Reaction network of the *hot CNO* cycle (white boxes) and the *NeNa* cycle (red boxes). Stable nuclei are drawn inside solid line boxes, while unstable ones in dashed boxes. Figure taken from [8].

*NeNa* cycle. If not already present as a seed nucleus of the star, $^{20}$Ne can be produced by three different thermonuclear processes: during the *hot CNO* cycle from the proton capture on $^{19}$F or the decay of $^{20}$Na, during helium burning from the $\alpha$ capture process $^{12}$C$(\alpha,\gamma)^{16}$O$(\alpha,\gamma)^{20}$Ne, and during carbon burning through the reaction $^{12}$C($^{12}$C,$\alpha$)$^{20}$Ne [8]. It is important to note that the last two production mechanisms take place in extreme environments and contribute less than the first.

In recent years, at LUNA, a large experimental effort has been devoted to the improvement of existing data on the reactions of the *NeNa* cycle. In this context, three experimental campaigns have already been completed. Firstly it was measured the $^{22}$Ne(p,$\gamma$)$^{23}$Na reaction, which had the highest uncertainties, and three new low energy resonances were discovered [17, 18, 19, 20, 21]; the obtained results have been confirmed also by other laboratories [22, 23]. Secondly, it was studied the $^{23}$Na(p,$\gamma$)$^{24}$Mg reaction, which is the breakout from the cycle [24]. Lastly, the first reaction of the cycle $^{20}$Ne(p,$\gamma$)$^{21}$Na has been performed [8].

The ongoing measurement has the objective of reducing the uncertainties on the reaction rate of the $^{21}$Ne(p,$\gamma$)$^{22}$Na reaction, whose importance is linked to the production of the unstable sodium isotope $^{22}$Na in novae and supernovae. The produced $^{22}$Na nucleus decays with a lifetime of 2.602 years to an excited level of $^{22}$Ne, which subsequently de-excites emitting a $\gamma$ ray of 1275 keV. Both the 1275 keV $\gamma$ line and the presence of the daughter nucleus $^{22}$Ne are strong signatures of $^{22}$Na production. Thus, the experimental observation of the $^{22}$Na decay products is extremely useful to infer the $^{22}$Na abundance in astrophysical scenarios and to impose constraints on the nucleosynthesis [12].

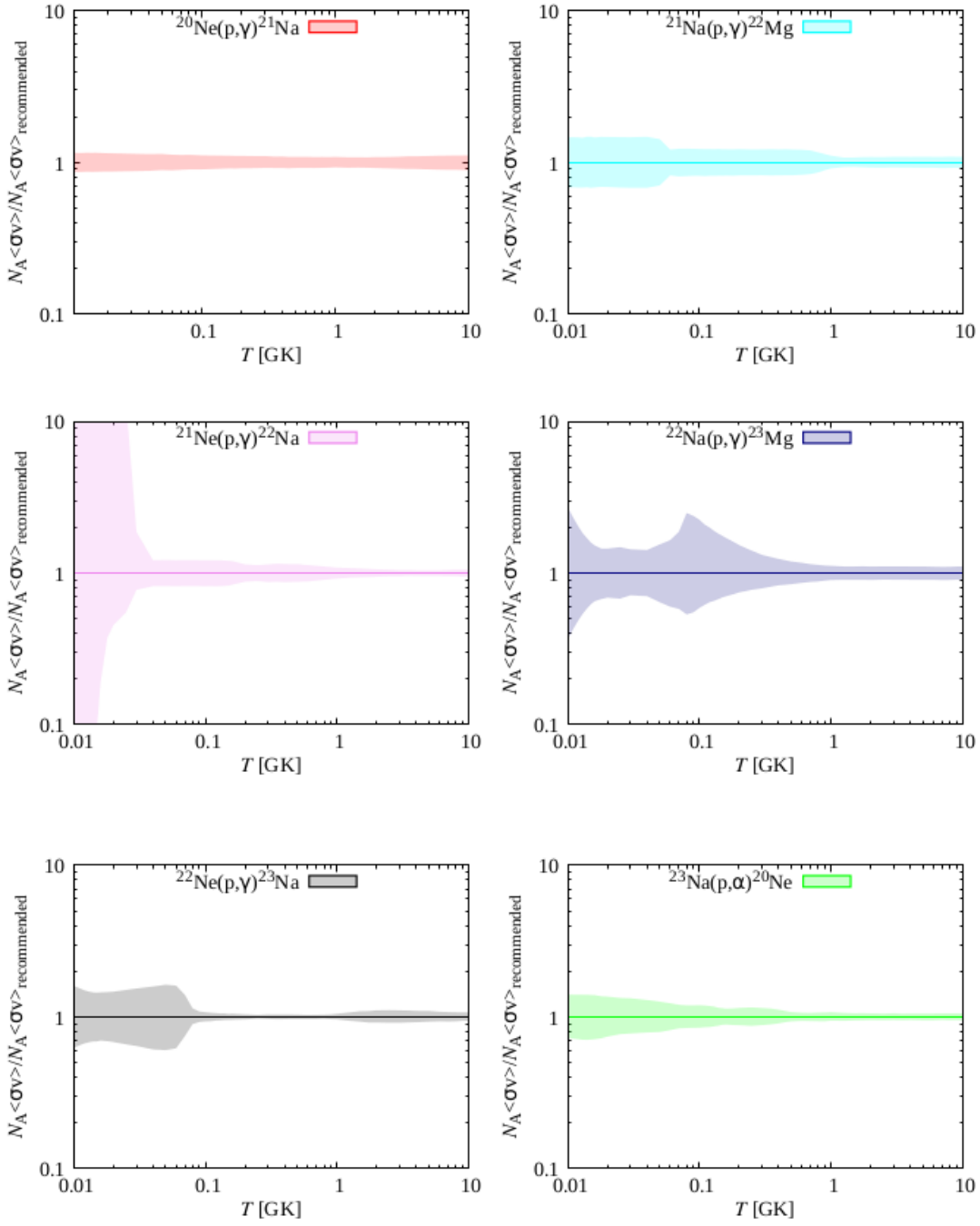


Figure 2.2: Relative thermonuclear reaction rates for all the nuclear reactions of the *NeNa* cycle. The $^{20}$Ne(p,$\gamma$)$^{21}$Na reaction rate is taken from [14], $^{22}$Ne(p,$\gamma$)$^{23}$Na from [15] and the others from [16]. Figure taken from [8].

### 2.1.1 Classical novae

In the *AGB* phase, intermediate mass stars ($0.4M_\odot \leq M \leq 11M_\odot$) undergo large mass losses because of strong interstellar winds. The progressive ejection of hydrogen uncovers more internal layers of the star and causes the rise of the surface temperature. When the temperature is high enough, the ejecta are ionized by intense ultraviolet radiation originating a *planetary nebula*; the residual core is called the *planetary nebula nucleus*. In the following and last step of the evolution, the hydrogen envelope is completely ejected and the hydrogen burning in the shell stops. The remnant is a *white dwarf*, which is a compact object sustained by an electron degenerate core. If the progenitor star has initial mass $2M_\odot < M < 9M_\odot$ the last burning stage is helium and the chemical composition of the white dwarf is carbon and oxygen (CO); instead, if the initial mass is in the range $9M_\odot < M < 11M_\odot$, the star can sustain up to carbon burning and the core is composed of oxygen and neon (ONe).

Since no thermonuclear reaction takes place in its core, the destiny of an isolate white dwarf is to cool down. Instead, if the white dwarf is in a closed binary system, it can accrete H-rich material that overflows the Roche lobe [1] of a companion low mass main sequence star (see Figure 2.3). If the white dwarf has a large mass and the accretion rate is high, the white dwarf mass can reach the Chandrasekhar mass $M \sim 1.4M_\odot$ and thermonuclear reactions are ignited. In this environment the energy generation is extremely high and the white dwarf explodes as a thermonuclear supernova (*type Ia supernovae*).

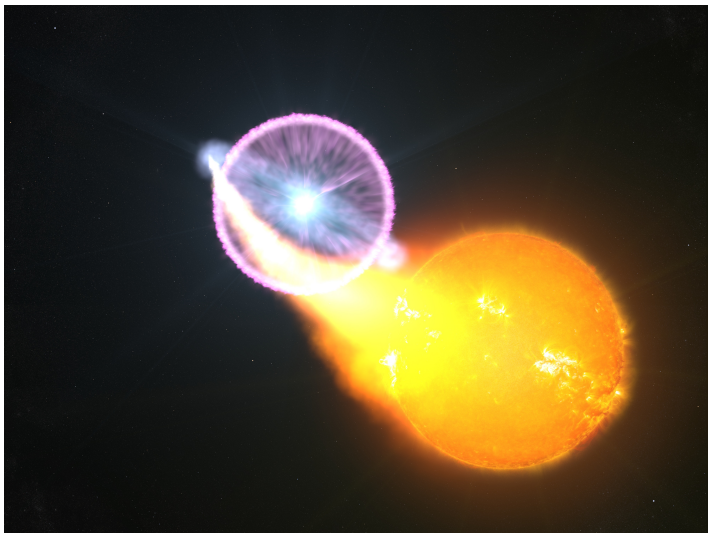

Figure 2.3: Representation of a binary system comprising a white dwarf accreting matter from a stellar companion. https://www.nasa.gov/press/2014/july/nasas-fermi-space-telescope-reveals-new-source-of-gamma-rays

Instead, if matter is transferred with a small rate ($10^{-10} - 10^{-9}M_\odot$ per year), it forms an accretion disk and only a fraction deposits on the surface of the white dwarf, where it is compressed and heated by the strong gravity. Eventually, nuclear burning is ignited (hydrogen burning proceeds firstly through *pp* chains and secondly through *hot CNO* cycles) and a thermonuclear runaway takes place. This type of explosion is called *classical novae* and it involves only the accreted layer and not the internal core. For this reason, the process can be repeated, with a recurrence of $10^4 - 10^5$ years. Classical novae are frequent phenomena, each year about 35 explosions are expected in our Galaxy, and they contribute to chemical enrichment of the Galaxy.

From observation results, the content of the ejecta in carbon, nitrogen and oxygen is larger

[1] The Roche lobe is a hypothetical surface that delimits the gravitational domain of a star.

than the solar abundances. What is more, in 1/3 of the total novae, an overabundance of neon also emerged. This enrichment of ejected matter is attributed to a mixing process with the CO or ONe core. Indeed, the composition of the white dwarf plays an important role in the nucleosynthesis of the nova explosion. From theoretical models, the temperatures in novae are high enough for burning hydrogen through the *hot CNO* cycle. If the core composition is ONe, NeNa and MgAl seed nuclei are present and nucleosynthesis proceeds up to intermediate mass nuclei. In particular, in massive white dwarfs temperatures reach values of $T \sim 400$ MK, and the burning of $^{20}$Ne becomes an efficient process. As a result, $^{22}$Na is produced through the reaction $^{20}$Ne(p,$\gamma$)$^{21}$Na, followed by the $^{21}$Na decay into $^{21}$Ne and the proton capture $^{21}$Ne(p,$\gamma$)$^{22}$Na [12]. The production of $^{22}$Na is characteristic of ONe white dwarfs and observations of its synthesis through the detection of the $E_\gamma = 1275$ keV $\gamma$ ray may allow to distinguish ONe white dwarfs from the more common CO ones. In addition, through the detection of $\gamma$ rays from novae explosions, the abundance of synthesized $^{22}$Na may be directly measured, allowing to set constrains on the nucleosynthesis [25].

Experimentally, the $E_\gamma = 1275$ keV photon emitted in the $^{22}$Na decay is observable via satellite telescope spectroscopy up to 2-3 years after the nova explosion. However, since actual instrumentation is limited to distances smaller than $\sim 1$ kpc and a successful detection would require a relative close novae explosion, the $^{22}$Na $\gamma$ line has not been observed yet [25]. Currently, a new generation of $\gamma$ ray instruments is proposed for a new mission, which may provide improved resolution and sky coverage [26], so, in the near future, experimental data may be available for a comparison with the predicted abundances.

### 2.1.2 Core-collapse supernovae

The production of $^{22}$Na in massive stars takes place mainly in the carbon burning stage, but there is experimental evidence of $^{22}$Na production through the *NeNa* cycle during core-collapse supernovae.

High mass stars ($M > 11M_\odot$) reach extreme high temperatures and, after the exhaustion of the central carbon, they are able to ignite three further burning stages in their core: neon, oxygen and silicon burning. The fuel of these advanced burning stages is provided by the ashes of the previous core burning stage and the star expands becoming a supergiant. When silicon in the center is exhausted, the core is composed of elements of the iron peak group, which have the highest binding energy per nucleon, and no successive burning stages are ignited. At this point the star has an onion-like structure: a degenerate iron core, in which degenerate electron pressure counteracts gravity, surrounded by thin concentric still active shells. Since the outer shells continue burning lighter elements, the ashes of the burning deposit on the core, increasing its mass. Eventually, the mass of the core exceeds the Chandrasekhar limit and the electron degeneracy is not able to counteract gravity, causing the core to collapse. In the collapse the density of the core rapidly increases and, when it becomes comparable to the nuclear density, the free nuclei and nucleons feel the nuclear repulsive force. The nuclear potential rebounds the matter, generating an outward shock wave. As the shock wave moves towards the star it heats up the different layers, igniting a short phase of explosive burning in which elements of intermediate and high mass are synthesized. After this explosion, called *core-collapse supernova*, the high density central core is left as a remnant: depending on its mass it becomes a neutron star or a black hole [5, 4].

In this case, the experimental observation of $^{22}$Na abundances is not feasible through $\gamma$ ray spectroscopy. Indeed, during the explosive burning stage other radioactive nuclei with $\gamma$ lines at similar energies, such as $^{56}$Ni, are produced in larger quantities. Nonetheless, important information about nucleosyntesis in explosive scenarios comes from the analysis of presolar grains, which are pieces of stardust found in primitive meteorites and interplanetary dust. The sources of these grains are identified through measurements of the isotopic abundances, but

several anomalies in the isotopic composition have been observed. In particular, some C-rich grains presented a noble gas component Ne-E(L) with nearly monoisotopic $^{22}$Ne [27]. The excess of $^{22}$Ne is attributed to the decay of $^{22}$Na originally incorporated into the grains, since noble gases do not form compound that condenses into grains [12]. The additional presence of Ti in the grains links the origin to supernovae explosions.

The difficulty in explaining the observed abundances arises from the fact that $^{22}$Na is mainly produced by carbon burning and an excess abundance is expected in environments with low carbon content. Instead, the observed C-rich grains must have originated in a C-rich environment. In [28] it is introduced a model, based on the mixing of matter between different layers of the supernova, that is able to explain the observed abundances. In this framework, it is assumed that hydrogen is incorporated in the helium shell and it is not fully consumed before the explosion. If the shock wave invests the helium shell with some hydrogen still present, the *hot CNO* cycle is activated and the amount of produced $^{22}$Na increases by orders of magnitude. This model still requires detailed calculations before quantitative results can be applied to constrain supernovae explosions and an improvement in the measurement of the $^{21}$Ne(p,$\gamma$)$^{22}$Na reaction rate is necessary to asses the role of this reaction.

## 2.2 $^{21}$Ne(p,$\gamma$)$^{22}$Na reaction

The $^{21}$Ne(p,$\gamma$)$^{22}$Na reaction is an exothermic reaction with $Q_{value}$=6739 keV. It is expected that its reaction rate is dominated by several resonances at low energies. Figure 2.4 shows the main contributions to the total reaction rate of the $^{21}$Ne(p,$\gamma$)$^{22}$Na reaction as a function of stellar temperature. As it can be seen, in the temperature range of novae ($T_9 \sim 0.3$), the reaction rate is dominated by the resonances at $E_p = 126$ and $E_p = 272$ keV, while the other resonances at $E_p = 271, 290$ and $E_p = 352$ keV are minor contributors because of their low resonance strength [2]. At higher temperatures, the three resonances at $E_p = 525, 702$ and $E_p = 768$ keV start contributing significantly [29] and they are important in supernovae scenarios ($T_9 > 0.7$). The direct capture component, from estimates, is expected to become relevant only at $T_9 > 3$ [30, 2]. Instead, the two resonances at $E_p < 100$ keV have low upper limits [16] and do not play a role at astrophysical energy.

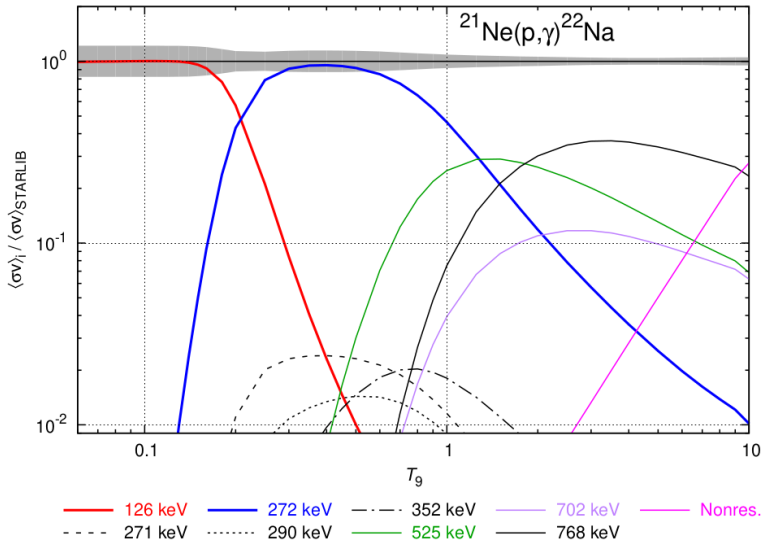


Figure 2.4: Contribution of several resonances and non-resonant capture contribution to the total reaction rate [31] of the $^{21}$Ne(p,$\gamma$)$^{22}$Na reaction. The stellar temperatures are expressed in units of $10^9$ K and the resonance energies are in the laboratory reference frame.

Consequently, the reaction rate in a given astrophysical scenario is strongly dependent on the properties of the resonances that come into play at the characteristic temperatures. Since the resonance strengths measured in previous experiments are affected by high relative uncertainties ($\sim$ 20%), a re-measurement is necessary. The objective of the actual LUNA campaign is to measure the strengths of the $E_p = 126$ and 272 keV resonances.

This thesis is focused on the doublet of resonances at $E_p = 271$ keV and $E_p = 272$ keV, which populate the $E_x = 6997.1$ keV and $E_x = 6998.1$ keV excited level of $^{22}$Na respectively. The excited levels decay schemes are shown in Figure 2.5 and 2.6. Even if the major astrophysical contribution arises from the $E_p = 272$ keV resonance, it is also important to characterize the $E_p = 271$ keV resonance. Indeed, in literature it is not known in detail and, being very close in energy to the $E_p = 272$ keV resonance, it is crucial to disentangle its contribution.

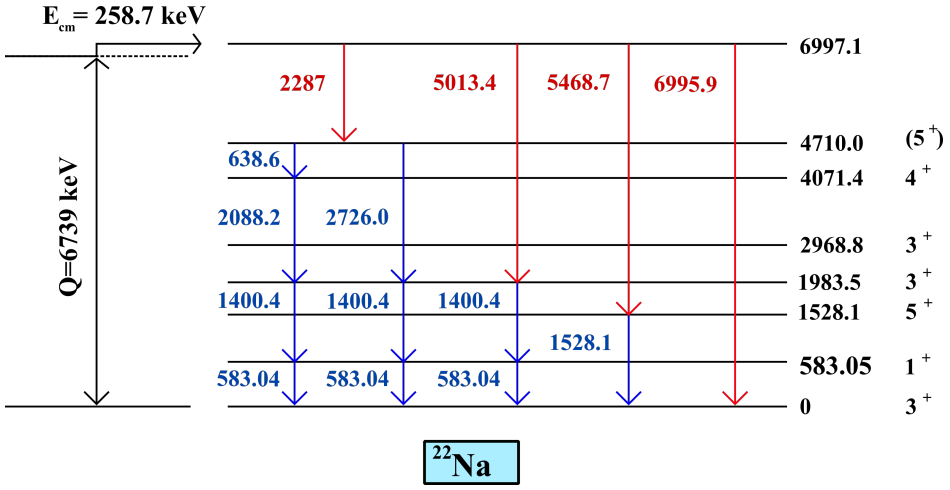


Figure 2.5: Decay scheme of the excited level of $^{22}$Na populated by the $E_p$=271 keV resonance. All the energy levels and the transitions are in units of keV. The red arrows refer to primary $\gamma$ rays, while the blue ones to secondary $\gamma$ rays. Data taken from [32].

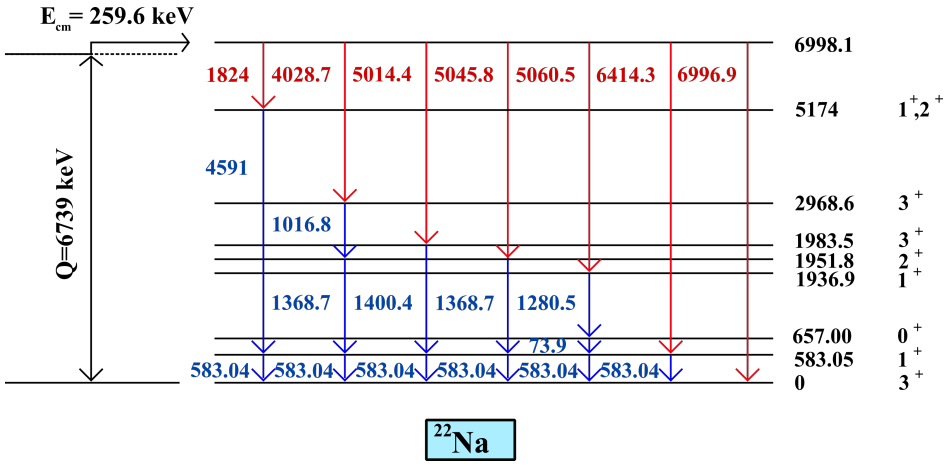


Figure 2.6: Decay scheme of the excited level of $^{22}$Na populated by the $E_p$=272 keV resonance. All the energy levels and the transitions are in units of keV. The red arrows refer to primary $\gamma$ rays, while the blue ones to secondary $\gamma$ rays. Data taken from [32].

### 2.2.1 State of the art

The $^{21}$Ne(p,$\gamma$)$^{22}$Na reaction was studied in three experiments performed between 1977 and 1983. In 1992 a fourth experiment was dedicated to the low energy resonances and successfully distinguished the two resonances of the doublet at $E_p = 272$ keV. In the following these experiments and the major results are reported.

#### H. L. Berg et al. experiment [29]

Proton induced resonances on $^{21}$Ne were studied in the energy range $E_p = 0.4 - 1.6$ MeV at the California State University in 1977. A 4 MV Van de Graaff accelerator provided proton beams of $60 - 120$ µA. The target was a differentially pumped gas target filled with neon gas enriched to 92.5% at pressure of $0.7 - 3.0$ Torr. The $\gamma$ rays produced in the reaction were observed at $\theta = 90$ ° and $\theta = 0$ ° by two Ge(Li) detectors. In some measurements only the 90° detector was used, and the other was substituted by a water cooled copper pipe capped with a Cu beam stop. A lead shield was placed between the pipe-beam stop combination and the 90° detector. Scattered protons were detected by a particle counter.

This experiment established fifteen previously reported (p,$\gamma$) resonances and discovered nineteen new (p,$\gamma$) resonances. The resonance widths, or their upper limits, have been obtained from the comparison with the shape of the narrow resonance ($\Gamma = 16$ eV) at $E_p = 1169$ keV in the $^{20}$Ne(p,$\gamma$)$^{21}$Na reaction. This was possible thanks to the residual $^{20}$Ne abundance in enriched $^{21}$Ne gas. The resonance strengths of all the observed resonances in the $^{21}$Ne(p,$\gamma$)$^{22}$Na reaction were calculated relative to the same $E_p = 1169$ keV resonance in the $^{20}$Ne(p,$\gamma$)$^{21}$Na reaction. From the properties of the observed resonances, it was calculated the influence of low energy tails on stellar reaction rate. Except for the $E_p = 702$ and 768 keV resonances, it was determined that the contribution of the other resonances is negligible due to their small resonance widths or strengths. Table 2.1 collects the properties of the $E_p = 702$ and 768 keV resonances, together with the $E_p = 525$ keV one, which due to its strength may contribute in stellar scenario.

| $E_p$ [keV] | $(2J+1)\Gamma_p\Gamma_\gamma/\Gamma$ [meV] | $\Gamma$ [keV] |
|---|---|---|
| 524.7±1.5 | 6.1±1.2 | <0.3 |
| 701.8±0.5 | 12±3 | 3.5±0.6 |
| 767.9±0.5 | 51±15 | 3.5±0.6 |

Table 2.1: Resonance strengths and widths of the main intermediate energy resonances in the $^{21}$Ne(p,$\gamma$)$^{22}$Na reaction measured in [29].

#### J. Görres et al. experiments [2, 30]

The $^{21}$Ne(p,$\gamma$)$^{22}$Na reaction was studied in Münster in 1983 [2] using a 360 keV proton accelerator which provided a beam of $80 - 300$ µA in the energy range $E_{p,lab} = 70 - 355$ keV. The experimental set up comprised a differentially pumped gas target system in which neon gas enriched to 91% $^{21}$Ne was recirculated. The beam entered the chamber through high pumping impedances and was stopped in a Faraday cup. The gas in the target was at a pressure of $p = 0.5 - 10.0$ Torr. The $\gamma$ rays produced in the reaction were detected with two 80 cm$^3$ Ge(Li) detectors, placed at $\theta = 90°$ on each side of the disc-shaped target chamber. The cap of the detectors was placed at 2.4 cm from the beam axis and, to suppress background $\gamma$ rays, the detectors were enclosed in an antimony-free lead shield with thickness $6 - 10$ cm. In this experiment, four new resonances have been discovered at $E_p = 126, 272, 291$ and 352 keV.

In addition, upper limits were set for the two resonances at $E_p$=98 and 227 keV, which are expected from the $^{22}$Na level structure. The strength of the $E_p = 272$ keV resonance was determined relative to the well known $E_p$=278 keV resonance of the $^{14}$N(p,$\gamma$)$^{15}$O reaction. A value of $\omega\gamma = (76 \pm 13)$ meV was obtained using enriched neon gas for the $E_p = 272$ keV resonance. In a similar experiment natural neon was used and the resonance strength was $\omega\gamma = (99 \pm 20)$ meV. Considering both results, it was adopted the value $\omega\gamma = (82 \pm 12)$ meV, which was used to determine the resonance strengths and the upper limits for the other resonances of the $^{21}$Ne(p,$\gamma$)$^{22}$Na reaction. These results are summarized in Table 2.2. In addition, the branching ratios for the proton unbound states are obtained from the $\gamma$ decay schemes. In table 2.3 the branching ratios relevant for the $E_p = 272$ keV resonance are reported.

| $E_p$ [keV] | $(2J+1)\Gamma_p\Gamma_\gamma/\Gamma$ [meV] | $\Gamma$ [keV] |
|---|---|---|
| 98±7 | $\leq 0.04$ | |
| 126.3±0.6 | 0.30±0.06 | $\leq 1.2$ |
| 227±6 | ≤0.04 | |
| 271.7±0.4 | 660 ± 100 | $\leq 0.1$ |
| 290.9±0.4 | 16±3 | $\leq 0.2$ |
| 352.2±0.4 | 65±11 | $\leq 0.1$ |

Table 2.2: Resonance strengths and widths of the low energy resonances in the $^{21}$Ne(p,$\gamma$)$^{22}$Na reaction measured in [2].

The following year, J. Görres et al. [30] performed another experiment with the same experimental set up using the 4 MV Dynamitron accelerator at the Universität Stuttgart. The objective was the study of the direct capture process in the $^{21}$Ne(p,$\gamma$)$^{22}$Na reaction. However, the presence of broad and strong resonances hindered the measurement of this process. Nonetheless, a new resonance at $E_p = (717 \pm 2)$ keV was discovered and it was set the upper limit $\omega\gamma \leq 0.05$ µeV on the resonance strength for the resonance at $E_p = 98$ keV.

**H. W. Becker et al. experiment [1]**

The low energy resonances at $E_p = 126, 272$ and 291 keV of the $^{21}$Ne(p,$\gamma$)$^{22}$Na reaction were studied in 1992 at the Universität Münster. A 400 kV accelerator provided high energy resolution proton beam, whose energy was varied with a computer controlled system that allowed to scan energy in steps as small as 0.4 eV. For each energy step the accumulated charge on the target was recorded. The target consisted in a Cu pipe with the axis along the beam direction and neon gas enriched to 95% in $^{21}$Ne was injected near the center of the pipe. The $\gamma$ rays produced in the reaction were detected with a germanium detector placed in close geometry to the gas target. The yield curves were studied both in thin and thick (target thickness $\gg$ resonance width) target configurations.

Scanning an energy range of 2.5 keV around the 272 keV resonance, it was observed a new weak resonance at relative distance of $(0.888 \pm 0.005)$ keV from the one already known [2]. The strength of the resonance at the $E_p = 271$ keV was obtained relative to the $E_p = 272$ keV one and it is equal to $(2J+1)\Gamma_\gamma\Gamma_p/\Gamma = (17 \pm 3)$ meV. The $\gamma$ ray spectra acquired at the peak of both these resonances showed different decay schemes and the branching ratios have been calculated for the $E_p = 271$ keV and 272 keV resonances separately. The results are reported in Table 2.3, in which the branching ratios from [2] are also displayed.

The widths of the resonances at $E_R = 126, 271, 272$ and 291 keV were re-measured, im-

| $R \rightarrow E_F$ [keV] | $BR\%$ [2] | $BR\%, E_R = 271$ keV [1] | $BR\%, E_R = 272$ keV [1] |
|---|---|---|---|
| $R \rightarrow 0$ | 51±2 | 30 ±2 | 50 ± 2 |
| $R \rightarrow 583$ | 1.8±0.2 | | 1.8±0.2 |
| $R \rightarrow 1528$ | | 5±1 | |
| $R \rightarrow 1937$ | 1.9±0.2 | | 1.9±0.5 |
| $R \rightarrow 1952$ | 29±2 | | 29±2 |
| $R \rightarrow 1984$ | 7.0±0.3 | 49±3 | 5.9±0.5 |
| $R \rightarrow 2969$ | 4.2±0.9 | | 4.2±0.9 |
| $R \rightarrow 3060$ | 0.3±0.1 | | |
| $R \rightarrow 4710$ | 0.4±0.1 | 16±2 | |
| $R \rightarrow 4771$ | 0.6±0.1 | | |
| $R \rightarrow 5174$ | 0.9±0.1 | | 0.9±0.2 |
| $R \rightarrow 5603$ | 0.5±0.1 | | |
| $R \rightarrow 5959$ | 0.3±0.1 | | |
| $R \rightarrow 5988$ | 2.1±0.1 | | |

Table 2.3: Branching ratios of the $E_p$=272 keV resonance obtained in [2] (the 272 keV doublet was not resolved) and branching ratios of the $E_p$=271 and 272 keV resonances obtained in [1].

proving the previous results by nearly two orders of magnitude. The resonance widths and energies are summarized in Table 2.4. The errors associated to resonance energies are relative and do not include absolute calibration errors.

| $E_p$ [keV] | $\Gamma$ [eV] |
|---|---|
| 126.69±0.04 | <12 |
| 270.67±0.04 | <5 |
| 271.56±0.04 | <3 |
| 290.50±0.04 | <11 |

Table 2.4: Energies and widths of low energies resonances in the $^{21}$Ne(p,$\gamma$)$^{22}$Na reaction measured in [1].

# Chapter 3

# Experimental setup

The $^{21}$Ne(p,$\gamma$)$^{22}$Na reaction was performed at LUNA, in the underground facility of the Laboratori Nazionali del Gran Sasso (LNGS).

LUNA is located in an unique environment that is particularly suited for Nuclear Astrophysics measurements: charged particle induced reactions usually have very small cross sections at energies of interest for stellar evolution and, consequently, the reaction rates are very low. For this reason, it is crucial to distinguish the signal of interest from the background. On Earth surface, indeed, it is extremely difficult to reduce the signal produced by cosmic rays and a deep underground laboratory is a preferable choice. At the LNGS, the 1400 m of dolomite rocks (equivalent to 3800 m of water) above the experimental tunnel shield against cosmic rays, reducing the muon flux by six orders of magnitude with respect to the Earth surface and the neutron flux by three [33, 34].

In its low background environment, since the installation of the first accelerator in 1991, LUNA has reached outstanding results in the Nuclear Astrophysics field [33, 35].

In the first part of this Chapter, the LUNA accelerator and the gas target are described, while the second part is dedicated to the experimental setup adopted during the $^{21}$Ne(p,$\gamma$)$^{22}$Na reaction study.

## 3.1 LUNA II 400 kV accelerator

In the first phase of LUNA, a 50 kV electrostatic accelerator [36] was used to study the nuclear reactions of interest for hydrogen burning in the Sun [33]. Then, in 2000, a second accelerator, LUNA II, was installed [37]. LUNA II covers a larger energy range and allows to study reactions involving heavier nuclei. In particular, it has been used to measure numerous reactions of the Big Bang Nucleosynthesis and of the *CNO*, *NeNa* and *MgAl* cycles. The installation of a new 3.5 MV accelerator will be completed soon and in the near future LUNA will be able to explore higher energy regions [38].

LUNA II is a 400 kV commercial electrostatic accelerator installed by the High Voltage Engineering Europe, Netherlands. The accelerator is embedded in a tank (shown in Figure 3.1), which is filled with a gas mixture, consisting of 75% $N_2$ and 25% $CO_2$, at a pressure of 20 bar.

The main components of the accelerator are an Inline-Cockcroft-Walton power supply, which is located inside the tank and provides the high voltage, and a radio-frequency ion source, which is mounted on the accelerator tube and can operate for periods of about 40 days before needing replacement.

LUNA II can provide both a proton or an helium beam, reaching high beam currents up to 1 mA for hydrogen (75% purity) and up to 500 µA for helium. Such high values of beam

Figure 3.1: LUNA II accelerator tank.

current are of fundamental importance to increase the statistics when performing reactions with very low cross sections.

A stabilization system, comprising an RC filter and an active feedback loop based on a chain of resistors, filters the high voltage at the terminal, ensuring a highly stable beam. This is a crucial characteristic, since the cross section decreases exponentially with energy and consequently even small energy changes can contribute significantly to the uncertainties in the final measurement.

The ions, after being extracted from the source by an electrode, are accelerated in the beam line and encounter firstly a vertical steering magnet and secondly an analyzing magnet. The latter can direct the beam towards one of two parallel beam lines, which are connected to two permanent setup: an extended windowless gas target and a solid target. The accelerator and the gas target beam line are shown in Figure 3.2.

The accelerator was calibrated through the $^{12}$C(p,$\gamma$)$^{13}$N proton capture reaction [37]. The obtained result was then check with (p,$\gamma$) well known resonances on $^{23}$Na, $^{25}$Mg and $^{26}$Mg. These resonant reactions were used also to determine the energy spread of the beam, which was measured lower than 100 eV. The calibration curve is a linear function of the sum of $TV$ (high voltage reading of the accelerator) and $PV$ (probe voltage of the ion source):

$$E_p = (0.9933 \pm 0.0002)\frac{\text{keV}}{\text{kV}} \cdot (TV + PV) - (0.41 \pm 0.05)\ \text{keV} \tag{3.1}$$

The uncertainty on the proton beam energy is 0.3 keV and the beam stability is better than 5 eV/h.

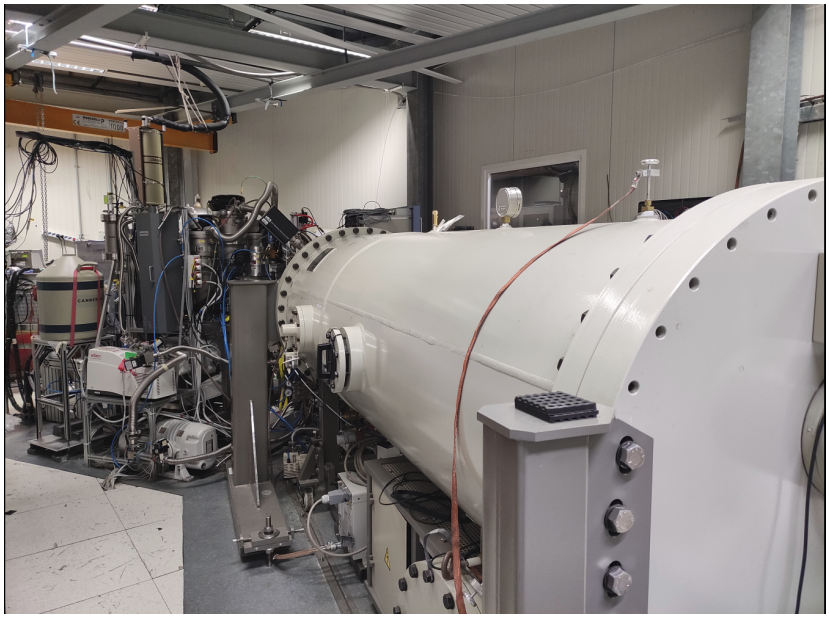

Figure 3.2: LUNA II accelerator and gas target beam line.

## 3.2 Windowless gas target

The $^{21}$Ne(p,$\gamma$)$^{22}$Na reaction was measured using the windowless gas target beam line.

The usage of a gas target offers several advantages, despite a complicate technical construction. Firstly, the gas is not affected by deterioration due to the ion beam irradiation. This is particularly important in Nuclear Astrophysics' experiments, because to increase the statistics it is necessary to irradiate the target with an intense ion beam for long time periods and therefore the target stability is a crucial parameter. Another key feature is that gas targets can reach very high isotopic purity, thus the beam induced background due to contaminants is lower. What is more, the thickness of the target can be varied modifying the gas pressure [39]. On the other hand, several issues must be taken into account. The gas density must be known precisely and it is strictly related to the pressure and the temperature. For this reason, when the experimental set up was built, an initial phase was devoted to the measurement of the pressure and temperature profiles in different regions of the scattering chamber. A contribution to the variation of the density comes from the beam heating effect, which is due to the heating and consequent thinning of the gas, when the beam loses energy passing through it. The details on the gas density calculation are given in 4.3. Another disadvantage is that the electric beam current cannot be measured using the Faraday cup method [4], because of the charge state fluctuations of the ion beam and the presence of electrons produced by the ionization of gas molecules. A solution is to measure the current using a calorimeter. A description of the calorimeter used in this experiment and of its working principle is given in 3.4.

The gas target set up adopted at LUNA is a windowless gas target. The choice of not having an entrance window is mainly driven by the necessity of avoiding beam energy loss and reducing beam energy straggling. In addition to this, an entrance window could deteriorate by beam bombardment introducing problematic uncertainties on the beam energy loss.

It is necessary to implement a differential pumping system because there is no physical barrier that divides the target chamber from the accelerator line. In fact, the beam lines of the accelerator must be kept at high vacuum (order of $10^{-7}$ mbar), while the gas inside the target is at higher pressure (order of mbar).

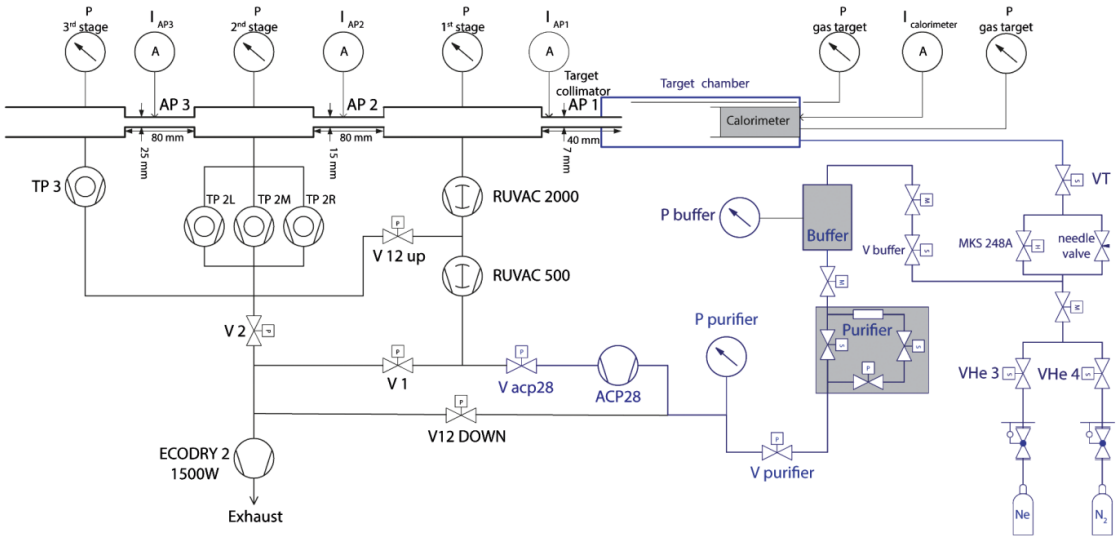


Figure 3.3: Scheme of the differential pumping system used in the windowless gas target at LUNA. The Figure is taken from [40].

Figure 3.3 shows a scheme of the differential pumping system built at LUNA.
The amount of gas that enters the chamber is driven by two valves: a needle valve, that provides a constant flux, and a MKS 248A valve, that regulates the incoming flux to keep the pressure of the target constant. These two fluxes of gas enter the same pipe and encounter another valve (VT valve) from which the gas is inserted into the chamber.

The gas pressure in the chamber is measured using two capacitance manometers, which are connected to the front and end of the chamber. The manometer connected to the end of the chamber, MKS baratron 626A, controls, via a feedback unit, the amount of gas that is injected by the MKS 248A valve. The pressure values are read and logged every two seconds by a Labview Fieldpoint 2000 system.

When the gas is inside the target chamber, it flows towards the accelerator beam line (in Figure 3.3 the beam comes from the left). Then it encounters the differential pumping system which is made of three water cooled collimators (AP1, AP2 and AP3) and three pumping stages.

The first collimator has a diameter of 7 mm and a length of 40 mm. Its dimensions were chosen as a compromise between the necessity of a high flow impedence (long aperture with a small diameter) and the requirements of the beam dimensions. After the AP1 collimator, there is the first pumping stage, which is equipped with a Roots pump (2050 $m^3/h$) backed by another Roots pump (500 $m^3/h$). In Figure 3.3 these two pumps are labeled as RUVAC 2000 and RUVAC 500. In the first stage about 99% of the gas flow is pumped out and a pressure of about two orders of magnitude lower than the target is reached.

The remaining gas may flow through the AP2 collimator and reach the second pumping stage. In this stage the pressure is low enough to allow the usage of turbomolecular pumps: using two 1000 l/s and one 1500 l/s turbomolecular pumps (labeled as TP 2L, TP 2M and TP 2R) it is reached a high vacuum pressure (about $10^{-6}$–$10^{-7}$ mbar).

Then the residual gas may flow through the third pumping stage. This stage is equipped with a turbomolecular pump (360 l/s, labeled as TP 3) and, as in the second stage, the pressure is about $10^{-6} - 10^{-7}$ mbar. After the third stage, the pressure conditions of the accelerator are met.

The gas pumped out by the three pumping stages can follow two different paths: it can be discarded and ejected as exhaust or, in case of enriched or rare gases, it can be reused after a

proper purification. In this last case, the gas lines are used in recirculation mode (V1, V2 and V12 DOWN valves closed, Vacp28 valve open). Following this path, the gas coming from the three pumping stages is compressed by a dry 27 $m^3/h$ forepump and, then, it flows towards a chemical getter (Monotorr II purifier). The purifier removes contaminations (mainly due to oxygen and nitrogen) and the purified gas is stored in a buffer. After the purifier, the gas can be injected again into the target.

The pumps and the valves (except the needle valve which is manual) are controlled by Labview. [40, 41]

The study of the $^{21}$Ne(p,$\gamma$)$^{22}$Na reaction is divided into two phases that require different gases. In the first one natural neon is used (isotopic composition 90.48% $^{20}$Ne, 0.27% $^{21}$Ne and 9.25% $^{22}$Ne). Since the natural abundance of $^{21}$Ne is extremely low, the second phase involves the usage of 59% $^{21}$Ne enriched gas. In both cases, the gas target is used in recirculating mode. Despite the low amount of $^{21}$Ne in natural neon, two resonances have been studied in the first phase and the present thesis is focused on those data.

## 3.3 Experimental set up for the $^{21}$Ne(p,$\gamma$)$^{22}$Na reaction study

The experimental set up used to perform the $^{21}$Ne(p,$\gamma$)$^{22}$Na reaction is very similar to the one that was used in the $^{22}$Ne(p,$\gamma$)$^{23}$Na reaction study [17, 40] and in the $^{20}$Ne(p,$\gamma$)$^{21}$Na one [8]. Figure 3.4 shows a diagram of the setup, which comprises a scattering chamber ($33.0\times12.0\times10.4$ $cm^3$) mounted after the AP1 aperture, two high purity germanium detectors and a calorimeter. In the following Sections the different components are described.

### 3.3.1 Germanium detectors

To detect the $\gamma$ rays produced in the $^{21}$Ne(p,$\gamma$)$^{22}$Na reaction, it is adopted a detection system based on two high purity germanium detectors (HPGe). Those are widely used because of their higher energy resolution when compared to other detectors (for example scintillators) and because of their rather high atomic number (32) that ensures a high absorption coefficient. The detectors are made of a bulk of germanium, a semiconductor crystal whose properties are exploited to extract the signal. Indeed, the electrons in a germanium crystal are disposed in a band structure, comprising a valence and a conduction band separated by an energy gap of about 1 eV. When a $\gamma$ ray interacts with the bulk material, the signal is generated by the promotion of valence electrons to the conduction band. Since the energy gap is very small, the thermal energy of the electrons is enough for the promotion from the valence to the conduction band. This leads to unwanted noise that prevents the proper functioning of the detector. To avoid this effect, germanium detectors need to be cooled, for example using liquid nitrogen [42].

The two detectors used in this experiment are labeled in the following as GePD and GeDD:

- GePD is a CANBERRA low background detector, whose relative efficiency is 130% [1]. It is mounted below the interaction chamber, at 12.71 cm from the AP1 collimator.
- GeDD is an ORTEC low background detector, whose relative efficiency is 90%. It is mounted above the interaction chamber, at 5.78 cm from the AP1 collimator.

### 3.3.2 Electronics and DAQ

The data acquisition system is driven by two different and complementary systems:

[1] The relative efficiency is considered with respect to the efficiency of a 3"·3" NaI scintillator detector for the 1333 keV $\gamma$ ray emitted in the decay of $^{60}$Co.

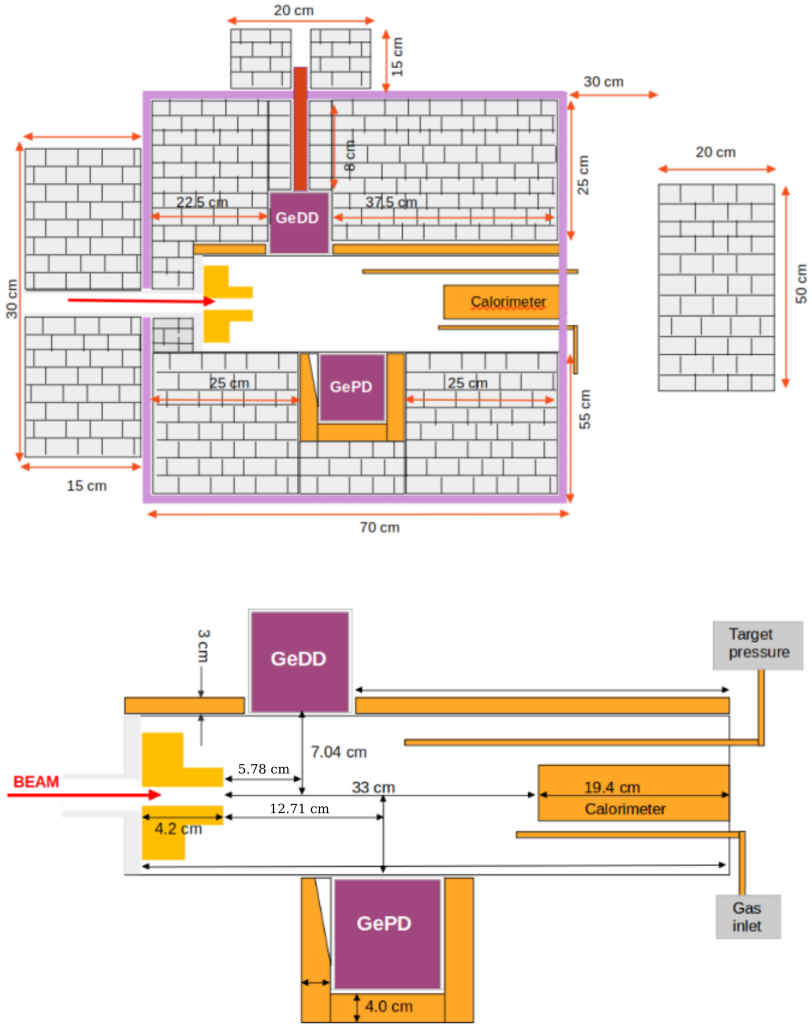


Figure 3.4: Drawing of the adopted experimental set up. In the upper panel it is shown the scattering chamber, the detectors and the different lead shields. In the lower panel it is shown a magnification of the scattering chamber and the detectors. The different passive shielding components are color coded: grey for the lead bricks, orange for the copper layers and violet for the antiradon box.

- Analogue multichannel acquisition: it records the events in histograms which can be used for offline analysis. In addition, the live time and the real time of each run are saved. The difference between these two times is that in the live time it is subtracted the contribution due to the dead time of the detector (i.e. the time window in which a signal is being acquired and another event cannot be recorded).
- CAEN digital acquisition: data are saved in list mode and the energy, timestamp and pile up of each event are stored. In this acquisition it is possible to evaluate the contribution of the dead time using a different procedure. In fact, if a pulser is connected to the acquisition system, the dead time is obtained comparing the number of pulser events acquired during a run with the frequency set in the pulser.

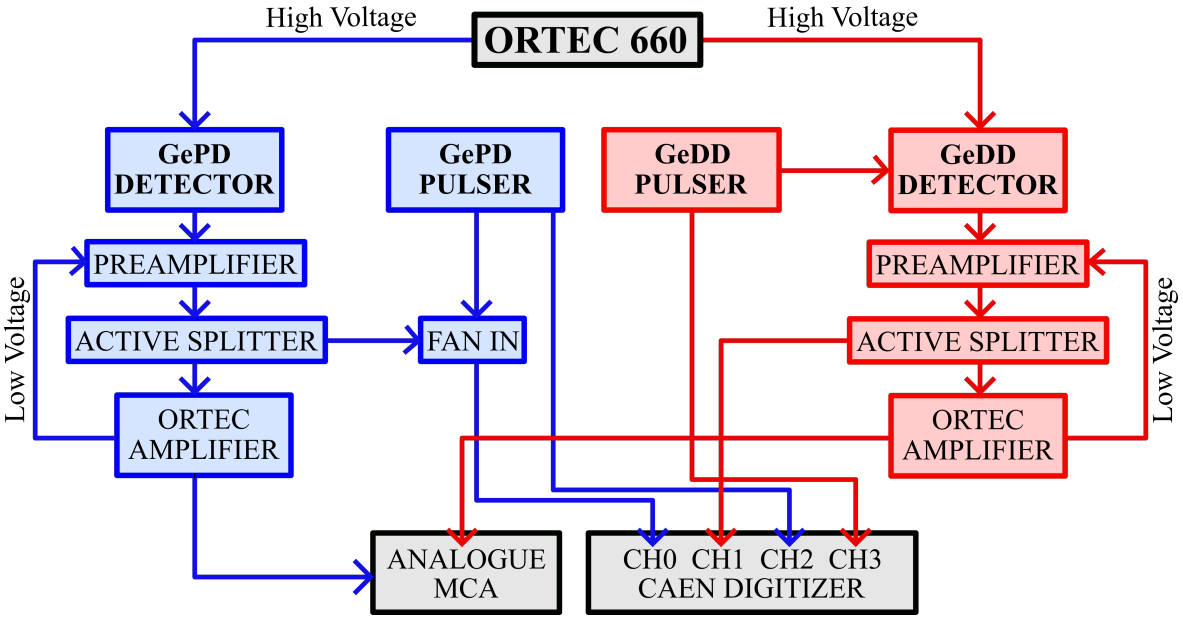


Figure 3.5: Scheme of the electronics. The blue components refer to the GePD detector, while the red ones to the GeDD detector.

Figure 3.5 shows a scheme of the electronics. An ORTEC 600 module provides the high voltage to both GePD (5 kV) and GeDD (4.8 kV) detectors. The outputs of the detectors are connected to preamplifiers, placed close to the detectors. The preamplifiers need low voltage power supply, which is provided by two ORTEC spectroscopy amplifiers (671 for GePD and 672 for GeDD).

The signals coming from the preamplifiers are sent to two active splitters: the split signals are used for the two acquisition systems. For both detectors, one of the split signals is sent to the ORTEC spectroscopy amplifier and then to the analogue multichannel analyzer. This signal is acquired using the MAESTRO software.

On the other hand, the electronics of the two detectors are slightly different for the CAEN digital acquisition. For GePD the other split signal is sent to an adder which sums it with the signal coming from the pulser. The output of the adder is connected to the ch0 of the CAEN digitizer (model N6724). For GeDD, instead, the pulser is directly connected to the detector and thus the split signal comprises already the pulser contribution. In this case there is no need of an adder and the output of the splitter is directly connected to the ch1 of the digitizer. The output of the plusers is in turn split into two signals and the one not summed to the detectors' output is directly connected to the remaining channels in the CAEN digitizer (ch2 for the pulser of GePD and ch3 for the pulser of GeDD). All the electronic modules are mounted inside a NIM crate in the accelerator room.

## 3.4 The Calorimeter

As mentioned above, when the ion beam passes through the gas in the target, the low energy ions are neutralized and the beam charge state fluctuates. In addition, in its path the beam ionizes the gas molecules, originating a large number of secondary electrons. These two effects hinder the possibility of using a Faraday cup approach to measure the beam current. As a consequence, a beam calorimeter was implemented to measure the beam current [43]. In this method, the quantity to be measured is the power deposited by the beam.

Figure 3.6: Beam calorimeter used in the experiment

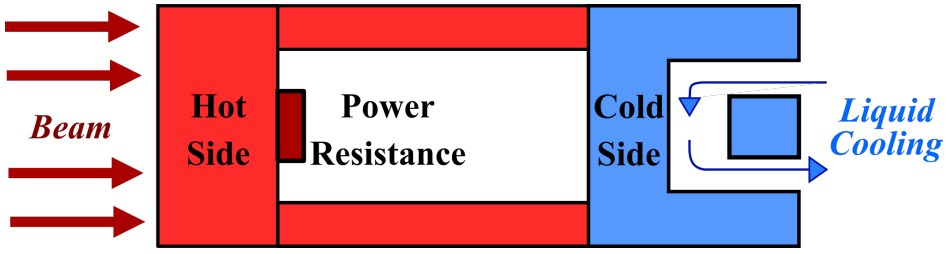


Figure 3.7: Diagram of the functioning of the beam calorimeter.

The calorimeter, shown in Figure 3.6, is a copper device that comprises two thermally coupled sides (named hot side and cold side), among which the temperature gradient is kept constant. A schematic of its components is shown in Figure 3.7. The cold side is kept at a temperature of 0° C by a cooling machine. The hot side acts as beam stopper and it is kept at a temperature of 70° C. The heat load to this latter side comes from two contributions: the ion beam that hits the calorimeter and the heat provided by heating resistors. Without the beam, the heating is entirely provided by the resistors; if the beam is on, it deposits a certain amount of heat on the beam stopper. In order to keep the temperature constant a feedback loop regulates the amount of heat produced by the resistances, diminishing or increasing the power depending on whether the beam is active or not. Operating in this configuration, the total power, given by the sum of the beam power and of the resistors power, is constant.

The temperature is read by several PT100 thermoresistors placed in different points of the calorimeter, and the values of temperature and power are read and logged every second by a Labview Fieldpoint 2000 system.

The beam intensity can be obtained as

$$I = \frac{W_0 - W_{beam}}{E_{beam} - \Delta E_{beam}} \cdot e = \frac{W_{calo}}{E_{beam} - \Delta E_{beam}} \cdot e \tag{3.2}$$

where

- $W_0$ is the power provided by the resistors when the ion beam is off. Its value is measured for several minutes before and after each acquisition run.
- $W_{beam}$ is the power provided by the resistors when the ion beam is turned on; it is lower than $W_0$.
- $W_{calo}$ is the difference between $W_0$ and $W_{beam}$ and it is the power provided by the beam.
- $(E_{beam} - \Delta E_{beam})$ is the beam energy when it reaches the hot side of the calorimeter. It is given by the difference between the initial energy of the beam and the energy loss in the gas target.

More details on these quantities are given in Chapter 4.

### 3.4.1 Calorimeter calibration

The beam intensity given in eq. 3.2 has to be corrected for the calorimeter calibration. The calorimeter calibration is necessary to associate the calorimetric power $W_{calo}$ and the electrical power $W_{el}$. These two quantities are expected to be very close: $W_{el} = C \cdot W_{calo}$ with $C \sim 1$.

To calibrate the calorimeter, the current intensity was measured using the Faraday cup method. The target chamber was evacuated and electrically connected to the calorimeter; in addition, the AP1 collimator was removed to improve the vacuum value. The total charge that reached the chamber and the calorimeter was measured using a current integrator and a counter unit. The electrical power is obtained as

$$W_{el} = \frac{E_p \cdot I_{target}}{q_e} \tag{3.3}$$

where $E_p$ is the energy of the proton beam, $I_{target}$ is the measured current intensity and $q_e$ is the charge state of the beam.

The experimental set up adopted to study the $^{21}$Ne(p,$\gamma$)$^{22}$Na reaction is the same of the $^{20}$Ne(p,$\gamma$)$^{21}$Na reaction, which was previously measured at LUNA [8]. Therefore, the calibration performed during the $^{20}$Ne(p,$\gamma$)$^{21}$Na reaction data taking campaigns is also used for the $^{21}$Ne(p,$\gamma$)$^{22}$Na study.

The calorimeter was calibrated in February 2020 and, with an improved vacuum set up, in October 2020, during the first $^{20}$Ne(p,$\gamma$)$^{21}$Na data taking campaign. In October, the measurement was performed with a vacuum value of $10^{-5}$ mbar in the target chamber and varying the beam energy in the range 50 keV to 390 keV. Since the beam current was higher than 450 µA, the calorimeter hot side was set at 80° C and the cold side at -15° C. Several runs were acquired in this configuration. The $W_0$ values were acquired for long periods before and after the measurements with the beam. All the values $W_0$, $W_{beam}$ and $W_{el}$ are taken as the average value over the entire run.

The $W_{el}$ values show a linear trend with respect to $W_{calo}$ and the data points were fitted using the following relation:

$$W_{el} = m \cdot W_{calo} + q \tag{3.4}$$

The experimental points and the fitting functions are shown in Figure 3.8. The calorimeter calibration used in this thesis is the one obtained considering both February and October data sets. The value of the slope is $m = (0.986 \pm 0.002)$ and the offset is $q = (-0.2 \pm 0.1)$ W.

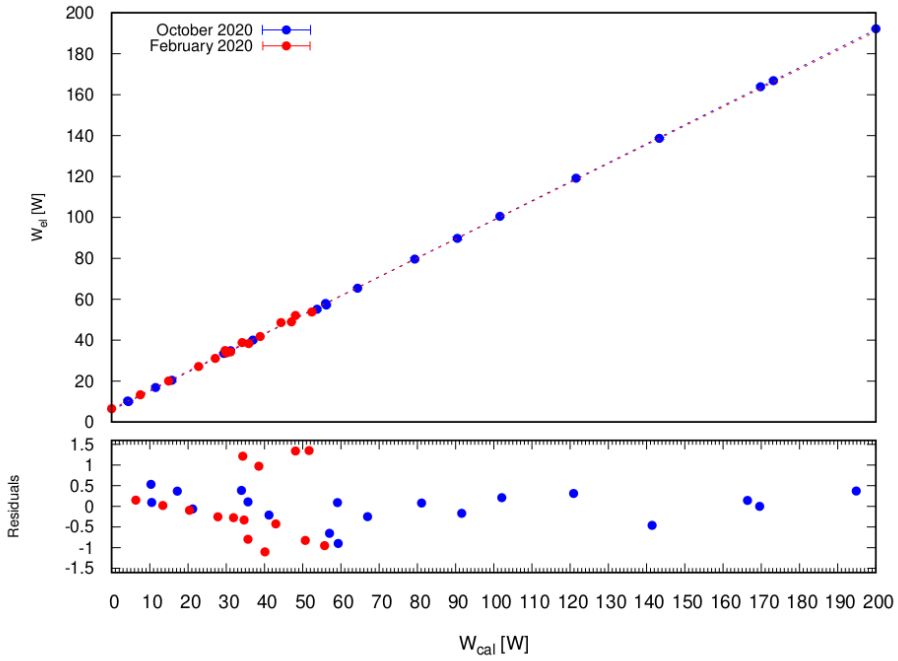


Figure 3.8: Calorimeter calibrations performed using the data acquired in February and October 2020. The lower panel shows the residuals of the linear fits. Figure taken from [8].

## 3.5 Background at LUNA

The background sources that contribute to experiments performed at LUNA can be mainly divided into two different categories: the laboratory background and the beam induced background. The laboratory background is due to cosmic rays and natural radioactivity, while the beam induced background is generated by the interaction of the ion beam delivered by the accelerator with contaminants or passive materials.

### 3.5.1 Laboratory background

The signal produced by cosmic rays contributes to the background in $\gamma$ ray spectra at energies above 3 MeV. After the interaction with the Earth atmosphere, the composition of cosmic rays at sea level is dominated by muons. Muons are highly penetrating particles and can produce detectable signals through several processes: the energy loss while traversing the detector, the production of energetic electrons and subsequent secondary electrons and $\gamma$ radiation, and the interaction with the material surrounding the detector. Muons are also responsible for neutron production through spallation reactions [39]. As mentioned above, the rock surrounding the laboratory reduces the cosmic rays flux. Figure 3.9 shows the reduced background signal in the underground LUNA laboratory in comparison to the one acquired on Earth surface. A five orders of magnitude reduction for the signal in the $\gamma$ spectrum is visible.

On the other hand, natural radioactivity produces $\gamma$ rays of energies lower than 2.6 MeV. The origin of this type of radiation is mainly connected to $^{40}$K, and the decay chains of $^{238}$U and $^{232}$Th, which are present in the rocks of the experimental halls and in the experimental set up. Their contribution can be reduced through passive shielding (low radioactive lead and copper) of the experimental set up. In an underground laboratory, where the cosmic rays interactions are extremely reduced, it is possible to adopt passive shielding thicker than the

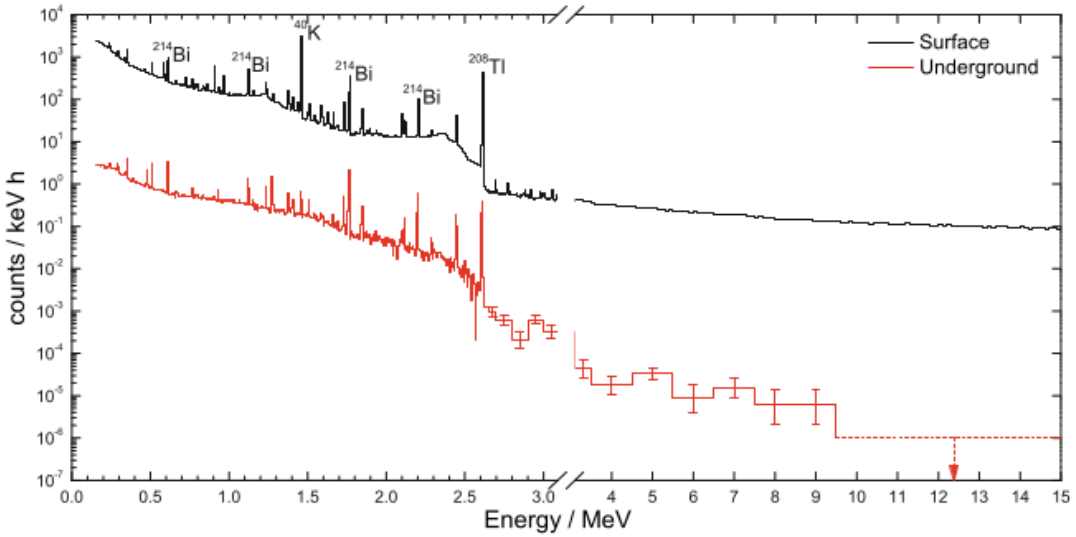


Figure 3.9: Comparison of the spectra of environmental background acquired with a high purity germanium detector on Earth surface and in the LUNA laboratory. In the underground measurement, the detector was shielded with lead and copper. Figure taken from [39].

ones used on Earth surface, where it is necessary to take into account the possibility that muons may interact with the shielding material generating additional radiation.

Another source of $\gamma$ rays is the decay of radon gas. It is possible to limit its contribution to the background using dedicated anti-radon boxes: both the target and the detector are enclosed in airtight containers flushed by radon free gas.

In addition, background signal may arise also from neutrons, which are produced by spontaneous fission of $^{238}$U and ($\alpha$,n) reactions (triggered by the $\alpha$ particles produced by the decay chains of $^{238}$U and $^{232}$Th). [44]

Eventually, a contribution that must be carefully examined in each case comes from the internal radioactivity of the detectors used in the experiment.

To reduce the contribution of the laboratory background, in the $^{21}$Ne(p,$\gamma$)$^{22}$Na reaction study, both the gas target and the detectors are surrounded by a passive shield made of several components:

- **Lead shielding**. This shield is built to reduce the contribution of $\gamma$ rays coming from the environment of the underground laboratory. The scattering chamber and the detectors are inside a castle made of lead bricks. Since the rear part of the scattering chamber cannot be enclosed in the lead castle, an additional external lead wall is built on this side in order to allow the opening of the chamber and the removal of the calorimeter. Another background contribution may arise from the interaction of the proton beam with the AP2 collimator. For this reason another lead shield is built between the first pumping stage and the main castle.
- **Antiradon box**. To reduce the background induced by the decay of radon gas, the main lead castle is encapsulated in an antiradon box, which is made of an airtight plexiglass container in which nitrogen is flushed in overpressure. This prevents the entrance of argon inside the castle.
- **Copper shielding.** This shield has the role of reducing the signal induced by the radioactive isotope $^{210}$Pb present in the lead shielding. In fact, the daughter nucleus of $^{210}$Pb is $^{210}$Bi, which in turn decays $\beta^-$ emitting electrons. These electrons can produce $\gamma$ rays through the bremsstrahlung mechanism. The GePD detector is surrounded by

a 4 cm copper layer on the sides that do not face the scattering chamber. In addition, a 3 cm thick layer of copper is positioned between the upper part of the scattering chamber and the lead shielding.

In Figure 3.10 the lead wall, the chamber closed with the calorimeter flange, the lead castle and the antiradon box are visible.

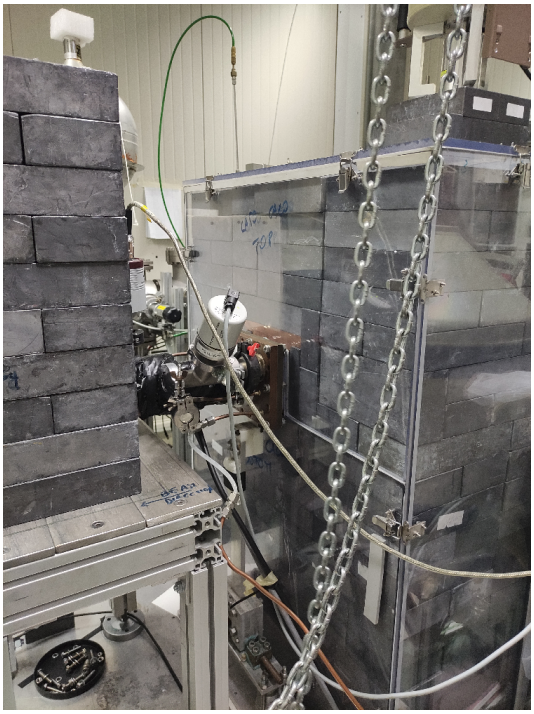

Figure 3.10: Photo of the rear part of the target chamber. On the left, it is visible the lead wall. The chamber is closed with the calorimeter flange and it is surrounded by the lead castle and the antiradon box.

### 3.5.2 Beam induced background

The beam induced background stems from the interaction of ion beam particles with contaminants which may be present in the target or in the surrounding material. It is independent of the laboratory depth, but depends on the beam energy. In general, the major contribution to beam induced background comes from light contaminants (atomic number lower than the target of interest). This is because heavier elements have higher Coulomb barriers, which lower the probability of producing a reaction.

The beam induced background can be reduced through a meticulous choice of the materials and components used in the target and in the experimental set up. It is crucially important to identify all the possible contribution of beam induced background.

A more detailed analysis of the experimental spectra acquired during the $^{21}$Ne(p,$\gamma$)$^{22}$Na reaction measurement is given in Chapter 4.

# Chapter 4

# Data analysis

As mentioned previously (see Chapter 2), this thesis is focused on the two resonances at $E_p$=271 keV and $E_p$=272 keV of the $^{21}$Ne(p,$\gamma$)$^{22}$Na reaction and the objective is to determine their resonance energy and strength. Since these two resonances are very close in energy, it is not possible to resolve them with the adopted experimental setup and they are both populated in the same run. The separation of the contributions coming from the $E_p$=271 keV and $E_p$=272 keV resonances is done through a detailed analysis of the $\gamma$ rays emitted in the de-excitation process.

In this Chapter, it is reported the analysis of the experimental data and, eventually, the obtained results are shown.

## 4.1 Measurement details

The study of the $E_p$=271 keV and $E_p$=272 keV resonances of the $^{21}$Ne(p,$\gamma$)$^{22}$Na reaction is performed with the resonance scan method. A resonance is populated if the energy of the beam summed to the $Q_{value}$ of the reaction matches the energy of the excited level of the compound nucleus. In the gas target, the energy of the proton beam $E_p$ in a given point of the scattering chamber depends on the initial energy of the beam $E_{beam}$ and on the energy loss $\Delta E_{beam}$ in the gas up to that point: $E_p = E_{beam} - \Delta E_{beam}$. Thus, varying the beam energy, it is possible to populate the resonance in different positions of the scattering chamber. In Figure 4.1 it is shown a scheme of the variation of the beam energy as it passes through the gas target.

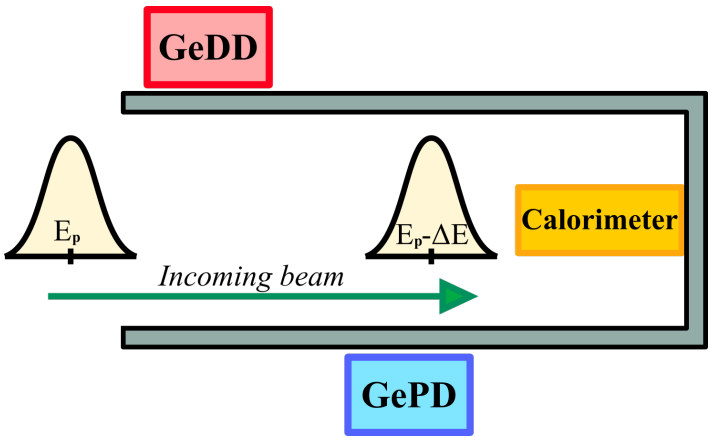


Figure 4.1: Diagram of the variation of the proton beam energy as the beam passes through the gas target.

In the experiment, two germanium detectors are used. Their efficiency depends, among other factors, on the distance of the $\gamma$ ray source from the detector and it increases closer to the detector. For this reason, the resonant yield curve reaches a maximum if the resonance is populated in front of the detector. The scan is performed acquiring long runs at different beam energies (1 keV steps).

The data taking for the $^{21}$Ne(p,$\gamma$)$^{22}$Na reaction study is split into campaigns, each one several weeks long. At the moment two campaigns, in which natural neon gas was used as target, are already completed:

- Summer campaign, June - July 2022
- Autumn campaign, October - November 2022

Another campaign, in which the enriched $^{21}$Ne gas will be used, is scheduled in Summer 2023.

The data analyzed in this thesis were acquired during the Autumn 2022 campaign, using the analogue multichannel acquisition mode.

## 4.2 Yield of a resonant reaction

The objective of nuclear astrophysics experiments, as already mentioned in Chapter 1, is the calculation of reaction rates at energies relevant for stellar evolution. The quantity that plays a fundamental role in the calculation of the reaction rates is the cross section, which, however, is not directly measurable. Instead, the quantities obtained experimentally are the number of reactions and the number of incident particles. The ratio of these two values is called yield and it is related to the cross section:

$$Y = \frac{\text{total number of reactions}}{\text{total number of incident particles}} = \frac{N_R}{N_B} \tag{4.1}$$

This expression can be rewritten in terms of quantities that can be directly measured

$$Y = \frac{N_{counts}}{N_B \eta BRW} \tag{4.2}$$

where $N_{counts}$ are the number of counts acquired by the detector for a determined $\gamma$ peak, $\eta$ is the detection efficiency, $BR$ is the branching ratio and $W$ is the angular distribution.

Working in the center of mass reference frame, it is possible to make explicit the relation between the yield and the cross section considering the target composed of several slices, each $\Delta x_i$ thick. Given an incident beam of energy equal to $E_0$, the cross section $\sigma_i$ and the stopping power $\epsilon_i$ can be considered constant over the slice if the energy loss $\Delta E_i$ in each slice is small. The yield in the i-th slice $\Delta x_i$ can be written as

$$\Delta Y_i = \frac{\text{total number of reactions in the i-th slice}}{\text{total number of incident particles in the i-th slice}} = \sigma_i N_i \Delta x_i \tag{4.3}$$

where $N_i$ is the number density of atoms in the slice.

The total yield is obtained integrating over all the target slices:

$$Y(E_0) = \int \sigma(x) N(x) dx = \int \sigma(x) N(x) dx \frac{dE(x)}{dx} \frac{dx}{dE(x)} = \int_{E_0 - \Delta E}^{E_0} \frac{\sigma(E)}{\epsilon(E)} dE \tag{4.4}$$

where $\Delta E$ is the total energy lost inside the target and $\epsilon(E) = -(1/N)(dE/dx)$ is the stopping power in units of (eV cm$^2$)/atom. Whether this integral is analytically solvable or not depends on the expression of the cross section.

In the case of isolated and narrow resonances, such as the ones analyzed in this thesis, the cross section is a Breit Wigner function (eq. 1.17). If the resonance is narrow, the stopping

power $\epsilon$, the de Broglie wavelength $\lambda$ and the partial width $\Gamma_i$ can be considered constant over the resonance width and equal to the values they acquire at the resonance energy $E_r$[1]. Inserting the expression eq. 1.17 of the cross section into eq. 4.4, the yield for a narrow resonance is given by

$$Y(E_0) = \int_{E_0-\Delta E}^{E_0} \frac{1}{\epsilon(E)} \frac{\lambda^2}{4\pi} \omega \frac{\Gamma_a \Gamma_b}{(E_r - E)^2 + \Gamma^2/4} dE \tag{4.5}$$

Solving the integral

$$Y(E_0) = \frac{\lambda_r^2}{2\pi} \frac{\omega\gamma}{\epsilon_r} \frac{\Gamma}{2} \int_{E_0-\Delta E}^{E_0} \frac{dE}{(E_r - E)^2 + (\Gamma/2)^2} =$$

$$= \frac{\lambda_r^2}{2\pi} \frac{\omega\gamma}{\epsilon_r} \left[ \arctan\left( \frac{E_0 - E_r}{\Gamma/2} \right) - \arctan\left( \frac{E_0 - E_r - \Delta E}{\Gamma/2} \right) \right] \tag{4.6}$$

where the definition $\omega\gamma = \omega\Gamma_a\Gamma_b/\Gamma$ has been introduced.

Eq. 4.6 assumes a simpler form if the target can be approximated as infinitely thick. This condition is verified if $\Delta E \gg \Gamma$, where $\Delta E$ is the target thickness in energy and $\Gamma$ is the total resonance strength. In this case the yield is given by the following expression:

$$Y_{\Delta E \to \infty}(E_0) = \frac{\lambda_r^2}{2\pi} \frac{\omega\gamma}{\epsilon_r} \left[ \arctan\left( \frac{E_0 - E_r}{\Gamma/2} \right) + \frac{\pi}{2} \right] \tag{4.7}$$

and the maximum yield is

$$Y_{max} = \frac{\lambda_r^2}{2} \frac{\omega\gamma}{\epsilon_r} \tag{4.8}$$

The de Broglie wavelength in the center of mass can be numerically calculated once the resonance energy in the laboratory ($E_r^{lab}$) and the masses of projectile and target ($M_0$ and $M_1$ respectively) are known:

$$\frac{\lambda_r^2}{2} = 2\pi^2 \frac{\hbar^2}{2 m_{01} E_r} = \left( \frac{M_0 + M_1}{M_1} \right)^2 \frac{4.125 \times 10^{-18}}{M_0 E_r^{lab}} \tag{4.9}$$

In the eq. 4.9, the resonance energy is in the laboratory frame and it is in units of eV; the factor $(M_0+M_1)/M_1$ is introduced to pass from the laboratory to the center of mass reference frame and $m_{01}$ is the reduced mass of the projectile-target system. In the equation the masses are in atomic mass units. [5]

## 4.3 Target density

The first quantity that is fundamental to determine precisely the cross section is the target density. Indeed, it is necessary to calculate the beam energy loss in the target and the integrated charge deposited by the beam. What is more, the difference between the beam energy and the energy loss determines the position inside the chamber at which the resonant state is populated.

The gas density is obtained through the ideal gas law

$$pV = nRT \tag{4.10}$$

where $p$ is the pressure, $V$ the volume, $n$ the amount of substance and $R$ is the ideal gas constant. An important issue that must be taken into account is that pressure and temperature may depend on the position inside the chamber. The dependence of the temperature,

[1] The values calculated at the resonance energy are labeled with the subscript $r$.

in particular, is more relevant when the current is obtained using the calorimeter approach (see Section 3.4) in which it is introduced a temperature gradient between the hot side of the calorimeter and the water cooled AP1 collimator.

Using the coordinate $z$ to indicate the position in the chamber along the beam line, the target density in units of atoms/cm$^3$ can be written as

$$\rho(z) = \frac{p(z)N_A}{RT(z)} \tag{4.11}$$

where, in addition to the quantities introduced in eq. 4.10, $N_A$ is the Avogadro constant.

The experimental setup is designed in such a way that the two germanium detectors are placed in a region of constant gas density [40]. Nonetheless, both the pressure and temperature profiles were studied in a preliminary phase.

### 4.3.1 Pressure and temperature profiles

As mentioned above, the experimental setup for the study of the $^{21}$Ne(p,$\gamma$)$^{22}$Na reaction is the same that was adopted for the $^{22}$Ne(p,$\gamma$)$^{23}$Na reaction [17]. During the construction of the setup, the gas pressure and temperature profiles have been measured without the beam. For this purpose, it is used a mockup chamber identical to the one used in the experiment, but equipped with eleven flanges to which it is possible to connect pressure and temperature gauges. A scheme of the mockup chamber is shown in Figure 4.2.

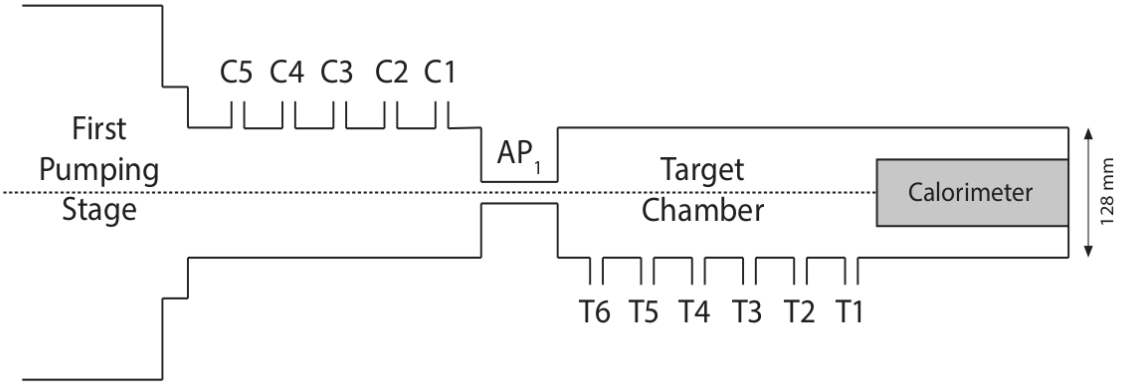


Figure 4.2: Diagram of the mockup chamber used to calculate the pressure and temperature profiles. Six of the flanges used for the measurement are located in the chamber and five between the first pumping stage and the AP1 collimator. Figure taken from [20].

During the measurement, the AP1 collimator was water cooled to a temperature of 290 K while the hot side of the calorimeter was kept at a temperature of 343 K. The data acquisition was repeated for several values of the gas pressure inside the chamber, ranging from 0.5 mbar to 5 mbar. The pressure is measured using four capacitance manometers and the temperature using four Pt100 thermoresistors. These latter were mounted on long wires and placed at the center of the chamber. Since the measuring devices were less than the flanges, the profiles are obtained measuring in the same gas condition and mounting the manometers and thermoresistors in different flanges. Figure 4.3 and 4.4 show the pressure and temperature profiles respectively. The pressure is flat inside the chamber, while it decreases of about a factor 30 inside the AP1 collimator. The temperature, instead, decreases monotonically from the hot side of the calorimeter to the AP1 collimator. From the experimental data it was estimated that the pressure contributes with a 1.0% to the uncertainty on the gas density profile while

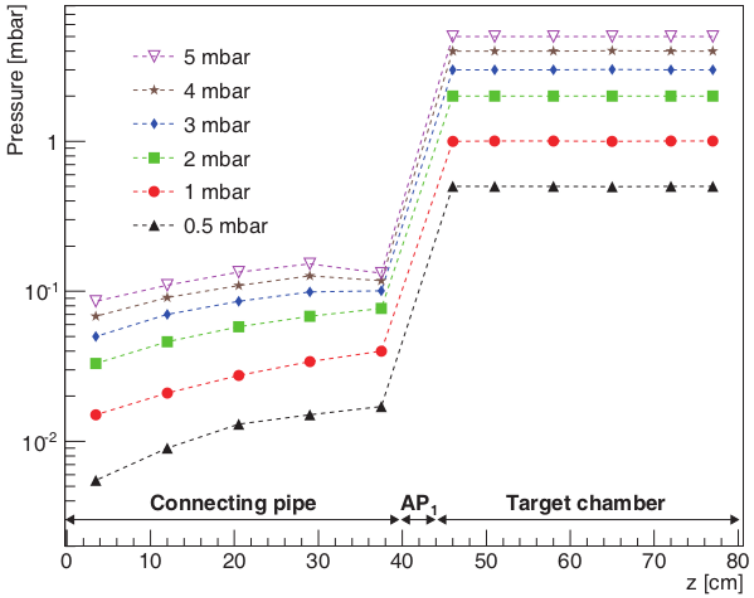


Figure 4.3: Pressure inside the gas target chamber as a function of distance $z$ from the aperture AP2. The profiles are obtained for different target pressures, plotted in different colors. Figure taken from [40].

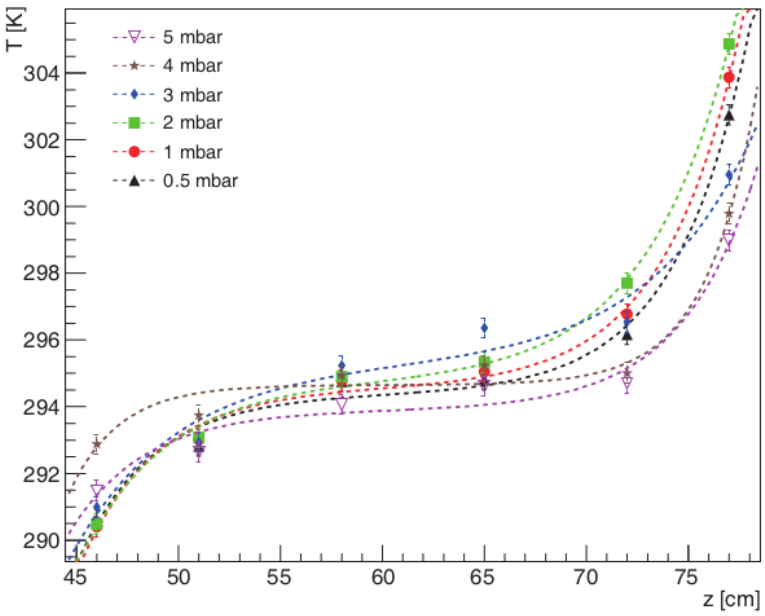


Figure 4.4: Temperature inside the gas target chamber as a function of distance $z$ from the aperture AP2. The profiles are obtained for different target pressures, plotted in different colors. Figure taken from [40].

the temperature with a 0.4%. More details on this measurement can be found in [40, 20, 21].

In the $^{21}$Ne(p,$\gamma$)$^{22}$Na reaction Autumn campaign, the pressure of the natural neon gas inside the chamber is kept constant at 2 mbar by the feedback system. The temperature of the gas $T = (295.1 \pm 1.1)$ K, instead, is obtained as the mean value of the temperatures in the T3 and T4 flanges (see Figure 4.2) measured in the temperature profile study with the gas at 2 mbar [20].

### 4.3.2 Energy loss

The passage of a charged ion through matter is characterized by energy loss and deflection. These two processes are mainly due to inelastic collisions with the atomic electrons (causing excitation and ionization) and, more rarely, elastic scattering from nuclei. The energy transferred in each of these collisions is usually a small fraction of the initial ion energy but, given that many interactions take place per unit path length, the ion energy loss is due to the cumulative effect.

The stopping power $dE/dz$ is the average energy loss per unit path length and it is well described by the Bethe-Bloch formula. $dE/dz$ depends on both the energy and the charge of the incoming ion, and the charge and the mass number of the medium. A convenient way of expressing the stopping power is in terms of the mass stopping power: in this case $dE/dz$ is divided by the density of the material and it is measured in units of eV·cm$^2$/g. [45]

It is possible to calculate the stopping power for different proton beam energies in neon using SRIM [46], which is a software package that provides the stopping and the range of ions in matter. The calculations made by SRIM are based on a database of experimental data which is regularly updated [47]. Figure 4.5 shows the stopping power of protons in a gaseous neon target. The uncertainty associated to the calculated stopping power for protons in neon is 1.7%.

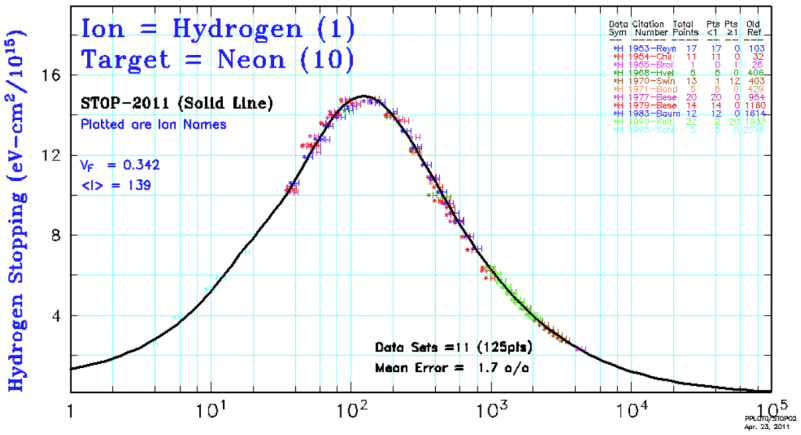


Figure 4.5: Energy loss of protons in neon gas. Figure taken from [48].

The energies of the proton beam used in the $^{21}$Ne(p,$\gamma$)$^{22}$Na reaction study range between 272 and 288 keV. In this small energy interval, the stopping power values follow a linear trend. Since the proton energy steps used in the measurement are small, the stopping power of all the energies of interest is not evaluated by SRIM. To obtain the energy loss for all the proton energies, it is adopted a two step process. Firstly, in a range close to the energy of interest, the SRIM values are fitted with a linear function. Then, the fitting coefficients are used to calculate the stopping power of energies comprised between the available energies.

### 4.3.3 Beam heating correction

As mentioned in the previous Section, the proton loses energy when it passes through the gas target. As a consequence, the gas is heated and, according to eq. 4.11, the density decreases. This effect is called beam heating and, previously to neon gas, it was studied for $^{14}$N [49, 50] and $^{3}$He [51] gases.

The beam heating on neon was studied using the resonance scan method, which exploits the fact that the beam energy loss depends on the gas density and that narrow resonances are populated at fixed energies. Thus, variations of the beam energy correspond to the population of the resonance in different positions along the scattering chamber. To perform this measurement, similarly to the measurement of the temperature and the pressure profiles, it was used a mockup chamber [40]. Figure 4.6 shows a diagram of the setup: a NaI scintillator detector, shielded with lead, was mounted on a movable support, and it was used to acquire the $\gamma$ rays emitted by the $E_{p,res}$= 272 keV resonance produced by protons on $^{21}$Ne. The gas target was filled with natural neon.

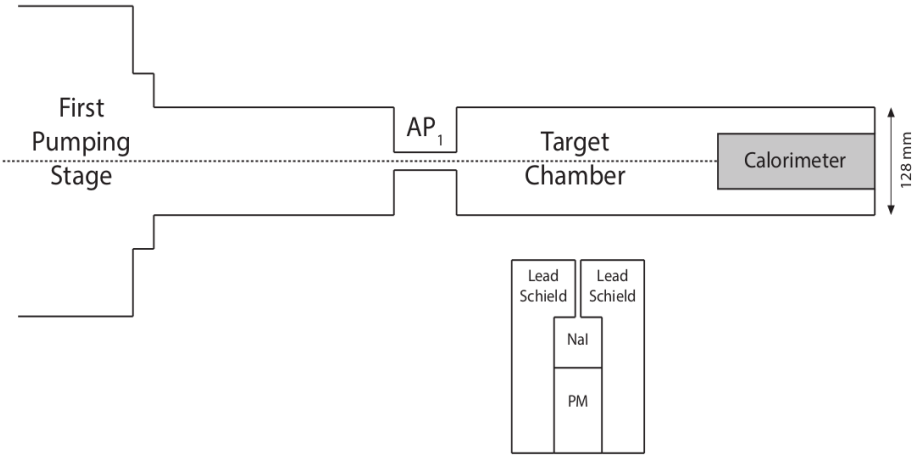


Figure 4.6: Diagram of the mockup chamber used to study the beam heating effect on the neon gas target. Figure taken from [20].

When the resonance is populated in front of the detector, the resonant yield curve has a maximum at $E_{p,max}$, and the energy loss in the scattering chamber can be obtained as

$$\Delta E_p^{exp}(p_T, I) = E_{p,max} - E_{p,res} \tag{4.12}$$

where $p_T$ is the pressure in the target chamber and $I$ the beam current. The ratio of the gas density without beam $n_0$ and the gas density with beam $n$ is given by

$$\frac{n}{n_0} = \frac{\Delta E_p^{exp}(p_T, I)}{\Delta E_p^{exp}(p_T, 0)} \tag{4.13}$$

where $\Delta E_p^{exp}(p_T, 0)$ is the energy loss obtained extrapolating the energy loss curve to $I$= 0 µA [40]. The $n/n_0$ measurement was repeated in different configurations: the NaI detector was placed in two different positions, the gas pressure values were set to $p_T$= 0.5, 2.5 and 4 mbar, and the beam intensity was varied between 30 and 260 µA.

The previous studies [49, 50, 51] reported that the beam heating is proportional to the dissipated power per unit length

$$\frac{dW}{dx} = \frac{dE}{d(nx)} nI \tag{4.14}$$

where $dE/d(nx)$ is the energy loss of protons in neon gas obtained with SRIM [46] and $n$ is the gas density.

The experimental values obtained in the measurement with neon gas confirmed the linear trend. The values of $n/n_0$ (eq. 4.13) as a function of the power deposited by the proton beam per unit length $dW/dx$ were fitted with a linear function and the ratio $n/n_0$ is given by

$$\frac{n}{n_0} = 1 - \alpha \cdot \frac{dW}{dx} \tag{4.15}$$

where $\alpha = (0.44 \pm 0.05) \cdot 10^{-3}$ and $dW/dx$ is in units of mW/cm. As for the pressure and temperature profiles, more details on the measurement can be found in [40, 20, 21].

Since in eq. 4.14 the dissipated power per unit length is a function of the current, the beam heating correction is obtained in a recursive fashion. Firstly, it is calculated the current using the gas density without beam. Then, using this current value, it is calculated the dissipated power per unit path length. The value of $dW/dx$ is inserted in eq. 4.15, from which it is obtained the ratio $n/n_0$. Eventually, it is recalculated the current using the gas density with beam $n$.

## 4.4 Beam current and integrated charge

Once the density and the stopping power are known, it is possible to calculate the beam current using eq. 3.2. The energy loss $\Delta E_{beam}$ in eq. 3.2 is obtained as

$$\Delta E_{beam} = \frac{dE}{dx} \cdot n \cdot \Delta x \tag{4.16}$$

where $dE/dx$ is the stopping power from SRIM in unit of (eV cm$^2$)/($10^{15}$ atoms), $n$ is the target density and $\Delta x$= (36.8 $\pm$ 0.5) cm is the effective scattering chamber length.

The integrated charge corrected for beam heating $Q$ is obtained multiplying the beam current by the livetime $LT$ (in seconds):

$$Q = I \cdot LT \tag{4.17}$$

The values of the charge calculated using this procedure are reported in Table 4.1. The associate uncertainty takes into account the systematic uncertainty on the pressure, the temperature, the energy loss, and the errors associated to the calorimeter calibration coefficients and beam heating coefficients. In addition, it is considered also the statistical uncertainty on $W_0$. If different runs are acquired at equal energy (i.e. the energy difference is smaller than 0.3 keV, see 3.1), they are summed.

| $E_p$ [keV] | Q [mC] |
|---|---|
| 273.0 | 2829 ± 19 |
| 274.1 | 9884 ± 51 |
| 275.0 | 2802 ± 19 |
| 276.0 | 18233 ± 124 |
| 277.0 | 9903 ± 66 |
| 278.0 | 32749 ± 169 |
| 279.0 | 19692 ± 76 |
| 279.9 | 18252 ± 92 |
| 280.9 | 27678 ± 149 |
| 282.0 | 17559 ± 92 |
| 283.0 | 13483 ± 88 |
| 284.0 | 22859 ± 145 |
| 284.9 | 25068 ± 131 |
| 286.0 | 31057 ± 114 |
| 287.9 | 37777 ± 167 |

Table 4.1: Calculated charge for all the experimental runs.

## 4.5 Analysis of $\gamma$ ray spectra

### 4.5.1 High Purity germanium $\gamma$ ray spectra

The interaction of $\gamma$ rays with the bulk material of the detectors is dominated by three main processes: photoelectric effect, Compton scattering and pair production. In each of these processes, the incoming photon produces secondary radiation: electrons in the photoelectric effect, electrons and secondary photons in the Compton scattering, and electron positron pairs in the pair production. The positrons produced after the pair production annihilate with electrons present in the medium, producing a pair of photons emitted in a back to back fashion.

In general, the electrons are absorbed by the detector's material and produce signal, while the secondary photons may be collected entirely or partially. Figure 4.7 shows a diagram of different possible interaction processes.

If the secondary radiation is collected entirely, the energy of the incoming $\gamma$ ray is the same of the signal produced in the detector. At this energy it is present a peak in the spectrum, called full energy peak or photopeak.

On the other hand, when one or more secondary photons escape the detector, different features may be present.

If a secondary photon is emitted after a Compton scattering event (or after multiple Compon scattering events) and exits the detector without interaction, the acquired signal has a lower energy respect to the incoming $\gamma$ ray. Since in Compton scattering the energy transferred to the electron is not fixed, the spectrum shows a continuum at energies lower than the full-energy peak.

In the case of the pair production mechanism, the photons produced in the positron annihilation have energy equal to $m_{electron} \cdot c^2$. If both the annihilation photons are absorbed

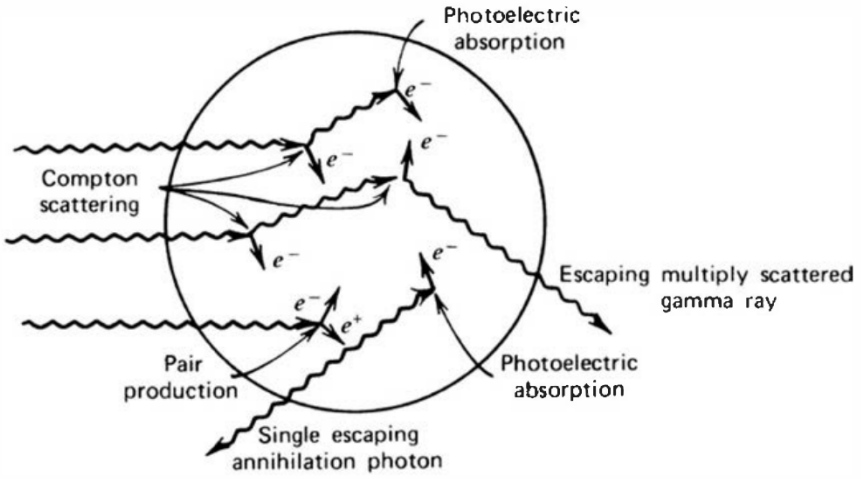


Figure 4.7: Diagram of possible interactions of $\gamma$ rays with the detector. Figure taken from [52].

by the detector, they contribute to the full-energy peak, otherwise they may originate first or second escape peaks. First escape peaks originate when only one of the annihilation photons escape the detector without interaction, and in the energy spectrum they are located at $E_\gamma - m_{electron} \cdot c^2$. Second escape peaks are the consequence of the escape of both annihilation photons, and in the energy spectrum they produce a peak at energy $E_\gamma - 2m_{electron} \cdot c^2$. [52]

The following analysis is mainly focused on the evaluation of the net areas of the full-energy peaks. Nonetheless, it is necessary to take into account the contribution of the Compton continuum and the peaks associated to first and second escape $\gamma$ rays that contribute to the experimental spectra.

### 4.5.2 Energy calibration

The data acquired using the analogue multichannel mode are stored in histograms whose bins are the channels of the MCA. In order to associate the channel number to the energy it is necessary to calibrate the spectra in energy.

The $\gamma$ rays emitted in the de-excitation of the resonant levels cover a wide energy range: from about 1 MeV to 7 MeV. For this reason, in the calibration procedure, known peaks at both high and low energy are used. Three low energy peaks are produced by the decay of the radioactive sources of $^{137}$Cs and $^{60}$Co. Instead, at higher energy it is exploited the resonant reaction induced by the proton beam on $^{19}$F contaminants. In this reaction, $^{16}$O is populated in an excited state and its de-excitation produces a $\gamma$ ray of energy $E_\gamma$ =6130 keV. In addition to the full energy peak, the first and the second escape peaks are also visible. Table 4.2 summarizes the six peaks used in the energy calibration.

The relation between the channel number and the energy is linear, thus the pairs ($N_{ch}$, $E_\gamma$), where $N_{ch}$ is the chamber number and $E_\gamma$ the peak energy, are fitted using the function

$$E_\gamma = m \cdot N_{ch} + q$$

Figure 4.8 shows the linear fit for both detectors and the energy calibration coefficients are reported in Table 4.3. To test the goodness of the fit it is defined the variable $t$, which follows the t-Student statistic at N-2 degrees of freedom:

$$t = \frac{\rho\sqrt{N-2}}{\sqrt{1-\rho^2}} \tag{4.18}$$

where $N$ is the number of data points and $\rho$ is the linear correlation coefficient. From the values obtained, it is possible to affirm that the hypothesis of not linear correlation is false with more than 95% confidence level for both linear fits.

| Decay or Reaction | Energy $\gamma$ [keV] |
|---|---|
| $^{137}$Cs | 661.657 |
| $^{60}$Co | 1173.228 |
| $^{60}$Co | 1332.501 |
| $^{19}$F(p,$\alpha\gamma$)$^{16}$O, full energy peak | 6128.63 |
| $^{19}$F(p,$\alpha\gamma$)$^{16}$O, first escape peak | 5617.63 |
| $^{19}$F(p,$\alpha\gamma$)$^{16}$O, second escape peak | 5106.63 |

Table 4.2: $\gamma$ rays used in the energy calibration of the detectors.

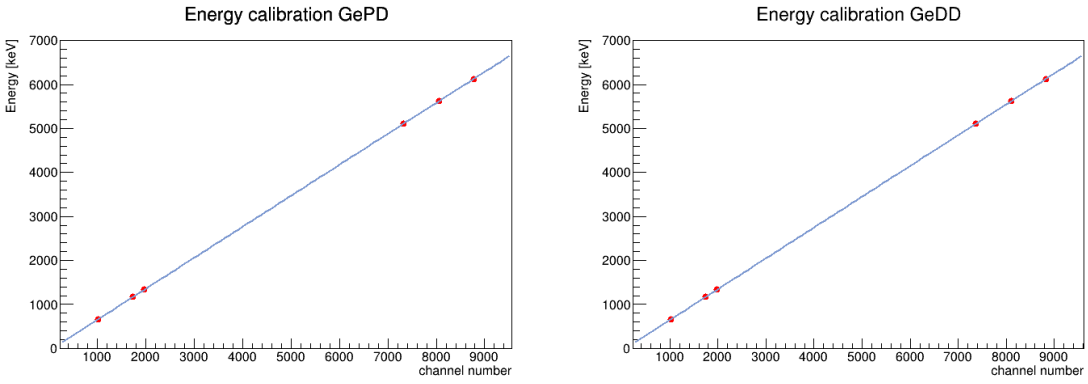


Figure 4.8: Linear fit for the energy calibration of the GePD detector (left panel) and the GeDD detector (right panel). The error bars are not visible because smaller than the points.

| Detector | Calibration slope $m$ [keV/channels] | Calibration offset $q$ [keV] | $\rho$ |
|---|---|---|---|
| GePD | 0.704156 $\pm$ 0.000008 | -49.57 $\pm$ 0.01 | 0.99999998 |
| GeDD | 0.700115 $\pm$ 0.00001 | -50.88 $\pm$ 0.01 | 0.999999996 |

Table 4.3: Coefficients of the energy calibration for both GePD and GeDD detectors. $\rho$ is the linear correlation coefficient.

### 4.5.3 Peak identification in the experimental spectra

Once performed the energy calibration, it is possible to identify the different $\gamma$ lines present in the experimental spectra. In particular, it is possible to identify the features described in 4.5.1: full-energy peaks, first and second escape peaks and Compton continuum.

The first step in the peaks identification is the distinction of the signal produced by the reaction of interest from the background. Several reactions are frequently observed [20, 8]:

- $^{21}$Ne(p,$\gamma$)$^{22}$Na: the reaction of interest produces $^{22}$Na, which is unstable and decays $\beta^+$ to an excited level of $^{22}$Ne. The excited level of $^{22}$Ne de-excites emitting a $\gamma$ ray of

energy $E_\gamma = 1275$ keV. As a consequence of the positron emitted in the $\beta^+$ decay, $\gamma$ rays at $E_\gamma = 511$ keV are also produced.

- $^{14}$N(p,$\gamma$)$^{15}$O: this reaction has a $Q_{value} = 7297$ keV and a resonance at $E_p = 278$ keV that populates the 7556.5 keV excited level of $^{15}$O. In the decay cascade of the 7556.5 keV level, $\gamma$ rays are emitted at the following energies: 7554.5, 6791.4, 6174.9, 5239.9, 5182, 2373, 1618.4, 1380.1, 763.4, 697.1 keV. The origin of nitrogen contaminants may be associated to implantation during tests with nitrogen gas.
- $^{19}$F(p,$\alpha\gamma$)$^{16}$O: this reaction has a $Q_{value} = 8114$ keV and has a rather high cross section at energies close to its $E_p = 223$ and 340 keV resonances. $^{16}$O is populated in an excited state and its de-excitation produces a $\gamma$ ray of energy $E_\gamma$=6128.63 keV. In addition to the full energy peak, the first and the second escape peaks are visible. Fluorine contaminants are associated to the heat conductive paste used in the calorimeter of a precedent experiment and to the O-rings used in the gas target set up.

The $\gamma$ ray peaks due to beam induced background visible in a typical spectrum acquired with the GePD detector at $E_p = 287.9$ keV are shown in Figure 4.9 (zoom on the lower energy part of the spectrum) and 4.10 (zoom on the higher energy part of the spectrum). In addition, when visible, the first escape ($FE$) and second escape ($SE$) peaks are also displayed.

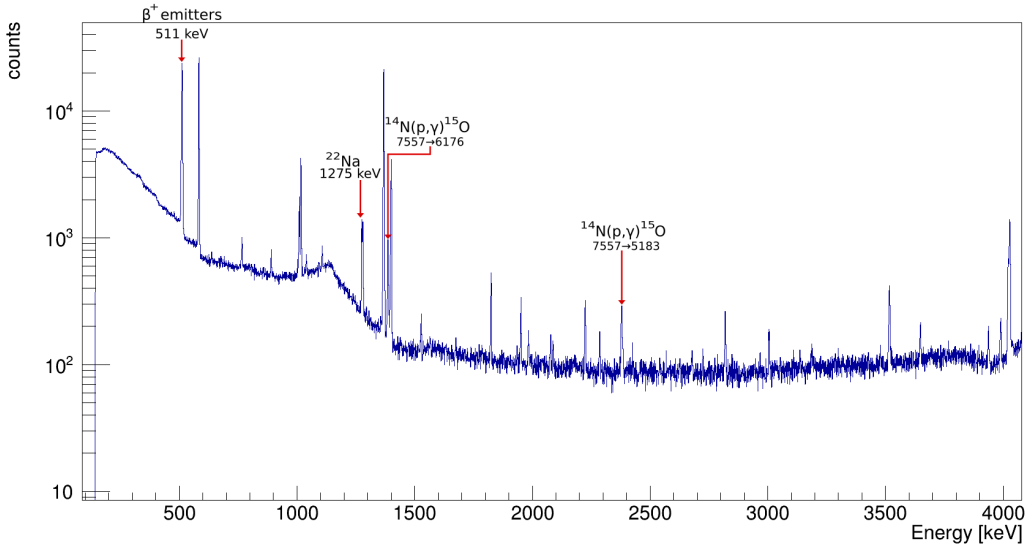


Figure 4.9: Spectrum acquired with GePD detector at $E_p$=282.0 keV, zoom on the 0 keV - 4000 keV energy region. $\gamma$ rays produced by beam induced background are marked.

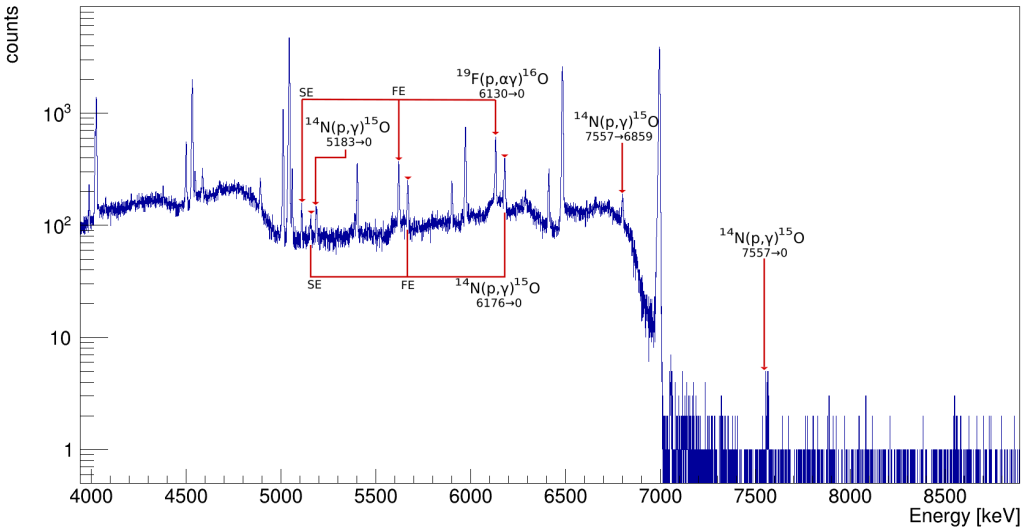


Figure 4.10: Spectrum acquired with GePD detector at $E_p$=282.0 keV, zoom on the 4000 keV - 8500 keV energy region. $\gamma$ rays produced by beam induced background are marked.

After the identification of the background contribution, it is possible to identify the peaks produced by the reaction of interest. In Section 2.2, Figure 2.5 and 2.6 show the primary $\gamma$ transitions expected from the de-excitation of the resonant states populated by the $E_p$=271 keV and $E_p$=272 keV resonances. In addition to these primary transitions, several other $\gamma$ lines, not attributable to background or secondary $\gamma$ rays, were observed during the analysis. Taking into account the excited levels of $^{22}$Na, four new primary transitions contribute in the de-excitation of the level populated by the $E_p$=272 keV resonance. Figure 4.11 shows the decay scheme of the 6998.1 keV level including both the transitions from literature and the new ones observed at LUNA. In addition, the associated secondary $\gamma$ cascade is also displayed.

To check whether these transitions are correctly identified, it is ongoing a detailed study of the coincidences between the primary $\gamma$ rays and the associated secondaries on the two detectors.

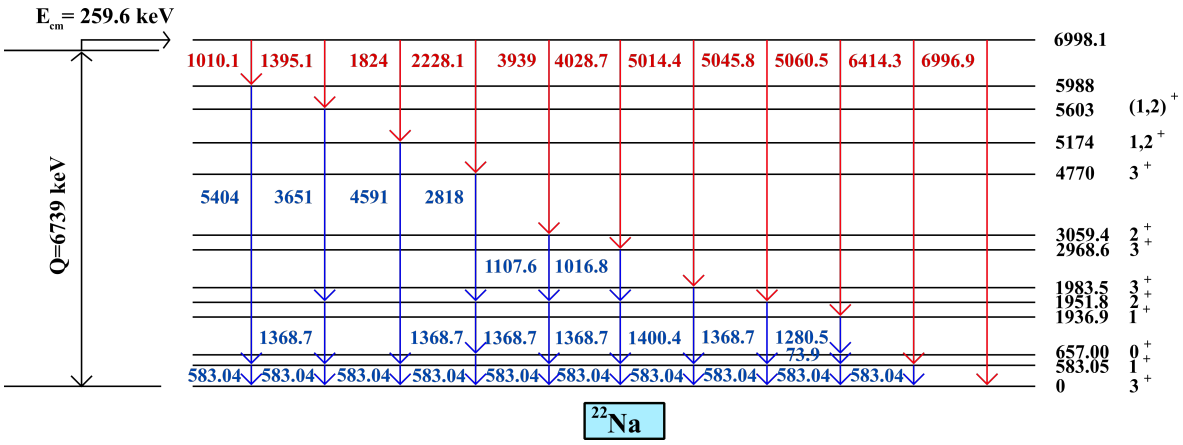


Figure 4.11: Level scheme of the transitions observed in the experimental spectra for the $E_p$=272 keV resonance, including both transitions from literature and the new ones observed at LUNA. All the energy levels and the transitions are in units of keV. The red arrows refer to primary $\gamma$ rays, while the blue arrows to secondary $\gamma$ rays. Data taken from [32].

Figure 4.12, 4.13 and 4.14 show the zoom on different energy regions of a typical experimental spectrum, acquired using the GePD detector and with beam energy $E_p$=282.0 keV (resonance populated in front of the detector). In Figure 4.12, 4.13 and 4.14 all the primary transitions and the visible first and second escape peaks are marked.

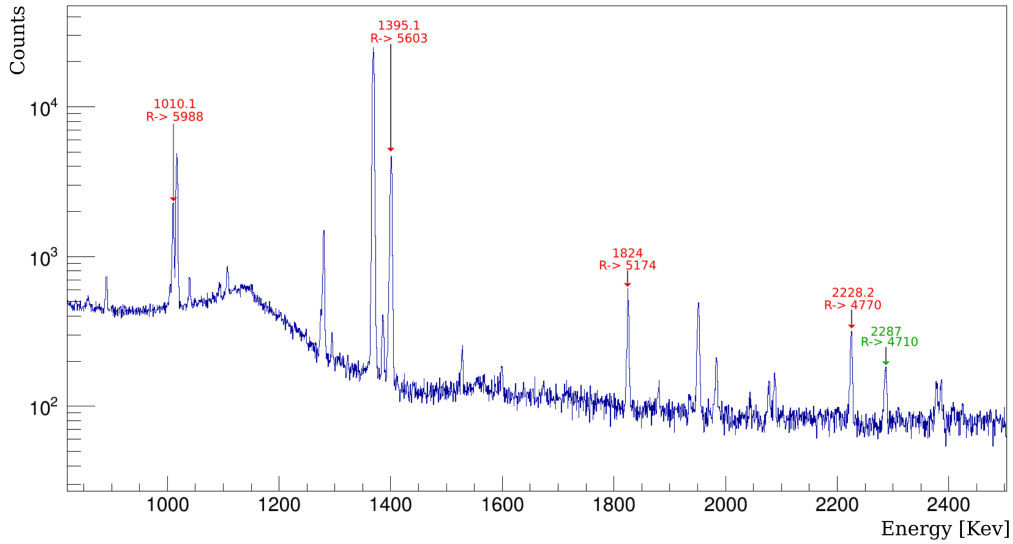


Figure 4.12: Spectrum acquired with GePD detector at $E_p$=282.0 keV, zoom on the 600 keV - 2600 keV energy region. The primary $\gamma$ rays produced by the $E_p$=271 keV resonance are marked in green, the primary $\gamma$ rays produced by the $E_p$=272 keV resonance are marked in red.

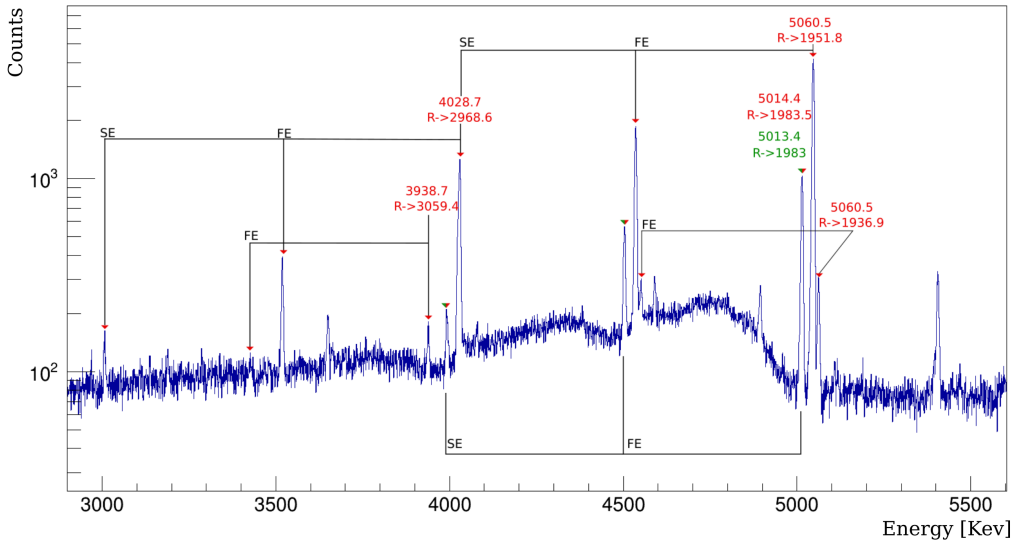


Figure 4.13: Spectrum acquired with GePD detector at $E_p$=282.0 keV. Zoom on the 3000 keV - 5500 keV energy region. The primary $\gamma$ rays produced by the $E_p$=271 keV resonance are marked in green, the primary $\gamma$ rays produced by the $E_p$=272 keV resonance are marked in red.

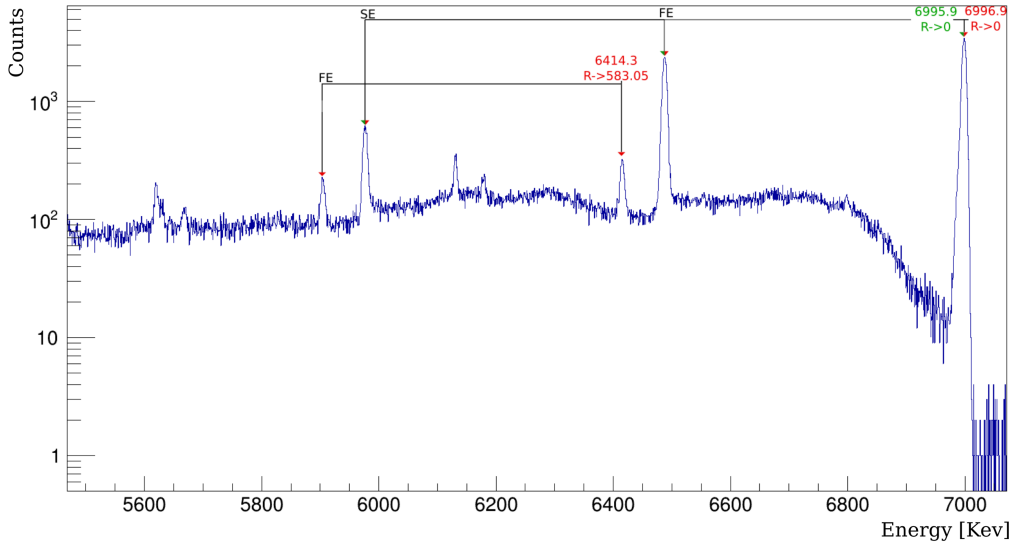


Figure 4.14: Spectrum acquired with GePD detector at $E_p$=282.0 keV. Zoom on the 5600 keV - 7000 keV energy region. The primary $\gamma$ rays produced by the $E_p$=271 keV resonance are marked in green, the primary $\gamma$ rays produced by the $E_p$=272 keV resonance are marked in red.

## 4.6 Efficiency

In the following analysis it is necessary to introduce the *full energy peak efficiency*, defined as the ratio of the number of counts detected in the full energy peak of a $\gamma$ ray of energy $E_\gamma$ to the number of emitted $\gamma$ rays of that energy [42]. The efficiency is a function of both the $\gamma$ ray energy and the solid angle of the detector. In the $^{21}$Ne(p,$\gamma$)$^{22}$Na reaction study, the efficiency must be known for a wide range of energies, since $\gamma$ rays of energies from few hundreds of keV up to almost 7 MeV are emitted. In addition, the efficiency must be measured at different distances from the detectors, since in the gas target the resonance is populated in different positions in the chamber depending on the proton beam energy.

As already mentioned, the experimental setup used for the $^{20}$Ne(p,$\gamma$)$^{21}$Na and the $^{21}$Ne(p,$\gamma$)$^{22}$Na reaction studies is the same. During the $^{20}$Ne(p,$\gamma$)$^{21}$Na reaction measurement, the efficiency has already been studied and, since the setup was not dismounted between the two measurements, the efficiencies are expected to be unchanged. Nonetheless, to verify that the efficiency did not change over time, the low energy component was re-measured at the beginning of the $^{21}$Ne(p,$\gamma$)$^{22}$Na reaction data acquisition.

Indeed, the experimental measurement of the efficiency is divided in two steps: firstly it is measured the low energy component and then it is extended to higher energies. The same procedure has been used for both the GePD and the GeDD detectors. The efficiency at low energies is measured using point-like calibrated sources of $^{60}$Co, $^{137}$Cs and $^{133}$Ba, which decay emitting $\gamma$ rays of fixed energies up to 1333 keV. The sources are mounted on a source holder that keeps the sources at the height of the beam axis and allow to move them along the beam axis. In this configuration, the full energy peak efficiency for a $\gamma$ ray of energy $E_\gamma$ is obtained as

$$\eta(E_\gamma) = \frac{N_\gamma}{A(t)\Delta t BR} \tag{4.19}$$

where $N_\gamma$ are the net counts of the full energy peak, $A(t)$ is the source activity at the measurement time, $\Delta t$ is the measurement time and $BR$ is the branching ratio of the observed $\gamma$ ray. The efficiency as a function of the distance from the AP1 collimator is obtained with

several acquisitions in which the sources are moved inside the target chamber in steps of $\sim 0.5 - 1$ cm. The positions in the chamber corresponding to the maximum efficiency are in front of the detectors, and in these positions the efficiency curve (efficiency as a function of the energy) is obtained fitting the experimental efficiencies with the function

$$\eta(E_\gamma) = e^{a+b\log E_\gamma + c\log^2 E_\gamma} \tag{4.20}$$

where $a$, $b$ and $c$ are the coefficients obtained from the fit.

The efficiency curve is then extended to higher energies using the $E_p = 278$ keV resonance of the $^{14}$N(p,$\gamma$)$^{15}$O reaction. This resonance populates the $E_x = 7556.5$ keV state of $^{15}$O, which de-excites emitting primary $\gamma$ rays at $E_\gamma = 765$ and 1384 keV. Associated to these primary $\gamma$ rays there are always (branching ratio 100%) two high energy secondary $\gamma$ rays at $E_\gamma = 6790$ and 6171 keV. The efficiency at high energy $\eta(E_{\gamma,high})$ is obtained from the efficiency at low energy $\eta(E_{\gamma,low})$ as

$$\eta(E_{\gamma,high}) = \eta(E_{\gamma,low})\frac{N_{\gamma,high}}{N_{\gamma,low}} \tag{4.21}$$

where $N_{\gamma,high}$ and $N_{\gamma,low}$ are the net counts of the secondary and primary $\gamma$ ray peaks respectively, obtained for high statistic runs acquired at the beam energy corresponding to the maximum yield. The low energy efficiency $\eta(E_{\gamma,low})$ is calculated from eq. 4.20 using the fit coefficients obtained with the radioactive sources.

At this point, all the experimental efficiencies, both the low energy component from the sources and the high energy one from eq. 4.21, are fitted with the function in eq. 4.20, and it is obtained a new efficiency curve that extends to higher energies.

The low energy efficiency component measured during the $^{21}$Ne(p,$\gamma$)$^{22}$Na reaction campaign is in agreement with the one measured previously. Thus, it was decided not to proceed with the re-measurement of the high energy component and the efficiency curves used in the $^{21}$Ne(p,$\gamma$)$^{22}$Na data analysis are the ones already obtained during the $^{20}$Ne(p,$\gamma$)$^{21}$Na reaction measurement. More details on the efficiency measurement can be found in [8, 53].

Finally, it is important to report that the experimental efficiencies have been corrected for summing effects before each fitting procedure. These are underestimations of the number of net counts that take place when two (or more) $\gamma$ rays are emitted in a time interval shorter than the time resolution of the detector. In this case, the signal of the two (or more) $\gamma$ rays is summed, resulting in a loss of counts in the full energy peak.

## 4.7 Peak areas

A fundamental quantity in the analysis is the net area of the full energy peaks of primary $\gamma$ transitions. Indeed, it is necessary to calculate the yield values, which are used in both the resonance energy and the resonance strength determination. The net area is obtained considering the number of counts under the peak and subtracting the background contribution, which is mainly due to Compton continuum from other peaks. The net area coincides with the net number of counts of the peaks.

To perform this part of the analysis, each peak is considered individually, because nearby peaks or other structures in the spectrum may affect the net area and the background. What is more, another issue arises when two primary $\gamma$ rays are very close in energy and cannot be resolved separately by the detectors. In the two following Sections, there is the description of the methods used for the net area evaluation of each primary peak. As in 4.5.3, it is used, as an example, a typical spectrum acquired using the GePD detector at beam energy $E_p$=282 keV.

The net areas of the 2287 keV and 5045.8 keV transitions are calculated for all the runs, and the results are reported in Table 4.5. Instead, the net areas of the other primary $\gamma$ rays

are calculated only for the runs acquired at the energy corresponding to the maximum of the yield curve (see 4.8). The results obtained for the runs acquired at $E_p$=282.0 keV with the GePD detector and at $E_p$=278.0 keV with GeDD detector are reported in Table 4.6 and 4.7 for the primary transitions of the $E_p$=271 keV and $E_p$=272 keV resonances respectively.

### 4.7.1 Net area of primary $\gamma$ transitions of $E_p$=271 keV resonance

#### 2287 keV peak

The 2287 keV peak is an isolated peak and the background contribution to the total area can be evaluated considering its average value in the regions on the left and on the right of the peak. To perform this operation, it is used the *jRadView* software [54]. Figure 4.15 shows the operating window of *jRadView*. The magenta markers allow to select the region of interest of the peak (ROI). In this region, after calculating the total number of counts, the software subtracts the background contribution and returns the net area of the peak. It is possible to select the energy region in which the background is evaluated (green markers). If there are no other peaks in the vicinity of the one of interest, the background is evaluated in two regions immediately adjacent to the ROI and as broad as the ROI. The background contribution to the peak is visualized as a green horizontal line. Together with the net area values, the software provides also the associated statistical errors, propagated as reported in [42].

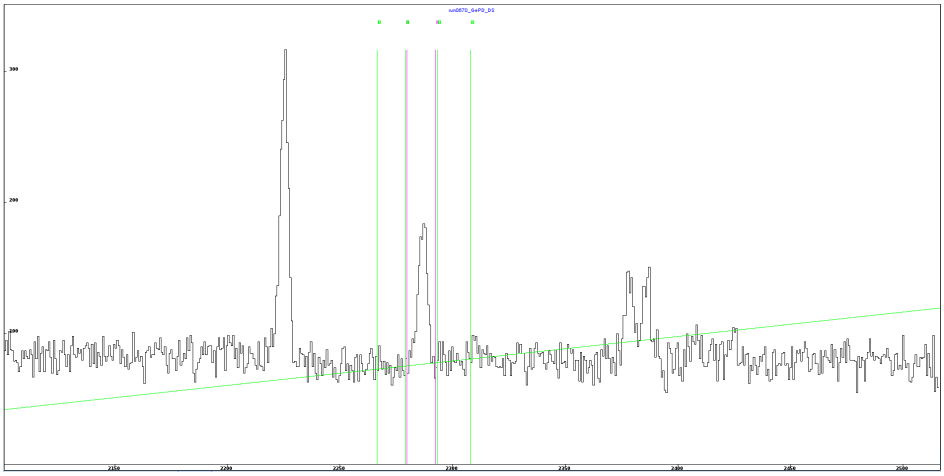

Figure 4.15: Zoom on the 2287 keV peak energy region. Spectrum acquired with the GePD detector at $E_p$=282.0 keV, visualized in the *jRadView* software operating window.

#### 5013.4 keV peak

The 5013.4 keV peak is very close in energy to the 5014.4 keV peak, which is one of the possible decay modes of the resonant state populated by the $E_p$=272 keV resonance. As a result, the two $\gamma$ rays are not resolved separately and both contribute to a common peak. The procedure to evaluate the area exploits the branching ratio values for the decay of the 6997.1 keV excited state of $^{22}$Na tabulated in [32]. The branching ratios of the excited level populated by the $E_p$ = 271 keV resonance are taken from literature and not calculated because not all the primary transitions are observed. To limit the systematic contributions, it was decided to use only the decay branching ratio values of the 6997.1 keV excited level of $^{22}$Na (populated by the resonance at $E_p$=271 keV) and not the ones of the 6998.1 keV excited level (populated by the resonance at $E_p$=272 keV).

As in the case of an isolated peak, it is firstly calculated the net area of the common peak using *jRadView*. Figure 4.16 shows the evaluation of the area of the 5013.4 keV and 5014.4 keV common peak.

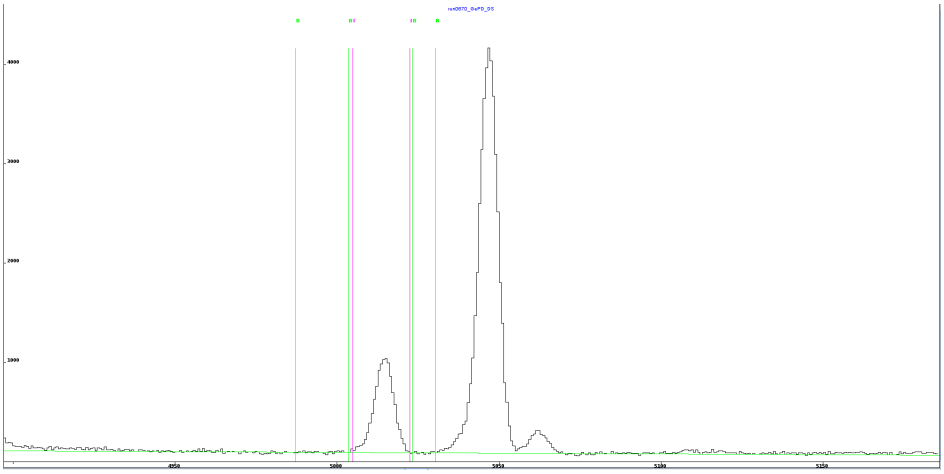

Figure 4.16: Zoom on the 5013.4 keV and 5014.4 keV common peak energy region. Spectrum acquired with the GePD detector at $E_p$=282.0 keV, visualized in the *jRadView* software operating window.

To disentangle the two contributions, the number of net counts expected for the 5013.4 keV $\gamma$ ray is given by

$$N_{5013.4} = \eta_{5013.4} \cdot BR_{5013.4} \cdot N_{reactions} \tag{4.22}$$

where $\eta_{5013.4}$ is the efficiency for $E_\gamma$=5013.4 keV and $BR_{5013.5} = (0.49 \pm 0.02)$ is the branching ratio for the 5013.4 keV primary transition. $N_{reactions}$ is the number of reactions that populate the $E_p$=271 keV resonant state and it is obtained as

$$N_{reactions} = \frac{N_{2287}}{\eta_{2287} \cdot BR_{2287}} \tag{4.23}$$

where $N_{2287}$ are the number of net counts for the 2287 keV peak, $\eta_{2287}$ is the efficiency for $E_\gamma$=2287 keV and $BR_{2287} = (0.16 \pm 0.02)$ is the branching ratio for the 2287 keV primary transition. The error associated to $N_{5013.4}$ is obtained through propagation of the uncertainties on the efficiency, the branching ratio and the number of counts.

### 5468.7 keV peak

The 5468.7 keV peak is visible in none of the experimental spectra. Thus, no values for its area are measured in the Autumn 2022 campaign.

### 6995.9 keV peak

The 6995.9 keV peak is very close to the 6996.9 keV peak, which is one of the possible decay modes of the resonant state populated by the $E_p$=272 keV resonance. As a result, the two $\gamma$ rays are not resolved separately and both contribute to a common peak. The procedure to evaluate the area is the same adopted for the 5013.4 keV peak.

Figure 4.17 shows the evaluation of the area of the 6995.9 keV and 6996.9 keV common peak with *jRadView*.

To disentangle the two contributions, the number of net counts expected for the 6995.9 keV is given by

$$N_{6995.9} = \eta_{6995.9} \cdot BR_{6995.9} \cdot N_{reactions} \tag{4.24}$$

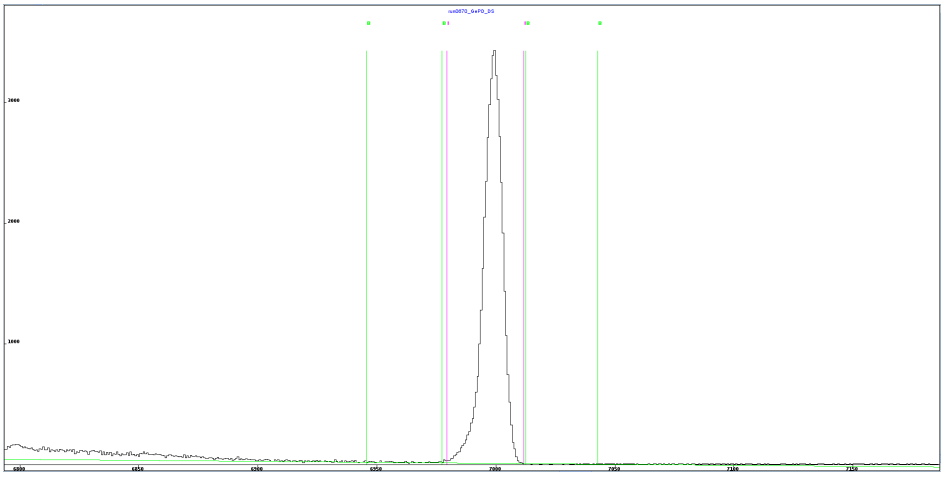

Figure 4.17: Zoom on the 6995.9 keV and 6996.9 keV common peak energy region. Spectrum acquired with the GePD detector at $E_p$=282.0 keV, visualized in the *jRadView* software operating window.

where $\eta_{6995.9}$ is the efficiency for $E_\gamma$=6995.9 keV and $BR_{6995.9} = (0.30 \pm 0.02)$ is the branching ratio for the 5013.4 keV primary transition and $N_{reactions}$ is the number of reactions that populate the $E_p$=271 keV resonant state.

### 4.7.2 Net area of primary $\gamma$ transitions of $E_p$=272 keV resonance

#### 1010.1 keV peak

The 1010.1 keV peak is close to a secondary $\gamma$ ray of $E_\gamma$=1016.3 keV belonging to the decay cascade of the 6998.1 keV level populated by the $E_p$=272 keV resonance (see Figure 2.6). In this case the two peaks are distinguishable, but still not separated enough to be analyzed separately. Thus, the net area is evaluated fitting the two peaks with a function comprising the sum of two Gaussian functions and a polynomial of first grade, that takes into account the background contribution. Since the Gaussian functions are normalized, the net area of the peaks is given by the constant coefficient. Figure 4.18 shows the two peaks fitted with the aforementioned function.

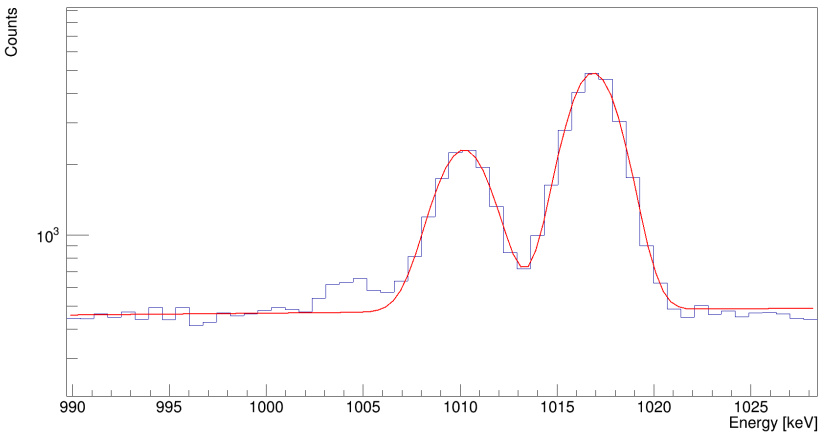


Figure 4.18: Fit of the 1010.1 keV and 1016.3 keV peaks with two normalized Gaussian functions and a polynomial of first degree. Spectrum acquired with the GePD detector at $E_p$=282.0 keV.

### 1395.1 keV peak

The 1395.1 keV peak is close to a secondary $\gamma$ ray of $E_\gamma$=1400 keV. This $\gamma$ ray is produced in the decay cascade of both the 6997.1 keV and the 6998.1 keV excited levels (see Figure 2.5 and 2.6). In this case the two peaks are not resolved separately and the net area is obtained subtracting the contribution of the secondary $\gamma$ rays.

Figure 4.19 shows the evaluation of the area of the 1395.1 keV and 1400 keV common peak with *jRadView*.

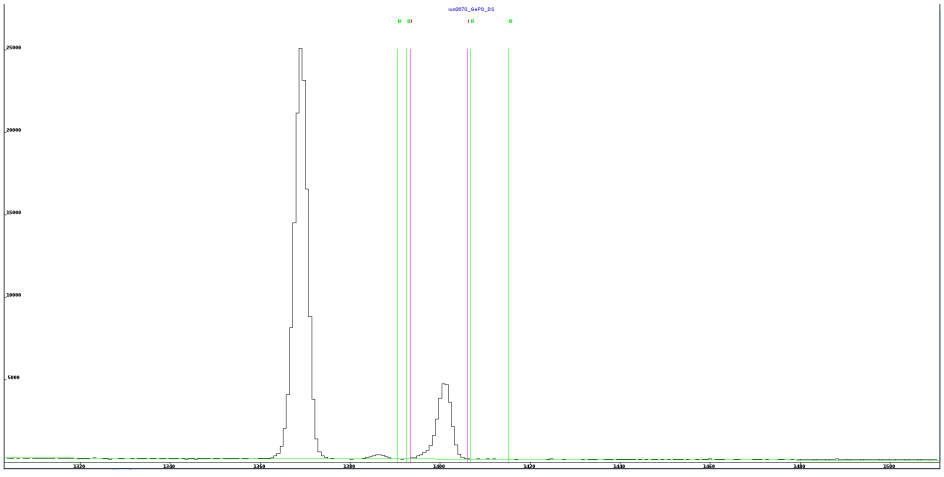

Figure 4.19: Zoom on the 1395.1 keV and 1400.4 keV common peak energy region. Spectrum acquired with the GePD detector at $E_p$=282.0 keV, visualized in the *jRadView* software operating window.

The contribution from the $E_p$=271 keV resonance to the 1400.4 keV peak is evaluated using the branching ratios:

$$N_{1400.4} = \eta_{1400.4} \cdot BR_{1400.4} \cdot N_{reactions} \tag{4.25}$$

where $\eta_{1400.4}$ is the efficiency for $E_\gamma$=1400.4 keV and $BR_{1400.4} = (0.61 \pm 0.02)$ is the branching ratio for the 1400.4 keV secondary transition and $N_{reactions}$ is the number of reactions that populate the $E_p$=271 keV resonant state. In this case the branching ratio is obtained summing the probability of the different paths that may produce a 1400.4 keV $\gamma$ ray.

Instead, the contribution from the $E_p$=272 keV resonance is obtained from the number of net counts of the 5014.4 keV peak as:

$$N_{1400.4} = \frac{N_{5014.4}}{\eta_{5014.4}} \cdot BR_{1400.4} \cdot \eta_{1400.4} \tag{4.26}$$

where $\eta_{1400.4}$ and $\eta_{5014.4}$ are the efficiencies for $E_\gamma$=1400.4 keV and $E_\gamma$=5014.4 keV respectively, $BR_{1400.4} = (0.969 \pm 0.003)$ is the branching ratio for the 1400.4 keV secondary transition and $N_{5014.4}$ are the net counts of the 5014.4 keV peak.

### 1824 keV peak

The 1824 keV peak is an isolated peak and the net area is calculated with the same procedure described for the 2287 keV peak. Figure 4.20 shows the evaluation of the area using *jRadView*.

### 2228.1 keV peak

The 2228.1 keV peak is an isolated peak and the net area is calculated with the same procedure described for the 2287 keV peak. Figure 4.21 shows the evaluation of the area using *jRadView*.

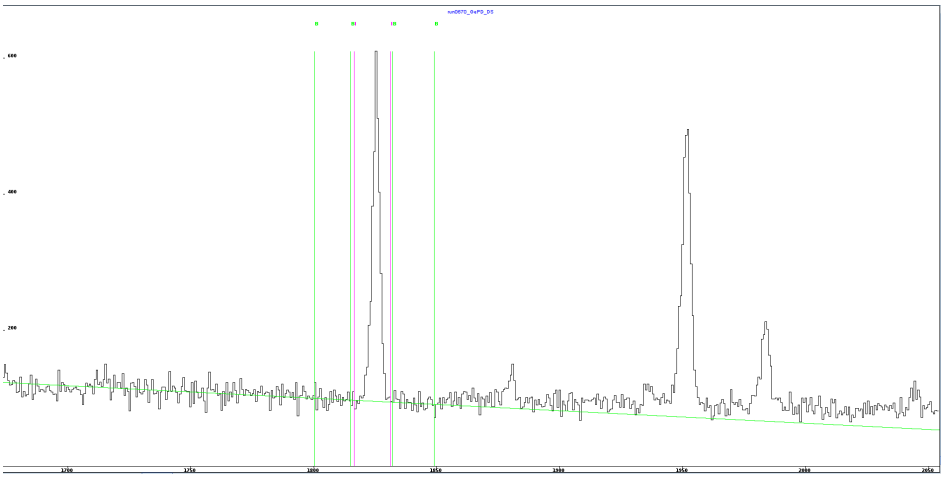

Figure 4.20: Zoom on the 1824 keV peak energy region. Spectrum acquired with the GePD detector at $E_p$=282.0 keV, visualized in the *jRadView* software operating window.

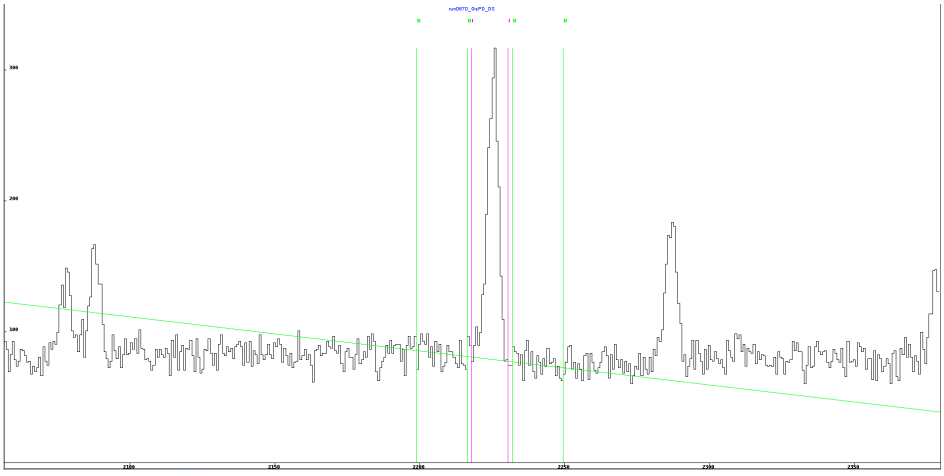

Figure 4.21: Zoom on the 2228.1 keV peak energy region. Spectrum acquired with the GePD detector at $E_p$=282.0 keV, visualized in the *jRadView* software operating window.

### 3938.7 keV peak

The 3938.7 keV peak is an isolated peak and the net area is calculated with the same procedure adopted for the 2287 keV peak. Figure 4.22 shows the evaluation of the area using *jRadView*.

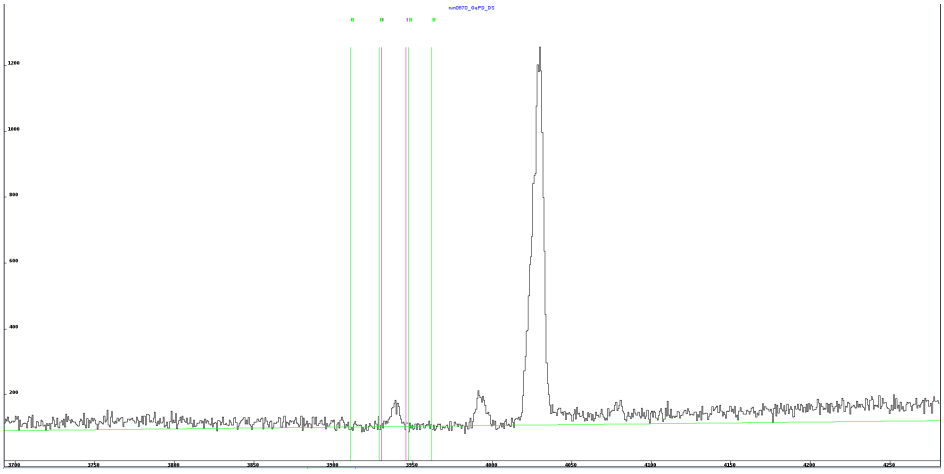

Figure 4.22: Zoom on the 3938.7 keV peak energy region. Spectrum acquired with the GePD detector at $E_p$=282.0 keV, visualized in the *jRadView* software operating window.

### 4028.7 keV peak

The 4028.7 keV peak is very close to the second escape peak ($E_\gamma$=4023.8 keV) of another primary $\gamma$ ray of $E_\gamma$=5045.8 keV, that may be produced by the decay of the 6998.1 keV excited level of $^{22}$Na when the $E_p$=272 keV resonance is populated. The two peaks are not resolved and contribute to a common peak in the spectrum. To disentangle the two areas it is used a procedure similar to the one adopted for the 5013.4 keV peak. The main difference is that no transitions from the 271 keV are involved and one of the two $\gamma$ rays is a second escape peak. The contribution of the 4023.8 keV $\gamma$ ray is calculated using the results obtained simulating the experiment with the Monte Carlo method. In the simulations the two peaks are resolved independently. In addition, it is possible to select which transitions are visualized in the spectra. The spectra are simulated at energies of $E_p$ = 280.91 keV for the GePD detector and $E_p$=278.04 keV for the GeDD one. The 4028.7 keV peak is not visualized in the histograms. The percentage of second escape counts respect to the full energy counts is obtained as $N_{4023.8}/N_{5045.8}$, where $N_{5045.8}$ and $N_{4023.8}$ are the net areas of the full energy peak and the second escape in the simulated spectrum. Figure 4.23 shows a zoom on the energy region of the 5045.8 keV full energy peak in the simulated spectrum and Figure 4.24 shows a zoom on the second escape peak.

The net area of the peaks in the simulated spectra is obtained as the difference of the total counts under the ROI of the peak and the background contribution. The latter is evaluated in regions on the left and on the right of the ROI of the peak (as visible in Figure 4.23 and 4.24). The results obtained from the simulations are reported in Table 4.4.

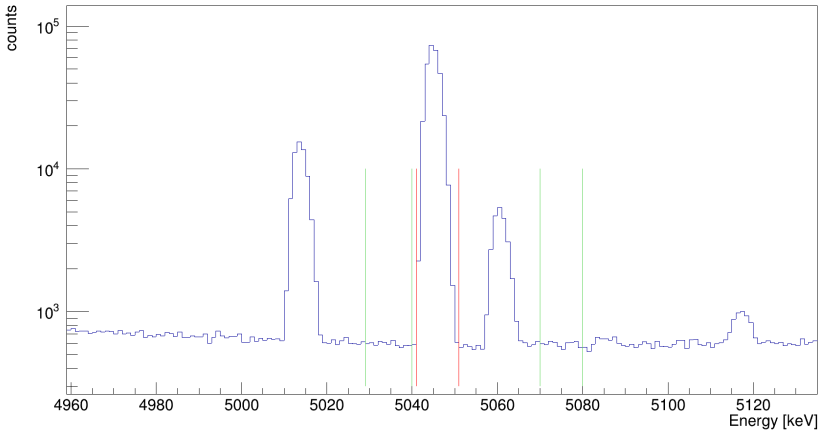


Figure 4.23: Zoom on the 5045.8 keV peak energy region. Simulated spectrum for the GePD detector, $E_p$=280.91 keV. The red markers indicate the ROI for the peak and the green markers the region considered for the background evaluation.

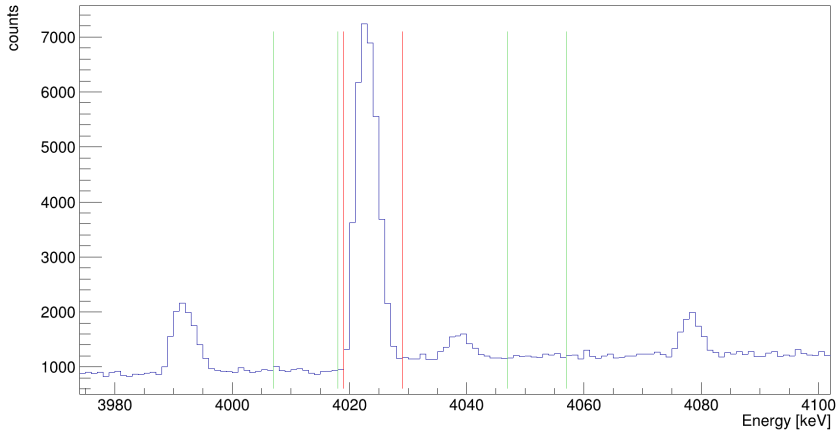


Figure 4.24: Zoom on the second escape peak (4023.8 keV) peak energy region. Simulated spectrum for the GePD detector, $E_p$=280.91 keV. The red markers indicate the ROI for the peak and the green markers the region considered for the background evaluation.

| Detector | $N_{4023.8}/N_{5045.8}$ |
|---|---|
| **GePD** | (9.90±0.08) % |
| **GeDD** | (16.0±0.1) % |

Table 4.4: Percentage of $N_{4023.8}/N_{5045.8}$ obtained from the simulated spectra. The errors on the percentage are obtained propagating the errors on the number of counts.

Once $N_{4023.8}/N_{5045.8}$ is obtained from the simulations, it is possible to determine the expected counts for the 4023.8 keV peak in the experimental spectra. Firstly, it is calculated the area of the full energy peak at 5045.8 keV using *jRadView* (shown in Figure 4.26). Then the number of counts for the second escape peak is obtained by the multiplication of the experimental value of $N_{5045.8}$ and the percentage reported in Table 4.4. The error on the number of counts is associated through propagation.

The common peak is isolated, as it is displayed in Figure 4.25, and its area is obtained using the *jRadView* software. Eventually, the number of counts of the 4028.7 keV peak is obtained subtracting the area of the second escape to the common peak.

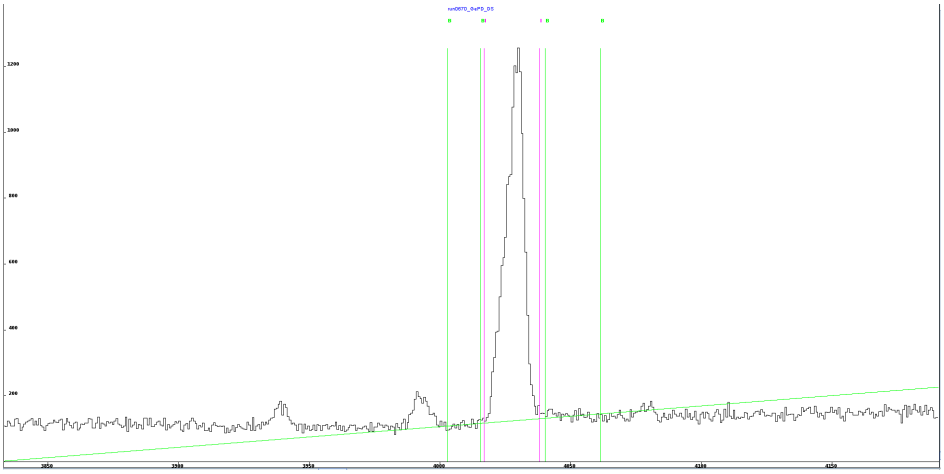

Figure 4.25: Zoom on the 4028.7 keV peak energy region. Spectrum acquired with the GePD detector at $E_p$=282.0 keV, visualized in the *jRadView* software operating window.

### 5014.4 keV peak

As mentioned above, the 5014.4 keV peak is separate by only 1 keV from the 5013.4 keV peak, thus they both contribute to the same common peak. The process to calculate the number of net counts for the 5013.4 keV peak is divided into two steps. Firstly, it is evaluated the net area of the common peak (shown in Figure 4.16) using *jRadView*. Secondly, the net counts obtained for the 5013.4 keV peak are subtracted to the those of the common peak.

### 5045.8 keV peak

The 5045.8 keV peak is close to the 5014.1 keV and the 5060.5 keV peaks, but they are considered separated. Particular attention is dedicated to the region on which the background contribution is evaluated. Figure 4.26 shows the evaluation of the area using *jRadView* and the area selected for the background evaluation.

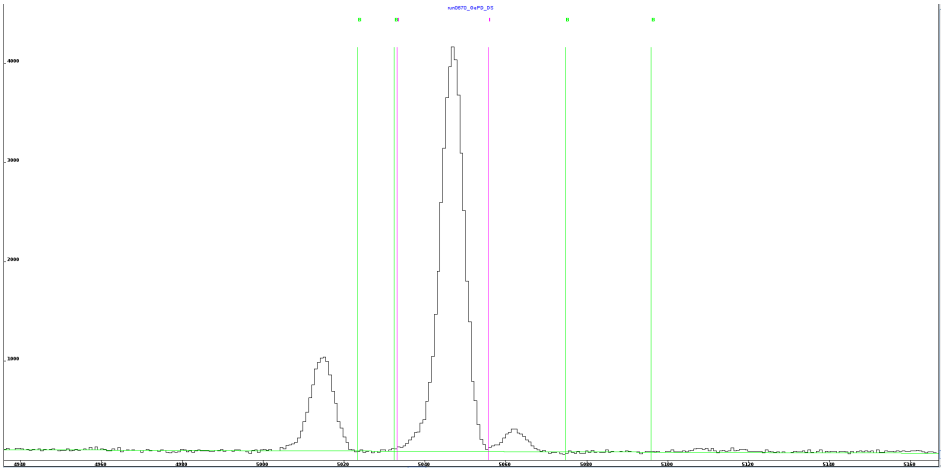

Figure 4.26: Zoom on the 5045.8 keV peak energy region. Spectrum acquired with the GePD detector at $E_p$=282.0 keV, visualized in the *jRadView* software operating window.

### 5060.5 keV peak

As mentioned above, the 5060.5 keV peak is close to the 5014.1 keV and the 5045.8 keV peaks, but they are considered separated. Figure 4.27 shows the evaluation of the area using *jRadView* and the area selected for the background evaluation.

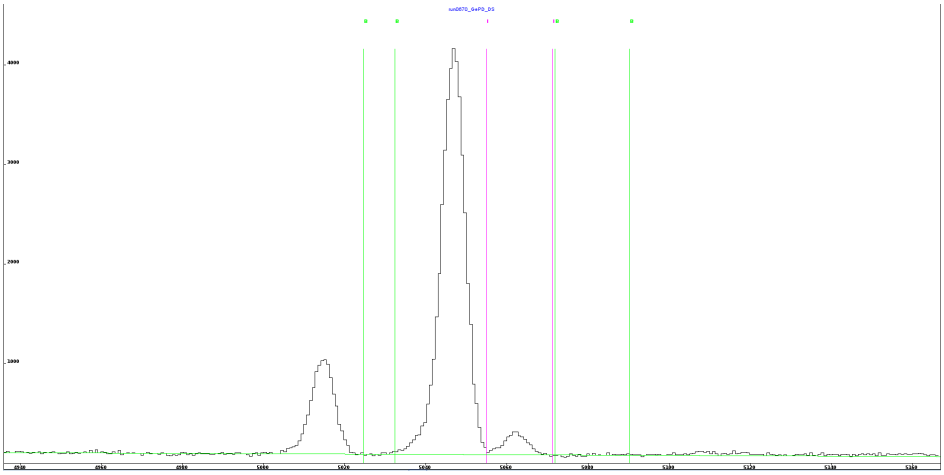

Figure 4.27: Zoom on the 5060.5 keV peak energy region. Spectrum acquired with the GePD detector at $E_p$=282.0 keV, visualized in the *jRadView* software operating window.

### 6414.3 keV peak

The 6414.3 keV peak is an isolated peak and the net area is calculated with the same procedure described for the 2287 keV peak. Figure 4.28 shows the evaluation of the area using *jRadView*.

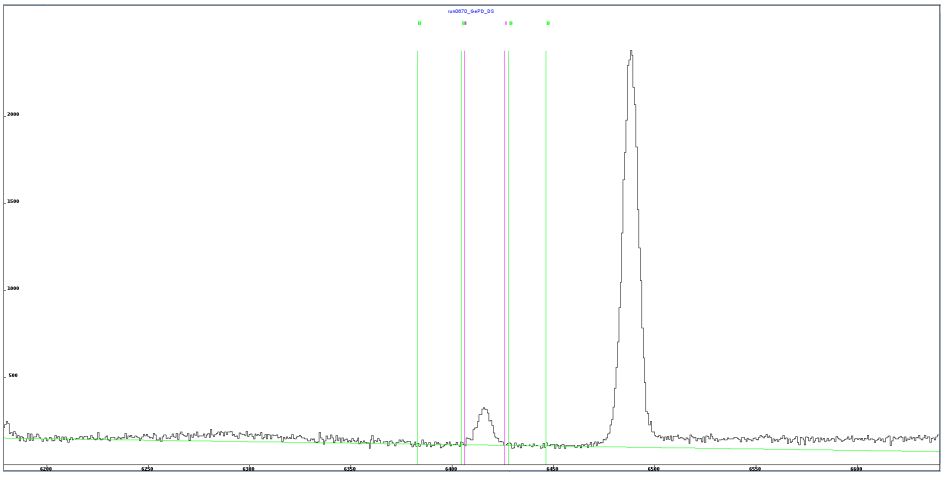

Figure 4.28: Zoom on the 6414.3 keV peak energy region. Spectrum acquired with the GePD detector at $E_p$=282.0 keV, visualized in the *jRadView* software operating window.

### 6996.9 keV peak

The 6996.9 keV peak is separated by only 1 keV from the 6995.9 keV peak, and both $\gamma$ rays contribute to the same peak. The process to calculate the number of net counts is the same as the one described for the 5014.4 keV peak. The common peak is shown in Figure 4.17.

| | **GePD detector** | | **GeDD detector** | |
|---|---|---|---|---|
| $E_p$ [keV] | $N_{2287}$ | $N_{5045.8}$ | $N_{2287}$ | $N_{5045.8}$ |
| 273.0 | 34 ± 13 | 970 ± 33 | | 1489 ± 43 |
| 274.1 | 266 ± 35 | 9728 ± 105 | 378 ± 45 | 12317 ± 128 |
| 275.0 | | 4123 ± 67 | 107 ± 20 | 4865 ± 79 |
| 276.0 | 688 ± 57 | 33263 ± 197 | 826 ± 69 | 37894 ± 223 |
| 277.0 | 398 ± 45 | 21930 ± 158 | 452 ± 51 | 22241 ± 169 |
| 278.0 | 1796 ± 86 | 86659 ± 314 | 1406 ± 89 | 74396 ± 304 |
| 279.0 | 1170 ± 71 | 59889 ± 262 | 657 ± 68 | 41498 ± 229 |
| 279.9 | 1073 ± 70 | 62028 ± 265 | 645 ± 66 | 35767 ± 212 |
| 280.9 | 1841 ± 93 | 99974 ± 339 | 854 ± 85 | 47768 ± 251 |
| 282.0 | 1158 ± 71 | 65224 ± 271 | 270 ± 63 | 24820 ± 176 |
| 283.0 | 968 ± 69 | 48589 ± 236 | 258 ± 52 | 15783 ± 145 |
| 284.0 | 1252 ± 85 | 77390 ± 296 | 341 ± 57 | 20896 ± 166 |
| 284.9 | 1135 ± 78 | 74876 ± 291 | | 18005 ± 155 |
| 286.0 | 1094 ± 80 | 78426 ± 297 | | 15326 ± 152 |
| 287.9 | 753 ± 72 | 62188 ± 266 | | 9996 ± 133 |

Table 4.5: Net area of the full energy peaks of the 2287 keV and 5045.8 keV transitions. The areas are calculated for all the experimental runs. The net areas of peaks acquired with different runs at the same energy are summed. Blank rows correspond to runs in which the full energy peak is not visible.

| | **GePD detector, $E_p$=282.0 keV** | **GeDD detector, $E_p$=278.0** |
|---|---|---|
| $E_\gamma$ [keV] | $N_{counts}$ | $N_{counts}$ |
| 2287 | 985 ± 66 | 1406 ± 89 |
| 5013.4 | 1646 ± 189 | 2155 ± 247 |
| 6995.9 | 757 ± 90 | 957 ± 114 |

Table 4.6: Net area of the full energy peaks of all the primary transitions of the 6997.1 keV excited level of $^{22}$Na. The areas are calculated for the experimental runs acquired at the proton beam energy which corresponds to the yield curve maximum (see 4.8). The net areas of peaks acquired with different runs at the same energy are summed.

| | **GePD detector, $E_p$=282.0 keV** | **GeDD detector, $E_p$=278.0** |
|---|---|---|
| $E_\gamma$ [keV] | $N_{counts}$ | $N_{counts}$ |
| 1010.1 | 11250 ± 142 | 19008 ± 211 |
| 1395.1 | 1448 ± 850 | 4959 ± 1273 |
| 1824 | 3239 ± 85 | 5005 ± 118 |
| 2228.1 | 1874 ± 77 | 2731 ± 102 |
| 3938.7 | 748 ± 73 | 1047 ± 117 |
| 4028.7 | 11517 ± 165 | 15737 ± 237 |
| 5014.4 | 10497 ± 232 | 13106 ± 301 |
| 5045.8 | 52050 ± 242 | 69198 ± 293 |
| 5060.5 | 2855 ± 84 | 2856 ± 102 |
| 6414.3 | 3281 ± 110 | 3597 ± 135 |
| 6996.9 | 56251 ± 257 | 74268 ± 300 |

Table 4.7: Net area of the full energy peaks of all the primary transitions of the 6998.1 keV excited level of $^{22}$Na. The areas are calculated for the experimental runs acquired at the proton beam energy which corresponds to the yield curve maximum (see 4.8). The net areas of peaks acquired with different runs at the same energy are summed.

## 4.8 Resonance energy

### 4.8.1 $E_p$=271 keV resonance

To determine the resonance energy it is necessary to study the yield curve, which is obtained considering the yield values of a given primary $\gamma$ ray as a function of the proton beam energy. As explained in 4.2, the yield is given by the ratio of the number of reactions to the number of incident particles. Since to evaluate the resonance energy it is necessary only the shape of the yield curve and not the yield absolute values, it is possible to calculate the yield normalizing the number of net counts of the experimental peaks to the integrated charge:

$$Y = \frac{N_{counts}}{Q} \tag{4.27}$$

where $N_{counts}$ is the net area of the full energy peak, obtained as described in Section 4.7.1, and $Q$ is the integrated charge. Written in this way, the yield is given in units of (n° of counts)/(C).

The resonance energy is obtained considering the yield curve of only one primary transition. For the $E_p = 271$ keV resonance, the yield curve is calculated for the 2287 keV transition, which is the only observed primary transition well separated from other peaks. The experimental yield values for the 2287 keV primary transition are reported in Table 4.8. If different runs are acquired at equal energy, they are summed. The blank rows in Table 4.8 correspond to runs in which the 2287 keV full energy peak was not observed. Indeed, compared to the $E_p$=272 keV resonance, the $E_p$=271 keV one has a lower strength and thus, considering the same runs, the statistics of the latter is worse. As a consequence of the lower statistics, the yield curves suffer higher statistical uncertainties.

| | **GePD detector** | **GeDD detector** |
|---|---|---|
| $E_p$ [keV] | Yield [1/mC] | Yield [1/mC] |
| 273.0 | 0.012 ± 0.005 | |
| 274.1 | 0.027 ± 0.004 | 0.038 ± 0.005 |
| 275.0 | | 0.038 ± 0.007 |
| 276.0 | 0.039 ± 0.003 | 0.047 ± 0.004 |
| 277.0 | 0.040 ± 0.005 | 0.046 ± 0.005 |
| 278.0 | 0.055 ± 0.003 | 0.046 ± 0.003 |
| 279.0 | 0.059 ± 0.004 | 0.033 ± 0.003 |
| 279.9 | 0.059 ± 0.004 | 0.035 ± 0.004 |
| 280.9 | 0.067 ± 0.003 | 0.031 ± 0.003 |
| 282.0 | 0.066 ± 0.004 | 0.015 ± 0.004 |
| 283.0 | 0.072 ± 0.005 | 0.019 ± 0.004 |
| 284.0 | 0.056 ± 0.004 | 0.015 ± 0.003 |
| 284.9 | 0.045 ± 0.003 | |
| 286.0 | 0.036 ± 0.003 | |
| 287.9 | 0.020 ± 0.002 | |

Table 4.8: Yield values for the 2287 keV $\gamma$ rays acquired with the GePD and the GeDD detectors. Blank rows correspond to runs in which the full energy peak is not visible.

Once calculated the yield values, in order to determine the resonance energy, it is necessary to determine the beam energy at which the yield curve reaches its maximum value. Indeed, since the yield maximum is linked to the detector's efficiency, it is reached when the efficiency for collecting the $\gamma$ rays produced in the reaction is the highest and, thus, the resonance is populated in front of the detector. To obtain the energy corresponding to the maximum $E_{max}$, the yield curves are fitted using a bell shape function that takes into account the asymmetry of the curve [53]:

$$Y(E) = Aexp\left\{-\frac{1}{2}\left[\frac{E - E_{max}}{\sigma + kexp(-\frac{E-E_{max}}{E_{max}})}\right]^2\right\} \tag{4.28}$$

where $A$, $E_{max}$, $\sigma$ and $k$ are parameters to be determined from the fit. For the values acquired using the GeDD detector the trend of the yield curve is not well defined and it was chosen to fix the values of the parameters $\sigma$ and $k$ to the ones from the fit of the 5045.8 keV yield

curve obtained for the same detector (see 4.8.2). Figure 4.29 and 4.30 show the yield curve fitted with eq. 4.28 for the GePD and GeDD detectors respectively. The fit coefficients and the $\chi^2/ndf$ are reported in Table 4.9. In addition to the statistical error obtained from the fit and reported in Table 4.9, there is also a systematic uncertainty associated to $E_{max}$, that is equal to 0.3 keV and is due to the accelerator's uncertainty on the energy (see 3.1).

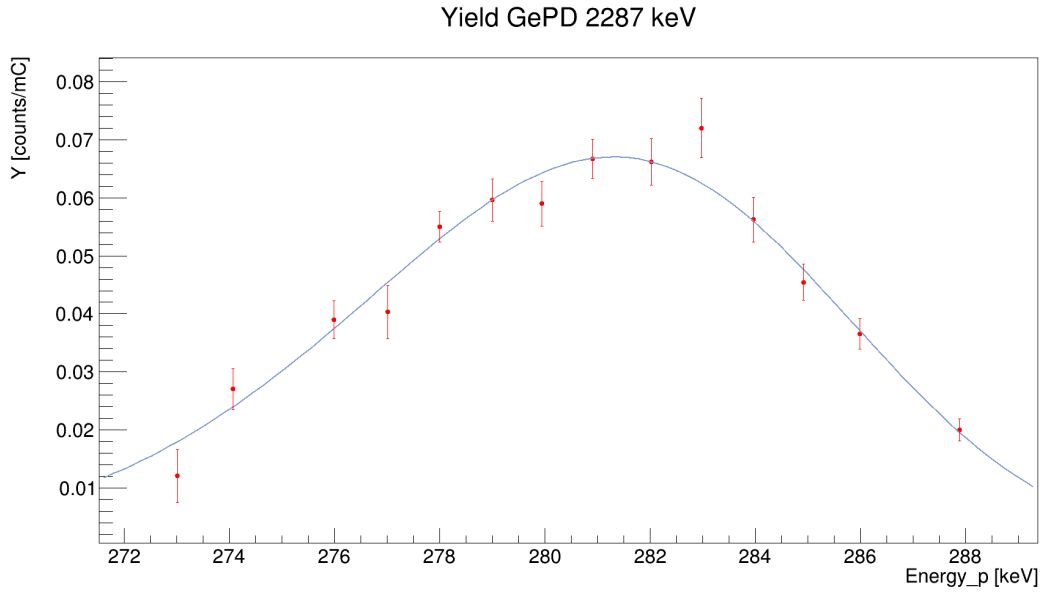


Figure 4.29: Yield curve for the 2287 keV primary transition, fitted with eq. 4.28. Data acquired using the GePD detector.

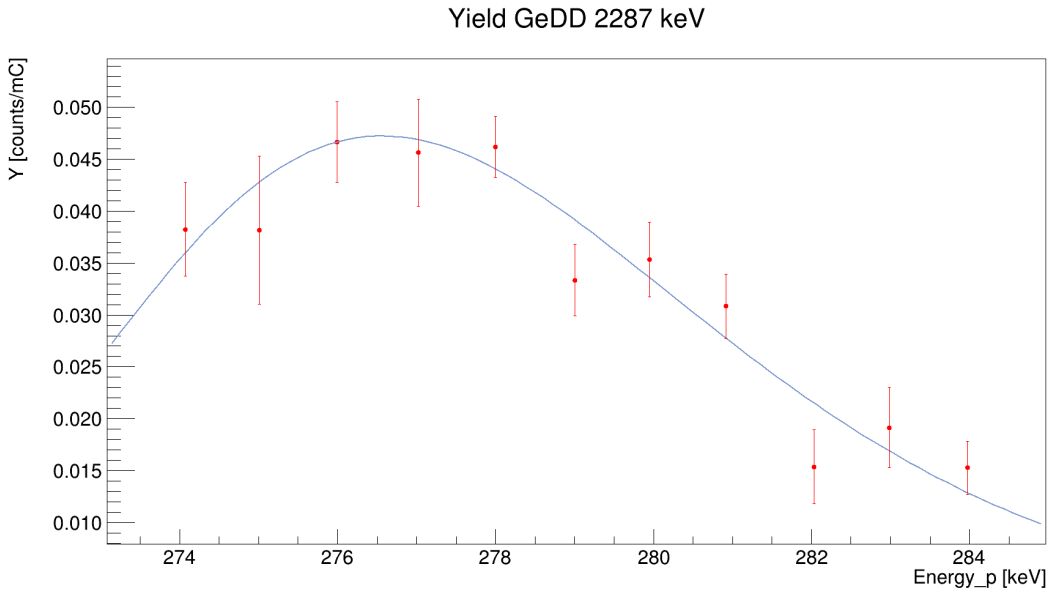


Figure 4.30: Yield curve for the 2287 keV primary transition, fitted with eq. 4.28. Data acquired using the GeDD detector.

| Detector | $A$ [1/mC] | $E_{max}$ [keV] | $\sigma$ [keV] | $k$ [keV] | $\chi^2/ndf$ |
|---|---|---|---|---|---|
| **GePD** | 0.067±0.002 | 281.3±0.2 | 12±5 | -17±5 | 10.322/10 |
| **GeDD** | 0.047±0.002 | 276.6±0.2 | 38.2± 0.8 | -34.6±0.8 | 9.406/9 |

Table 4.9: Coefficients obtained from the fit of the yield curve for the 2287 keV transition. The parameters $\sigma$ and $k$ for the fit of the yield values acquired with GeDD detector are fixed using the values reported in Table 4.12.

In the analysis of the spectra acquired by the GePD detector, another yield curve is obtained considering the net areas of the 2287 keV peak calculated using the method described in [42]. As in the previous case, the yield curve is fitted using the function in eq. 4.28 and the fit coefficient $E_{max}$ is equal to $E_{max} = (280.7 \pm 0.1)$ keV (goodness of the fit $\chi^2/ndf = 21.0193/11$). The adopted $E_{max}$ value for the GePD detector is $E_{max,GePD} = (280.9 \pm 0.1)$ keV and it is obtained with a weighted average of the coefficients from the two fits. As mentioned above, a systematic uncertainty of 0.3 keV must be added to the statistical uncertainty on $E_{max,GePD}$ to take into account the accelerator's calibration.

Eventually, the resonance energy in the laboratory is obtained as the difference between the proton beam energy corresponding to the maximum yield and the energy that is lost in the path up to the detector:

$$E_{R,lab} = E_{max} - (x_{coll} + x_{det}) \cdot \frac{dE}{dx} - \Delta E_{pipe} \tag{4.29}$$

where

- $E_{max}$ is the beam energy that corresponds to the maximum of the yield curve.
- $(x_{coll} + x_{det}) \cdot \frac{dE}{dx}$ is the energy lost by the beam in the collimator and in the chamber up to the detector. $x_{coll} = (2.5 \pm 0.5)$ cm is the effective collimator's length and $x_{det}$ is the detector's distance from the collimator (see 3.3.1). $dE/dx$ is the energy loss per unit path length obtained from SRIM.
- $\Delta E_{pipe} = (0.67 \pm 0.01)$ keV is the energy lost by the proton beam in the tube that connects the first pumping stage and the target chamber.

Table 4.10 shows the values of the resonance energy in the laboratory obtained for the $E_p$=271 keV resonance. The total value is obtained from the average weighted on the statistical uncertainties of the resonance energies obtained independently with the two detectors.

| Detector | $E_{R,lab}$ [keV] |
|---|---|
| **GePD** | 271.6±0.5 |
| **GeDD** | 271.1±0.5 |
| **total** | 271.6 ±0.5 |

Table 4.10: Resonance energy in the laboratory for the $E_p$=271 keV resonance.

### 4.8.2 $E_p$=272 keV resonance

The procedure to obtain the $E_p = 272$ keV resonance energy in the laboratory is analogous to the one adopted for the $E_p = 271$ keV resonance. For this resonance, the yield curve is calculated for the 5045.8 keV primary transition. The choice of this transition is dictated by the fact that the full energy peaks are well distinguishable from other peaks in the experimental spectra, and that the branching ratio is higher compared to other primary $\gamma$ rays whose

experimental peaks are isolated. The experimental yield values for the 5045.8 keV transition are reported in Table 4.11. As before, runs acquired at equal energy are summed. The yield curves for the 5045.8 keV transition are fitted using eq. 4.28 and are shown in Figure 4.31 and 4.32 for the GePD and the GeDD detectors respectively. The fit coefficients and the $\chi^2/ndf$ are reported in Table 4.12. As above, the uncertainty on $E_{max}$ has a statistical contribution from the fit, reported in Table 4.12 and a systematic contribution of 0.3 keV. Eventually, the resonance energy in the laboratory is calculated using eq 4.29. The results are reported in Table 4.13. In this case, the resonance energies obtained with the GePD and GeDD detectors are in excellent agreement.

| | **GePD detector** | **GeDD detector** |
|---|---|---|
| $E_p$ [keV] | Yield [1/mC] | Yield [1/mC] |
| 273.0 | 0.34 ± 0.01 | 0.53 ± 0.02 |
| 274.1 | 0.98 ± 0.01 | 1.25 ± 0.01 |
| 275.0 | 1.47 ± 0.03 | 1.74 ± 0.03 |
| 276.0 | 1.82 ± 0.02 | 2.08 ± 0.02 |
| 277.0 | 2.21 ± 0.02 | 2.25 ± 0.02 |
| 278.0 | 2.65 ± 0.01 | 2.27 ± 0.01 |
| 279.0 | 3.04 ± 0.02 | 2.11 ± 0.01 |
| 279.9 | 3.40 ± 0.02 | 1.96 ± 0.01 |
| 280.9 | 3.61 ± 0.02 | 1.73 ± 0.01 |
| 282.0 | 3.71 ± 0.02 | 1.41 ± 0.01 |
| 283.0 | 3.60 ± 0.03 | 1.17 ± 0.01 |
| 284.0 | 3.39 ± 0.02 | 0.914 ± 0.009 |
| 284.9 | 2.99 ± 0.02 | 0.718 ± 0.007 |
| 286.0 | 2.53 ± 0.01 | 0.493 ± 0.005 |
| 287.9 | 1.646 ± 0.009 | 0.265 ± 0.004 |

Table 4.11: Yield values for the 5045.8 keV $\gamma$ rays acquired with the GePD and the GeDD detectors.

| Detector | $A$ [1/mC] | $E_{max}$ [keV] | $\sigma$ [keV] | $k$ [keV] | $\chi^2/ndf$ |
|---|---|---|---|---|---|
| **GePD** | 3.698±0.009 | 281.71±0.02 | 12.5±0.6 | -7.7±0.6 | 655.76/11 |
| **GeDD** | 2.300±0.008 | 277.82±0.02 | 38.2±0.8 | -34.6±0.8 | 309.031/11 |

Table 4.12: Coefficients obtained from the fit of the yield curve of the 5045.8 keV transition.

| Detector | $E_{R,lab}$ [keV] |
|---|---|
| **GePD** | 272.4±0.5 |
| **GeDD** | 272.4±0.4 |

Table 4.13: Resonance energy in the laboratory for the $E_p$=272 keV resonance.

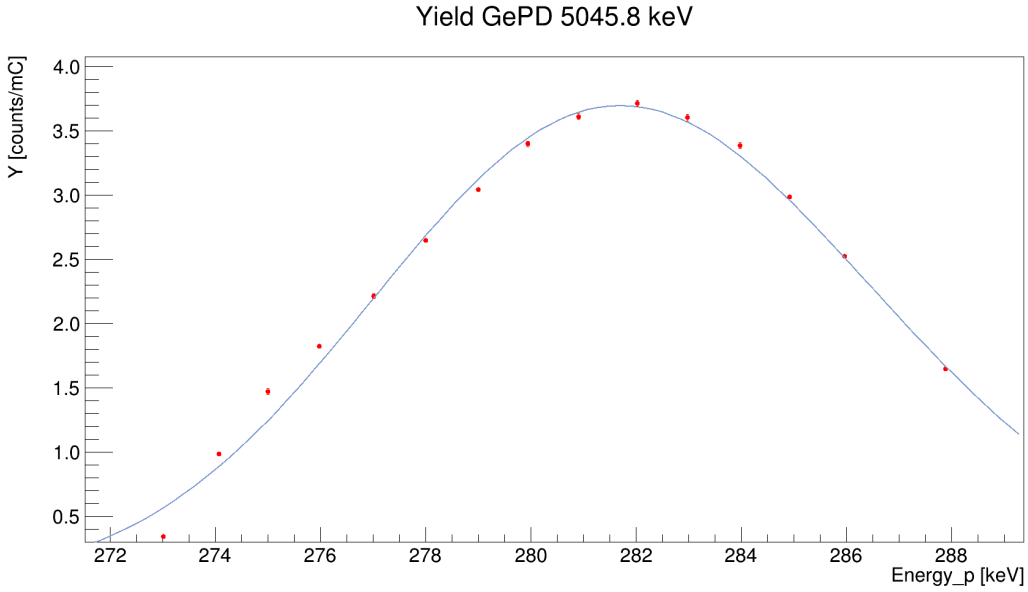


Figure 4.31: Yield curve for the 5045.8 keV primary transition, fitted with eq. 4.28. Data acquired using the GePD detector.

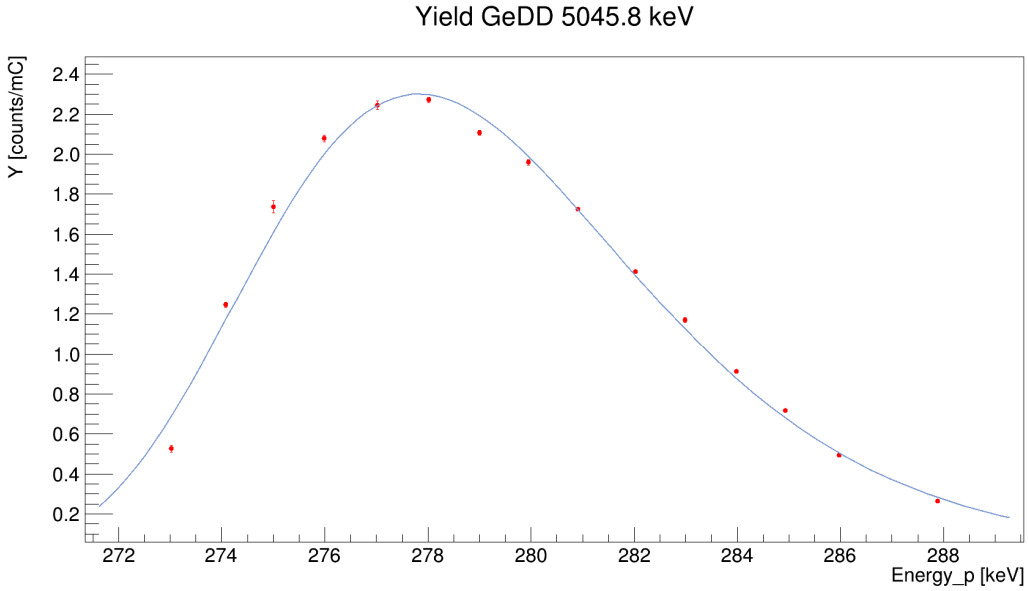


Figure 4.32: Yield curve for the 5045.8 keV primary transition, fitted with eq. 4.28. Data acquired using the GeDD detector.

At this point it is possible to compare the calculated resonance energies (Table 4.10 and 4.13) with the values reported in literature. From literature [1], the resonances of the doublet at $E_p = 272$ keV are expected to be separated by an energy interval of $(0.888 \pm 0.005)$ keV, which is consistent with the values from this analysis. The resonance energies from literature are summarized in Table 2.4 and for both resonances they are slightly lower than the obtained ones. Eventually, it is necessary to note that the uncertainties associated to the resonance energy obtained in this analysis are larger than the ones reported in literature (Table 2.4). However, the latter do not take into account systematic uncertainties from the calibration of the accelerator.

## 4.9 Branching ratios

The two resonances at $E_p = 271$ and 272 keV populate two excited states of $^{22}$Na that de-excite emitting $\gamma$ rays of different energies. It is possible to calculate the branching ratios for the decay modes of the excited level in the hypothesis that all primary transitions are experimentally observed. This assumption is not verified for the level at 6997.1 keV, populated by the $E_p = 271$ keV resonance, because one of the primary transitions reported in literature [32] is not observed in the acquired spectra. As a consequence, the branching ratios are calculated only for the 6998.1 keV level, which is populated by the 272 keV resonance.

The branching ratio for the $i-th$ transition is obtained as

$$BR_i = \frac{N_{max,i}/\eta_i}{\sum_j N_{max,j}/\eta_j} \tag{4.30}$$

where $N_{max,i}$ is the net number of counts in the full energy peak of the $i-th$ $\gamma$ ray, $\eta_i$ is the associated efficiency and the index $j$ runs over all the primary transitions. The subscript $max$ refers to values obtained for the run acquired at the proton beam energy closest to the one corresponding to the maximum of the yield curve. Thus, the branching ratios are calculated for the runs at energy equal to $E_p = 282.0$ keV and $E_p = 278.0$ keV for the GePD and the GeDD detectors respectively. The obtained results are reported in Table 4.14.

| | **GePD detector** | **GeDD detector** |
|---|---|---|
| $E_\gamma$ [keV] | BR % | BR % |
| 1010.1 | 2.30 ± 0.03 | 2.42 ± 0.03 |
| 1395.1 | 0.4 ± 0.2 | 0.8 ± 0.2 |
| 1824 | 0.95 ± 0.03 | 0.98 ± 0.02 |
| 2228.1 | 0.63 ± 0.03 | 0.63 ± 0.02 |
| 3938.7 | 0.38 ± 0.04 | 0.39 ± 0.04 |
| 4028.7 | 6.0 ± 0.1 | 6.0 ± 0.1 |
| 5014.4 | 6.5 ± 0.2 | 6.1 ± 0.1 |
| 5045.8 | 32.4 ± 0.3 | 32.2 ± 0.3 |
| 5060.5 | 1.78 ± 0.05 | 1.33 ± 0.05 |
| 6414.3 | 2.50 ± 0.09 | 2.10 ± 0.08 |
| 6996.9 | 46.2 ± 0.5 | 47.2 ± 0.4 |

Table 4.14: Branching ratios for the primary transitions of the 6998.1 keV excited level of $^{22}$Na.

## 4.10 Resonance strength

The gas target can be approximated as infinitely thick because the total width $\Gamma$ of the resonances under study is small compared to the target thickness in energy. Thus, the resonance strength is easily obtained from eq. 4.8

$$\omega\gamma = \frac{2\epsilon_r}{\lambda_r^2} Y_{max} \tag{4.31}$$

The terms of this equation are obtained as follows:

- $\epsilon_r$ is the effective stopping power of the gas target, calculated at the resonance energy. Assuming that $n_x$ is the concentration of the active nuclei and $n_y$ the concentration of inactive ones (i.e. nuclei that do not produce the reaction of interest), the effective stopping power is given by [5]

$$\epsilon_{eff} = \epsilon_x + \frac{n_y}{n_x}\epsilon_y \tag{4.32}$$

  In the experiment, the target is natural neon gas, which is a mixture of 0.27% $^{21}$Ne, 90.48% $^{20}$Ne and 9.25% $^{22}$Ne. In the hypothesis that the stopping power $\epsilon_{Ne}$ is the same for all the neon isotopes, the effective stopping power for $^{21}$Ne can be written as

$$\epsilon_{eff} = \frac{\epsilon_{Ne}}{0.0027} \tag{4.33}$$

- $\lambda_r$ is the de Broglie wave length and it is calculated with eq. 4.9.
- $Y_{max}$ is the value of maximum yield. In this case, differently from Section 4.8, it is necessary to write the yield as per the definition, in the correct unit of measurements. Neglecting the angular distribution, from eq. 4.2:

$$Y = \frac{N_{counts}}{N_B \eta BR} \tag{4.34}$$

  The maximum value $Y_{max}$ is obtained with different procedures for the two resonances at $E_p$=271 keV and $E_p$=272 keV. A description of the method adopted in each case is given in the respective subsections.

### 4.10.1 $E_p$=271 keV resonance

In the study of the spectra acquired during the experiment, not all the expected primary transitions of the 6997.1 keV excited level of $^{22}$Na are observed. For this reason, to evaluate $Y_{max}$ it is necessary to rely on the branching ratios from literature. Using the general formula for the yield, eq. 4.34, $Y_{max}$ is obtained from the yield value of the 2287 keV transition of the run acquired at the proton beam energy closest to the maximum of the yield curve (see 4.8.1):

$$Y_{max} = e \cdot \frac{N_{2287}}{Q\eta_{2287} BR_{2287}} \tag{4.35}$$

where $e$ is the electron charge, $N_{2287}$ is the net area of the 2287 keV full energy peak, $Q$ is the integrated charge, $\eta_{2287}$ is the efficiency to detect the 2287 keV $\gamma$ ray and $BR_{2287}$ is the branching ratio from literature [32]. For the GePD detector the experimental runs used in the calculation are acquired at $E_p$=280.9 keV, while for the GeDD detector at $E_p$=276.0 keV. As before, runs at equal energy are summed. The yield values and the efficiencies are reported in Table 4.15. The obtained values of $Y_{max}$ are reported in Table 4.16, together with the de Broglie wavelength calculated using eq. 4.9. In the calculation, the total value of the resonance energy in the laboratory is adopted (see Table 4.10).

| | **GePD detector** | | **GeDD detector** | |
|---|---|---|---|---|
| $E_\gamma$ [keV] | Yield | $\eta$ | Yield | $\eta$ |
| 2287 | 0.067 ± 0.003 | 0.00738 ± 0.00003 | 0.047 ±0.004 | 0.00506 ± 0.00003 |

Table 4.15: Yield values and efficiencies for the 2287 keV primary transitions of the $E_p$=271 keV resonance. The yields are calculated for the run whose energy is the closest to the maximum of the yield curve.

| Detector | $\lambda^2/2$ [cm$^2$] | $Y_{max}$ |
|---|---|---|
| **GePD** | $(1.655\pm0.003)\cdot10^{-23}$ | $(9\pm1)\cdot10^{-15}$ |
| **GeDD** | $(1.655\pm0.003)\cdot10^{-23}$ | $(9\pm1)\cdot10^{-15}$ |

Table 4.16: Values of $Y_{max}$ and $\lambda^2/2$ obtained from the experimental data acquired by the two detectors.

The resonance strength is evaluated with eq. 4.31. Table 4.17 reports the values obtained for the data acquired by the two detectors. The total resonance strength is obtained as the weighted average of these two values. Moreover, the resonance strength from literature is also reported. The resonance strength values and the associated uncertainties are shown in Figure 4.33. The values obtained with the GePD and GeDD detectors are in agreement within $1\sigma$ uncertainty. What is more, the total and the literature resonance strengths are compatible within $1\sigma$ uncertainty.

However, the resonance strength value obtained for the $E_p = 271$ resonance is preliminary and it still needs to be corrected for the energy straggling effect. This effect accounts for the fact that the energy loss of protons in neon gas is a statistical process whose fluctuations have the consequence that the energy distribution of particles enlarges as protons pass through the target. The correction will be applied using Monte Carlo simulations, which, at the moment, are under development.

| | **GePD** | **GeDD** | **Total** | **Literature** [1] |
|---|---|---|---|---|
| $\omega\gamma$ [meV] | 2.4±0.3 | 2.5±0.3 | 2.4±0.3 | 2.1±0.4 |

Table 4.17: Resonance strength values obtained for the $E_p$=271 keV resonance. The results are reported separately for each detector; the total resonance strengths refers to the value obtained with the weighted average of the values of the single detectors. Moreover the literature value is also reported.

### 4.10.2 $E_p$=272 keV resonance

In the case of the $E_p$=272 keV resonance, it is assumed that all the primary transitions are observed. In this hypothesis, $Y_{max}$ is given by

$$Y_{max} = e \cdot \sum_i \frac{N_{counts,i}}{Q_i \eta_i} \tag{4.36}$$

where $e$ is the electron charge and it is introduced to obtain the correct unit of measurement. The sum is performed over the yield values, divided by the respective efficiency, of all the primary transitions of the experimental run acquired with the proton beam energy closest to the maximum of the yield curve (see 4.8.2). For the GePD detector the experimental runs

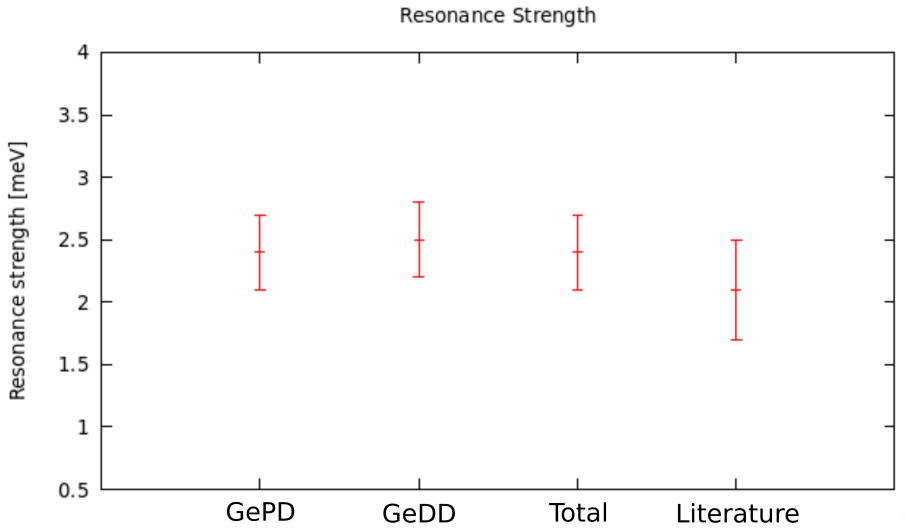


Figure 4.33: Comparison of the resonance strength values obtained with the two detectors for the $E_p = 271$ keV resonance. The total value and the literature one are also reported.

used in the calculation are acquired at $E_p$=282.0 keV energy, while for the GeDD detector at $E_p$=278.0 keV. Using eq. 4.36, the branching ratios from literature are not necessary to evaluate $Y_{max}$. The values of the yield for the primary transitions and the associated efficiencies used to calculate the resonance strength are reported in Table 4.18. As for the calculation of the resonance energy, runs at equal energy are summed.

| | **GePD detector** | | **GeDD detector** | |
|---|---|---|---|---|
| $E_\gamma$ [keV] | Yield | $\eta$ | Yield | $\eta$ |
| 1010.1 | 0.81 ± 0.01 | 0.01235 ± 0.00004 | 0.625 ± 0.008 | 0.00932 ± 0.00005 |
| 1395.1 | 0.10 ± 0.06 | 0.01021 ± 0.00004 | 0.16 ± 0.04 | 0.00741 ± 0.00004 |
| 1824 | 0.232 ± 0.006 | 0.00861 ± 0.00003 | 0.164 ± 0.004 | 0.00606 ± 0.00003 |
| 2228.1 | 0.134 ± 0.006 | 0.00752 ± 0.00003 | 0.090 ± 0.003 | 0.00517 ± 0.00003 |
| 3938.7 | 0.054 ± 0.005 | 0.00494 ± 0.00002 | 0.034 ± 0.004 | 0.00319 ± 0.00002 |
| 4028.7 | 0.82 ± 0.01 | 0.00486 ± 0.00002 | 0.517 ± 0.008 | 0.00313 ± 0.00001 |
| 5014.4 | 0.75 ± 0.02 | 0.00407 ± 0.00002 | 0.43 ± 0.01 | 0.00256 ± 0.00001 |
| 5045.8 | 3.73 ± 0.03 | 0.00405 ± 0.00002 | 2.27 ± 0.02 | 0.00255 ± 0.00001 |
| 5060.5 | 0.204 ± 0.006 | 0.00404 ± 0.00002 | 0.094 ± 0.003 | 0.00254 ± 0.00001 |
| 6414.3 | 0.235 ± 0.008 | 0.00331 ± 0.00002 | 0.118 ± 0.004 | 0.00203 ± 0.00001 |
| 6996.9 | 4.03 ± 0.03 | 0.00307 ± 0.00002 | 2.44 ± 0.02 | 0.00186 ± 0.00001 |

Table 4.18: Yield values and efficiencies for all the primary transitions of the $E_p$=272 keV resonance. The yields are calculated for the run whose energy is the closest to the maximum of the yield curve.

The values of $Y_{max}$ and the de Broglie wavelength are reported in Table 4.19 for both detectors.

Eventually, the resonance strength is evaluated using eq 4.31. The total resonance strength is obtained with a weighted average of the resonance strengths obtained using the two detec-

| Detector | $\lambda^2/2$ [cm$^2$] | $Y_{max}$ |
|---|---|---|
| **GePD** | $(1.650\pm0.003)\cdot10^{-23}$ | $(4.55\pm0.03)\cdot10^{-13}$ |
| **GeDD** | $(1.650\pm0.003)\cdot10^{-23}$ | $(4.45\pm0.03)\cdot10^{-13}$ |

Table 4.19: Values of $Y_{max}$ and $\lambda^2/2$ obtained from the experimental data acquired by the two detectors.

tors. The results are reported in Table 4.20. Figure 4.34 shows the resonance strength values and the associated uncertainties. The resonance strengths obtained with the two detectors are in agreement within $2\sigma$ uncertainty. The uncertainty associate to the total resonance strength obtained in this analysis is significantly improved compared to the one reported in literature. On the other hand, the two values are not in agreement and differ of about 40 meV. The new primary transitions of the 6998.1 keV excited level identified at LUNA are expected to contribute increasing the resonance strength value. As in the case of the $E_p = 271$ keV resonance, the resonant strength value obtained in this analysis is preliminary and it still needs to be corrected for the straggling effect.

| | **GePD** | **GeDD** | **Total** | **Literature** [2] |
|---|---|---|---|---|
| $\omega\gamma$ [meV] | 124±2 | 121±2 | 122±2 | 82±13 |

Table 4.20: Resonance strength values obtained for the $E_p$=272 keV resonance. The results are reported separately for each detector; the total resonance strengths refers to the value obtained with the weighted average of the values of the single detectors. Moreover, the literature value is also reported.

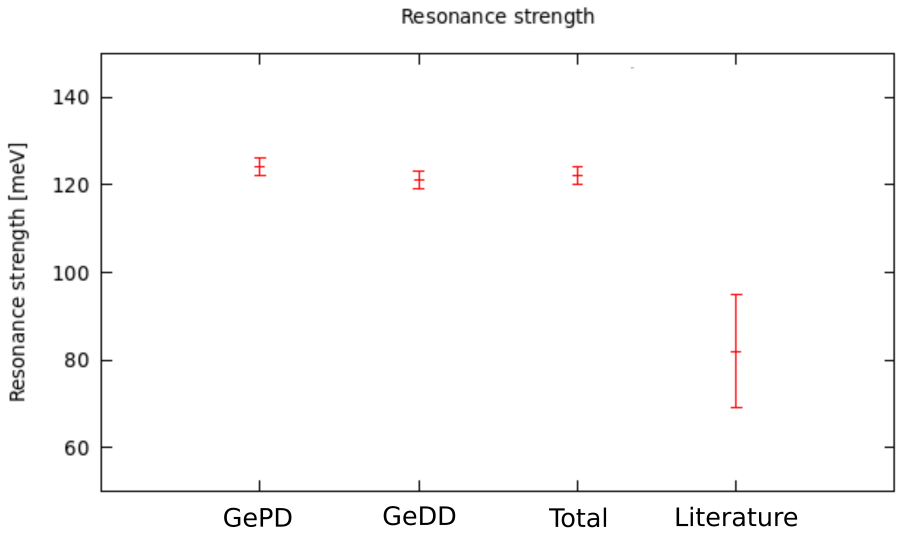


Figure 4.34: Comparison of the resonance strength values obtained with the two detectors for the $E_p = 272$ keV resonance. The total value and the literature one are also reported.

# Conclusions

This thesis is focused on the study of the two resonances at $E_p = 271$ and 272 keV of the $^{21}$Ne(p,$\gamma$)$^{22}$Na reaction, which is being studied in an ongoing experiment at LUNA. The analyzed data were acquired in Autumn 2022, during the first phase of the experiment. I contributed to the data taking with several shifts at the Gran Sasso National Laboratory and I took care of the complete analysis of the experimental data.

The $E_p = 271$ and 272 keV resonances populate the excited levels of $^{22}$Na at $E_x = 6997.1$ and 6998.1 keV respectively, and the $\gamma$ rays emitted in the de-excitation process are exploited to separate the contributions from the two resonances. In the analysis of the experimental spectra acquired at LUNA, the $\gamma$ ray at $E_\gamma = 5468.7$ keV, which is one of the four primary transitions expected from literature for the de-excitation of the $E_x = 6997.1$ keV level [32], has never been observed. The non observation of this transition may be attributed to the low strength of the $E_p = 271$ keV resonance and the consequent low statistic in the acquired data. Instead, four new primary transitions at $E_\gamma = 1010.1, 1395.1, 2228.1$ and 3939 keV have been observed for the de-excitation of the $E_x = 6998.1$ keV excited level. Further analysis is ongoing to validate the correct identification of these new transitions.

To characterize the resonances, both the resonance energies and strengths have been calculated. These calculations have been performed independently for the data acquired by the two high purity germanium detectors. In the case of the $E_p = 271$ keV resonance, the resonance energy values obtained with the two high purity germanium detectors are in agreement within $1\sigma$ uncertainty and the weighted average of these values is equal to $E_{R,lab} = (271.6 \pm 0.5)$ keV. Instead, the resonance energy values obtained for the $E_p = 272$ keV resonance are in excellent agreement within the two detectors, and the measured resonance energy is $E_{R,lab} = (272.4 \pm 0.5)$ keV. From literature [1], it is expected that this doublet of resonances is separated by (0.888$\pm$0.005) keV and the results of the data analysis reported in this thesis are consistent with this energy interval. However, in comparison to [1], the obtained resonance energy values for the $E_p = 271$ keV resonance and the $E_p = 272$ keV one are higher by 0.9 keV and 0.8 keV, respectively.

The resonance strength values obtained using the spectra acquired by the two detectors are in agreement within $1\sigma$ and $2\sigma$ uncertainty for the $E_p = 271$ and 272 keV resonances, respectively. The total resonance strength is the weighted average of the resonance strengths obtained with the two detectors. The total resonance strength of the $E_p = 271$ keV resonance is $\omega\gamma = (2.4 \pm 0.3)$ meV and it is compatible with $\omega\gamma = (2.1 \pm 0.4)$ meV reported in literature [1]. Instead, the total resonance strength obtained for the $E_p = 272$ keV resonance is $\omega\gamma =$ (122$\pm$2) meV. The uncertainty associated to the value of the total resonance strength obtained in this analysis is significantly reduced compared to the value $\omega\gamma = (82 \pm 13)$ meV reported in literature by Görres et al. [2]. However, the two values are not compatible since the resonance strength obtained in this analysis is higher by 40 meV than the literature value. An increase in the resonance strength value is expected to arise from the new primary transitions identified for the de-excitation of the 6998.1 keV level of $^{22}$Na.

These results are still preliminary, and further data analysis is still ongoing. In particular,

the straggling effect has still to be taken into account and this correction will be applied using the results of Monte Carlo simulations of the experiment, which, at the moment, are under development.

The implications for astrophysics resulting from the new measurement of these two resonances performed at LUNA will be addressed in the close future.

# Bibliography


[1] H. W. Becker et al. "Low energy resonances in $^{21}$Ne(p,$\gamma$)$^{22}$Na examined with a high energy resolution ion beam". In: *Hadrons and Nuclei* 343 (1992), pp. 361–366.

[2] J. Görres et al. "Search for low-energy resonances in $^{21}$Ne(p,$\gamma$)$^{22}$Na and $^{22}$Ne(p,$\gamma$)$^{23}$Na". In: *Nuclear Physics A* 385 (1982), pp. 57–75.

[3] E. M. Burbidge et al. "Synthesis of the Elements in Stars". In: *Reviews of Modern Physics* 29.4 (1957), p. 547.

[4] C. E. Rolfs and W. S. Rodney. *Cauldrons in the Cosmos: nuclear astrophysics*. The University of Chicago Press, 1988.

[5] C. Iliadis. *Nuclear Physics of Stars*. Second Edition. Wiley-VCH, 2015.

[6] A. Boeltzig et al. "Shell and explosive hydrogen burning". In: *The European Physics Journal A* 52 (2016).

[7] J. B. Marion and W. A. Fowler. "Nucelar reactions with the neon isotopes in stars". In: *The Astrophysical Journal* 125 (1957), p. 221.

[8] E. Masha. *Astrophysical nuclear reactions on Neon isotopes at LUNA*. Ph.D. Theses. 2022.

[9] R. M. Cavallo, A. V. Sweigart, and R. A. Bell. "The production of sodium and aluminium in globular cluster red giant stars". In: *The Astrophysical Journal* 464 (1996), pp. L79–L82.

[10] R. M. Cavallo, A. V. Sweigart, and R. A. Bell. "Proton-capture nucleosynthesis in globular cluster red giant stars". In: *The Astrophysical Journal* 492 (1998), pp. 575–595.

[11] R.G. Izzard et al. "Reaction rate uncertainties and the operation of the NeNa and MgAl chains during HBB in intermediate-mass AGB stars". In: *Astronomy & Astrophysics* 466 (2007), pp. 641–648.

[12] J. José and M. Hernanz. "Nucleosynthesis in classical nova explosions". In: *Journal of Physics G: Nuclear and Particle Physics* 34 (2007), R431–R458.

[13] C. Iliadis et al. "Proton-induced thermonuclear reaction rates for A=20-40 nuclei". In: *The Astrophysical Journal Supplement Series* 134 (2001), pp. 151–171.

[14] S. Lyons et al. "Determination of $^{20}$Ne(p,$\gamma$)$^{21}$Na cross sections from $E_p = 500-2000$ keV". In: *Physical Review C* 97 (2018), p. 065802.

[15] M. Williams et al. "First inverse kinematics study of the $^{22}$Ne(p,$\gamma$)$^{23}$Na reaction and its role in AGB star and classical nova nucleosynthesis". In: *Physical Review C* 102 (2020), p. 035801.

[16] C. Iliadis et al. "Charged-particle thermonuclear reaction rates:III. Nuclear physics input". In: *Nuclear Physics A* 841 (2010), pp. 251–322.

[17] F. Cavanna at al. "Three New Low-Energy Resonances in the $^{22}$Ne(p,$\gamma$)$^{23}$Na Reaction". In: *Physical Review Letters* 115 (2015), p. 252501.

[18] F. Cavanna et al. "Erratum: Three New Low-Energy Resonances in the $^{22}$Ne(p,$\gamma$)$^{23}$Na Reaction". In: *Physical Review Letters* 120 (2018), 239901(E).

[19] F. Ferraro et al. "Direct Capture Cross Section and the $E_p = 71$ and 105 keV Resonances in the $^{22}$Ne(p,$\gamma$)$^{23}$Na Reaction". In: *Physical Review Letters* 121 (2018), p. 172701.

[20] F. Cavanna. *A direct measurement of the $^{22}$Ne(p,$\gamma$)$^{23}$Na reaction down to the energies of astrophysical interest*. Ph.D. Thesis. 2015.

[21] R. Depalo. *The neon-sodium cycle: Study of the $^{22}$Ne(p,$\gamma$)$^{23}$Na reaction at astrophysical energies*. Ph.D. Thesis. 2015.

[22] K. J. Kelly et al. "New measurements of low-energy resonances in the $^{22}$Ne(p,$\gamma$)$^{23}$Na reaction". In: *Physical Review C* 95 (2017), p. 015806.

[23] A. Lennarz et al. "First inverse kinematics measurement of key resonances in the $^{22}$Ne(p,$\gamma$)$^{23}$Na reaction at stellar temperatures". In: *Physics Letters B* 807 (2020), p. 135539.

[24] A. Boeltzig et al. "Direct measurements of low-energy strengths of the $^{23}$Na(p,$\gamma$)$^{24}$Mg reaction for astrophysics". In: *Physics Letters B* 795 (2019), pp. 122–128.

[25] M. Hernanz et al. "Models and observation of high energy emission from stellar explosions: novae and type Ia supernovae". In: *39TH ESLAB Symposium on Trends in Space Science and Cosmic Vision 2020* (2005).

[26] C. L. Fryer et al. "The Case for a New MeV Gamma-Ray Mission: Radionuclide Astronomy in the 2020s". In: *Bulletin of the American Astronomical Society* 51.3 (2019).

[27] S. Amari et al. "Interstellar graphite in meteorites". In: *Nature* 345 (1990), pp. 238–240.

[28] M. Pignatari et al. "Carbon-rich presolar grains from massive stars: subsolar $^{12}$C/$^{13}$C and $^{14}$N/$^{15}$N ratios and the mystery of $^{15}$N". In: *The Astrophysical Journal Letters* 808.2 (2015), p. L43.

[29] H. L. Berg et al. "Proton induced resonances on $^{21}$Ne". In: *Nuclear Physics A* 276 (1977), pp. 168–188.

[30] J. Görres et al. "Proton-induced direct capture on $^{21}$Ne and $^{22}$Ne". In: *Nuclear Physics A* 408 (1983), pp. 372–396.

[31] A. L. Sallaska et al. "STARLIB: a next-generation reaction-rate library for Nuclear Astrophysics". In: *The Astrophysical Journal Supplement Series* 207:18 (2013).

[32] URL: https://www.nndc.bnl.gov/nudat3/. (accessed: 24.04.2023).

[33] C. Broggini at al. "LUNA: Nuclear Astrophysics Deep Underground". In: *Annual Review of Nuclear and Particle Science* 60 (2010), pp. 53–73.

[34] D. Bemmerer at al. "Feasibility of low-energy radiative-capture experiments at the LUNA underground accelerator facility". In: *The European Physical Journal A* 24 (2005), pp. 313–319.

[35] C. Broggini. "The Luna experiment". In: *EPJ Web of Conferences* 136, 01008 (2017).

[36] U. Greife at al. "Laboratory for Underground Nuclear Astrophysics (LUNA)". In: *Nuclear Instruments and Methods in Physics Research Section A: Accelerators, Spectrometers, Detectors and Associated Equipment* 350 (1994), pp. 327–337.

[37] A. Formicola at al. "The LUNA II 400 kV accelerator". In: *Nuclear Instruments and Methods in Physics Research* A 507 (2003), pp. 609–616.

[38] URL: https://www.lngs.infn.it/en/luna. (accessed: 16.04.2023).

[39] A. Best at al. "Underground nuclear astrophysics: Why and how". In: *The European Physical Journal A* 52 (2016).

[40] F. Cavanna at al. "A new study of the $^{22}$Ne(p,$\gamma$)$^{23}$Na reaction deep underground: Feasibility, setup and first observation of the 186 keV resonance". In: *The European Physical Journal A* 50.11 (2014).

[41] F. Ferraro at al. "A high efficiency gas target setup for underground experiments, and redetermination of the branching ratio of the 189.5 keV $^{22}$Ne(p,$\gamma$)$^{23}$Na resonance". In: *The European Physical Journal A* 54 (2018).

[42] G.R. Gilmore. *Practical Gamma-ray Spectrometry*. Second Edition. John Wiley & Sons, Ltd, 2008.

[43] C. Casella at al. "A new setup for the underground study of capture reactions". In: *Nuclear Instruments and Methods in Physical Research A* 489 (2002), pp. 160–169.

[44] C. Broggini at al. "LUNA: Status and prospects". In: *Progress in Particle and Nuclear Physics* 98 (2018), pp. 55–84.

[45] W. R. Leo. *Techniques for Nuclear and Particle Physics Experiments: A How-to Approach*. Fourth Edition. Springer Verlag, 1987.

[46] J. F. Ziegler and M. D. Ziegler and J. P. Biersack. *SRIM*. Version SRIM-2013.00. URL: http://www.srim.org/.

[47] J. F. Ziegler, M. D. Ziegler, and J. P. Biersack. "SRIM – The stopping and range of ions in matter (2010)". In: *Nuclear Instruments and Methods in Physics Research B* 268 (2010), pp. 1818–1823.

[48] URL: http://www.srim.org/StopPlots/STOPO110.gif. (accessed: 26.04.2023).

[49] J. Görres at al. "The influence of intense ion beams on gas target densities". In: *Nuclear Instruments and Methods* 177 (1980), pp. 295–303.

[50] D. Bemmerer et al. "Low energy measurement of the $^{14}$N(p,$\gamma$)$^{15}$O total cross section at the LUNA underground facility". In: *Nuclear Physics A* 779 (2006), pp. 297–317.

[51] M. Marta et al. "Study of beam heating effect in a gas target through Rutherford scattering". In: *Nuclear Instruments and Methods in Physics Research Section A: Accelerators, Spectrometers, Detectors and Associated Equipment* 569 (2006), pp. 727–731.

[52] G. F. Knoll. *Radiation Detection and Measurement*. Fourth Edition. John Wiley & Sons, Inc, 2010.

[53] A. Ciapponi. *Studio della reazione $^{20}$Ne(p,$\gamma$)$^{21}$Na alle energie astrofisiche presso l'acceleratore LUNA 400 kV*. Laurea Magistrale in Fisica, Università degli studi di Milano. 2021.

[54] A. Caciolli et al. "A new FSA approach for in situ $\gamma$ ray spectroscopy". In: *Science of the The Total Environment* 414 (2012), pp. 639–645.